



ScuDo
Scuola di Dottorato ~ Doctoral School
WHAT YOU ARE, TAKES YOU FAR



Doctoral Dissertation
Doctoral Program in Physics (32.th cycle)

Light manipulation in multilayered photonic structures

Ugo Stella

* * * * *

Supervisor

Prof. Emiliano Descrovi

Doctoral Examination Committee:

Prof. Matthieu Roussey, University of Eastern Finland

Prof. Paolo Biagioni, Politecnico di Milano

Prof. Costanza Toninelli, Università di Firenze

Prof. Stefano Taccheo, Politecnico di Torino

Prof. Fabrizio Giorgis, Politecnico di Torino

Politecnico di Torino

29/05/2020

This thesis is licensed under a Creative Commons License, Attribution - Noncommercial-NoDerivative Works 4.0 International: see www.creativecommons.org. The text may be reproduced for non-commercial purposes, provided that credit is given to the original author.

.....
Ugo Stella
Turin, 29/05/2020

Abstract

This thesis is devoted to novel nano-optical phenomena and devices based on multilayered photonic structures sustaining electromagnetic surface waves. First, a hybrid dielectric-metallic multilayer is considered, able to sustain electromagnetic surface modes called *Tamm plasmons*. The coupling of emitters to Tamm modes is exploited in order to obtain a highly directional fluorescence emission from a single nanoaperture in a metal film. The increased directionality and beaming of the emission coupled to Tamm modes is demonstrated experimentally through back focal plane images of the fluorescence intensity. Experimental observations are well supported by rigorous calculations, performed by means of a Finite-Difference Time-Domain model. Next, electromagnetic surface waves sustained by a total dielectric multilayer are considered, called *Bloch surface waves*. An original device for enhancing the radiative decay rate and directing the emission of organic dyes located on the surface of a patterned dielectric multilayer stack is presented. The device is based on a cavity for Bloch surface waves surrounded by a circular outcoupler to redirect the coupled emission at low numerical aperture. A streak-camera based spectroscopic setup is implemented in order to demonstrate the Purcell effect through spectral and temporal measurements of the coupled emission. Also, Bloch surface waves are further exploited for producing vectorial vortex beam through a mechanism involving a spiral diffraction grating on top of a dielectric multilayer. The vortex beam is generated in a two-step process, involving a spin to orbital angular momentum conversion from a focused circularly polarized beam into radially propagating Bloch surface waves and a Bloch surface wave diffraction in free-space, with the additional phase distribution imparted by the spiral diffraction grating. Experimentally, Back focal plane imaging plus Stoke's polarimetry techniques are implemented in order to retrieve the angular distribution and polarization state of the diffracted light. The mechanism effectively generates a vortex beam carrying orbital angular momentum at low numerical aperture.

Contents

Introduction	1
1 Multilayered structures and electromagnetic surface waves	3
1.1 Physical fundamentals	3
1.1.1 Optics in dielectric media	3
1.1.2 Optics in metals	5
1.1.3 Polarization dependent reflection and refraction	6
1.1.4 Total internal reflection	8
1.2 Transfer matrix method	8
1.2.1 One dimensional photonic crystal	10
1.3 Bloch surface waves	13
1.3.1 Leakage radiation	16
1.4 Tamm plasmon polaritons	17
1.5 Multilayer fabrication and preparation	18
1.5.1 Plasma enhanced chemical vapor deposition	19
1.5.2 Plasma-ion assisted deposition	19
1.5.3 Atomic layer deposition	20
2 Tamm plasmon coupled fluorescence in nanohole structure	23
2.1 Coupling of emitters with photonic structures	23
2.2 Tamm plasmon polariton coupled fluorescence on flat metallic film	25
2.3 Coupling of fluorophores in single nanoapertures	27
2.3.1 Angular distribution of radiation in far field	29
2.3.2 Effect of the diameter of the nanoaperture	35
2.3.3 Effect of the shape of the nanoaperture	35
2.4 Conclusions	38
3 Bloch surface wave cavity for spontaneous emission decay rate enhancement	39
3.1 Purcell factor	39
3.2 State of the art for optical resonators for Purcell effect	41
3.2.1 The concept of Bloch surface wave cavity	42

3.3	Bloch surface wave coupled fluorescence on flat multilayer structure	43
3.4	Bloch surface waves circular cavity	46
3.4.1	Numerical model	47
3.5	Time-resolved spectroscopic setup	49
3.6	Experimental results	50
3.6.1	Spectral signature of BSW-coupled emission	50
3.6.2	Temporal signature of BSW-coupled emission	53
3.7	Directional BSW cavity-coupled emission in free-space	55
3.7.1	Numerical model	55
3.7.2	Angular distribution with back focal plane technique	56
3.7.3	BFP spectral and temporal analysis	56
3.8	Conclusions	59
4	Vortex beam generation by spin-orbit coupling in Bloch surface waves	61
4.1	Angular momenta of light	62
4.1.1	Spin angular momentum and polarization structure of light	62
4.1.2	Stokes parameters	63
4.1.3	Orbital angular momentum	65
4.2	Vortex beam	65
4.3	Spiral diffraction grating	67
4.3.1	The sample	67
4.3.2	Experimental setup	69
4.4	Numerical modeling	70
4.5	Analysis of spiral radiation patterns	72
4.5.1	Circular outcoupler ($m = 0$)	72
4.5.2	Spiral outcoupler ($m = -1$)	74
4.5.3	Spiral outcoupler ($m = -2$)	77
4.6	Conclusion	80
	Summary and perspectives	81
	A Stokes parameters of diffracted light from annular gratings	85
	Bibliography	97

Introduction

In a 1987 paper, Eli Yablonovitch observed that losses in semiconductor lasers and other devices arising from light emitted at unwanted frequencies would not occur in a medium that prevented these frequencies of light from propagating [1]. He proposed a periodic optical nanostructure that affects the motion of photons in much the same way that ionic lattices affect electrons in solids, called *photonic crystal* (PC). Yablonovitch's main goal was to engineer photonic density of states to control the spontaneous emission of materials embedded in the PC. He offered an analogy to semiconductors, which have an energy “band gap” between the valence electrons—associated with chemical bonds—and the conduction electrons. Just as electrons with energies in the band gap cannot exist in a semiconductor, so light with frequencies in the electromagnetic band gap would not exist in the proposed structure. In each case, the periodic structure leads to destructive wave interference (electron waves or electromagnetic fields) that leads to the gap. After 1987, the number of research papers concerning PCs began to grow exponentially. However, due to the difficulty of fabricating these structures at optical scales, early studies were either theoretical or in the microwave regime, where PCs can be built on the more accessible centimetre scale [2]. The increased capability, in the last decades, to fabricate structures at the nanoscale and the high degree of control of material properties achieved by modern deposition systems has led to a plethora of photonic applications based on the control of the dispersion relation of visible light in two dimensional PCs, such as laser technology [3], lighting systems [4] and many others [5, 6].

Also, when an artificial defect is introduced into the photonic crystal, a photonic nanocavity is produced that can interact with light emitters. The efficient control of the Local Density of States (LDOS) in photonic crystal nanocavities has led to the implementation of PCs for biosensing [7] and for the control of spontaneous emission (SE) [8]. However, the interaction of the emitters with the modes of the structure is effective only if the emitters are located in close proximity of the LDOS local maxima [9]. In 2D PC slabs, this might be difficult to attain, as photonic modes are preferentially confined within high-index regions of the structure [10], with only evanescent tails leaking in the surrounding medium.

As an alternative to 2D PCs, a second route for enhancing light/matter interaction is to exploit surface plasmons (SPPs) on smooth planar or structured metallic films. SPPs are electromagnetic modes sustained at an appropriate metallic/dielectric interface wherein the field reaches its maximum intensity at the surface of the metal [11, 12]. The compression of the electromagnetic field in small volumes allows to greatly enhance the light-matter interaction. Unfortunately, SPPs relies on the oscillations of free electrons in metal, and such phenomenon is intrinsically affected by the scattering of electrons with metallic ions. The scattering results in ohmic losses that affect the performances of such devices.

The subject of this thesis is the attempt to overcome some of the limitations of the two approaches presented by employing properly designed multilayered photonic structures, sustaining electromagnetic surface waves, in order to manipulate the light at the nanoscale. The first chapter deals with a brief description of the basic principles underlying the physics of electromagnetic surface waves. In particular, two different types of surface waves are discussed: the Tamm plasmon polaritons (TPPs) and the Bloch surface waves (BSWs). In the second chapter, it is shown that coupling of fluorophores with Tamm plasmon exploiting small nanoapertures fosters the reshaping of the fluorescence which is emitted normally to the sample surface, with a small angular width. The third chapter will deal with the enhancement of the spontaneous emission decay rate, also called Purcell effect, assisted by resonant BSW in circular cavities, exploiting the so called Bloch Surface Wave Coupled Emission (BSW-CE), that is the natural coupling of light emitters with BSW. In Chapter 4, a mechanism for vortex beam generation is discussed, based on the diffraction of BSW from a spiral grating providing orbital angular momentum to the diffracted beam. Finally, a conclusion is given in Chapter 5 to briefly summarize the results, and to suggest possible directions for further research.

Chapter 1

Multilayered structures and electromagnetic surface waves

This Chapter provides an introduction into the physical basics of the investigated photonic multilayered structures in order to support understanding of the experiments and main conclusions presented in this thesis. At first, the principles of light propagation and excitations in dielectric media and metals are discussed. The propagation of electromagnetic waves in layered media is explained theoretically and a short introduction to the transfer matrix algorithm – a powerful method for calculating eigenstates in optical systems such as 1DPC – is given. Next, electromagnetic surface waves sustained by multilayers are discussed, providing the basic concepts regarding this important phenomenon. The last Sections briefly deal with the fabrication techniques implemented for the multilayers production.

1.1 Physical fundamentals

1.1.1 Optics in dielectric media

The propagation of an electromagnetic wave in a given medium is generally described by a set of linear partial differential equations, the Maxwell equations:

$$\begin{aligned}\nabla \times \mathbf{H}(\mathbf{r}, t) &= \mathbf{j}(\mathbf{r}, t) + \frac{\partial \mathbf{D}(\mathbf{r}, t)}{\partial t} \\ \nabla \times \mathbf{E}(\mathbf{r}, t) &= -\frac{\partial \mathbf{B}(\mathbf{r}, t)}{\partial t} \\ \nabla \cdot \mathbf{B}(\mathbf{r}, t) &= 0 \\ \nabla \cdot \mathbf{D}(\mathbf{r}, t) &= \rho(\mathbf{r}, t)\end{aligned}\tag{1.1}$$

These formulae couple the electric field \mathbf{E} , the electric displacement field \mathbf{D} , the

magnetic flux density \mathbf{B} and the magnetic field \mathbf{H} . The interplay of these fields with free electric charges and currents is represented by the charge density ρ_f and the current density \mathbf{j} .

A dielectric medium is free of charge carriers ($\rho_f = 0$) and thus the electric current flux becomes zero ($\mathbf{j} = 0$). In this case the Eqs. 1.1 are homogeneous. If the dielectric medium is linear and isotropic, the following constitutive relations hold:

$$\begin{aligned}\mathbf{D} &= \epsilon_0 \epsilon(\omega) \mathbf{E} \\ \mathbf{B} &= \mu_0 \mu(\omega) \mathbf{H}\end{aligned}\tag{1.2}$$

where ϵ_0 and μ_0 are the electric permittivity and the magnetic permeability of vacuum and $\epsilon(\omega)$ and $\mu(\omega)$ are the frequency-dependent relative permittivity and permeability of the material.

After substituting the field \mathbf{D} and \mathbf{B} in Maxwell's *curl* equations by the expressions 1.2 is possible to derive the homogeneous wave equation [13]:

$$\Delta \mathbf{E} - \frac{1}{c^2} \frac{\partial^2 \mathbf{E}}{\partial t^2} = 0\tag{1.3}$$

The magnetic and electric constants of the medium relate the phase velocity c with the vacuum speed of light c_0 :

$$c^2 = \frac{c_0^2}{\epsilon \mu} := \frac{c_0^2}{n^2}\tag{1.4}$$

In this thesis, all the materials are non-magnetic at optical frequencies leading to $\mu = 1$. Moreover, in ideal dielectric materials, absorption is zero and the refractive index n is a real number which has fundamental importance in optics.

In a linear and isotropic medium, a possible solution of the wave Eq. 1.3 is the transversal plane wave with angular frequency ω :

$$\mathbf{E}(\mathbf{r}) = \mathbf{E}_0 e^{i(\mathbf{k} \cdot \mathbf{r} - \omega t)}\tag{1.5}$$

where \mathbf{k} denotes the wave vector of the propagating plane wave, pointing towards the direction of propagation. The dispersion relation of the plane wave is linear, in accordance to Eq. 1.3:

$$\omega = c|\mathbf{k}|\tag{1.6}$$

In this framework, the materials used are linear and the optical fields are considered as monochromatic with a single angular frequency and each frequency component interacts independently with the media.

1.1.2 Optics in metals

In metals, strong optical losses alter the propagation of electromagnetic waves. The high density of free electrons generates current flows in metals, causing the high reflectivity for frequencies up to the visible range. This means that \mathbf{j} and ρ in Maxwell's equations 1.1 have finite values. With this in mind, it is possible to derive the wave equation for the propagation of electromagnetic waves in highly absorbing metals [14]:

$$\nabla(\nabla \cdot \mathbf{E}) - \Delta \mathbf{E} = -\mu_0 \mu \frac{\partial \mathbf{j}}{\partial t} - \frac{1}{c^2} \frac{\partial^2 \mathbf{E}}{\partial t^2} \quad (1.7)$$

According to Ohm's law, the electric field \mathbf{E} and the current density \mathbf{j} are linearly related via the conductivity σ :

$$\mathbf{j} = \sigma(\omega) \mathbf{E} \quad (1.8)$$

Taking a harmonic time dependence as in eq. 1.5, the derivatives with respect to space and time transform into the Fourier domain as $\partial/\partial t \rightarrow -i\omega$, $\partial^2/\partial t^2 \rightarrow -\omega^2$, $\nabla \rightarrow -i\mathbf{k}$ and $\Delta \rightarrow -k^2$. [15] Finally, the propagation of electromagnetic waves in non-magnetic metals can be described with the equation:

$$-\hat{\mathbf{k}}(-\hat{\mathbf{k}} \cdot \mathbf{E}) + \hat{k}^2 \mathbf{E} = \left(i\mu_0 \sigma \omega + \frac{\omega^2}{c^2} \right) \mathbf{E} \quad (1.9)$$

where $\hat{\mathbf{k}}$ denotes the *complex* wave vector. The generic dispersion relation of a damped electromagnetic wave in metals is given by:

$$\hat{k}^2 = \frac{\omega^2}{c_0^2} \left(\epsilon + i \frac{\sigma}{\omega \epsilon_0} \right) = \frac{\omega^2}{c_0^2} \hat{\epsilon} = \frac{\omega^2}{c_0^2} \hat{n}^2 \quad (1.10)$$

when transverse waves are considered (i.e. $\hat{\mathbf{k}} \cdot \mathbf{E} = 0$).

Eq. 1.10 is identical to 1.6, but with a generalized complex-valued dielectric function $\hat{\epsilon} = \epsilon' + i\epsilon''$ and the complex refractive index $\hat{n} = n + i\kappa$. The real and imaginary parts of the refractive index are related to the complex dielectric function as:

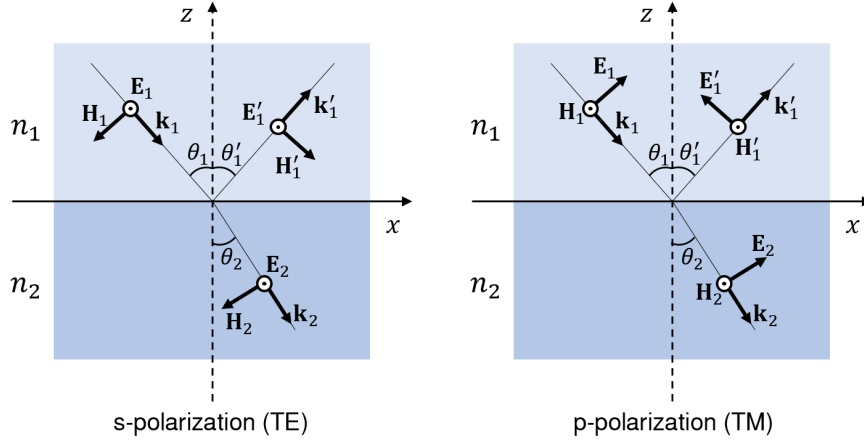


Figure 1.1: Reflection and refraction of s (TE) and p (TM) waves at the interface between two media with refractive indices n_1 and n_2 .

$$\begin{aligned}
 n^2 &= \frac{\epsilon'}{2} + \frac{1}{2}\sqrt{\epsilon'^2 + \epsilon''^2} \\
 \kappa &= \frac{\epsilon''}{2n} \\
 \epsilon' &= n^2 - \kappa^2 \\
 \epsilon'' &= 2n\kappa
 \end{aligned} \tag{1.11}$$

where κ is called the *attenuation coefficient*. According to the Lambert-Beer's law, κ is directly related to the attenuation of the intensity $I(z)$ of a light beam propagating through a medium with absorption coefficient α along the z -direction:

$$I(z) = I_0 e^{-\alpha z} \quad \text{with} \quad \alpha(\omega) = \frac{2\kappa(\omega)\omega}{c} \tag{1.12}$$

According to Eq. 1.12, even a small κ will lead to a strong attenuation for visible light, limiting the penetration depth into conducting media to a small fraction of the wavelength λ .

1.1.3 Polarization dependent reflection and refraction

In the previous Sections, the propagation of light in infinite and homogeneous media is described based on solutions of the wave equation. In this Section the general behaviour of light at optical boundaries is discussed. Detailed discussions can be found in [13, 16, 17]. In figure 1.1, two media on both sides of the interface

$z = 0$ have the refractive indices n_1 and n_2 , respectively. The coordinate system is chosen such that the xz plane is the plane of incidence. A plane wave with wave vector \mathbf{k}_1 is incident from the upper side. Without loss of generality, it is convenient to describe the incident electromagnetic wave as the superposition of two fields exhibiting perpendicular polarizations. If the two media are homogeneous and isotropic, these two components (p and s waves) are independent of each other. The s wave is also known as a TE wave because the electric field vector \mathbf{E} is transverse to the plane of incidence, whereas in case of p or TM wave the magnetic field vector \mathbf{H} is transverse to the plane of incidence. According to Maxwell's equations, the boundary conditions require the tangential components of the electric and magnetic field vectors E_x , E_y , H_x and H_y to be continuous at the interface $z = 0$, taking the coordinate system of figure 1.1 (see [13, 14]). For s polarization, imposing the continuity of E_y and H_x at the interface in $z = 0$ leads to:

$$\begin{aligned} E_1 + E'_1 &= E_2 \\ \sqrt{\frac{\epsilon_1}{\mu_1}}(E_1 - E'_1) \cos \theta_1 &= \sqrt{\frac{\epsilon_2}{\mu_2}} E_2 \cos \theta_2 \end{aligned} \tag{1.13}$$

where the continuity on the x -component of the magnetic field $H_{1,x} + H'_{1,x} = H_{2,x}$ and $\mathbf{H} = \sqrt{\epsilon/\mu} \mathbf{k} \times \mathbf{E}$ have been used to derive the second equation, valid for transverse waves ($\mathbf{E} \perp \mathbf{H}$, $\mathbf{E} \perp \mathbf{k}$, $\mathbf{H} \perp \mathbf{k}$).

Analogously, the continuity of E_x and H_y for p polarization leads to:

$$\begin{aligned} (E_1 - E'_1) \cos \theta_1 &= E_2 \cos \theta_2 \\ \sqrt{\frac{\epsilon_1}{\mu_1}}(E_1 + E'_1) &= \sqrt{\frac{\epsilon_2}{\mu_2}} E_2 \end{aligned} \tag{1.14}$$

From the boundary conditions 1.13 and 1.14, it is possible to calculate the Fresnel reflection and transmission coefficients for s and p polarization, defined as $r_s = E'_{1,s}/E_{1,s}$, $t_s = E_{2,s}/E_{1,s}$, $r_p = E'_{1,p}/E_{1,p}$ and $t_p = E_{2,p}/E_{1,p}$ (considering $\mu_1 = \mu_2 = 1$):

$$\begin{aligned} r_s &= \frac{n_1 \cos \theta_1 - n_2 \cos \theta_2}{n_1 \cos \theta_1 + n_2 \cos \theta_2}, & t_s &= \frac{2n_1 \cos \theta_1}{n_1 \cos \theta_1 + n_2 \cos \theta_2} \\ r_p &= \frac{n_2 \cos \theta_1 - n_1 \cos \theta_2}{n_1 \cos \theta_2 + n_2 \cos \theta_1}, & t_p &= \frac{2n_1 \cos \theta_1}{n_1 \cos \theta_2 + n_2 \cos \theta_1} \end{aligned} \tag{1.15}$$

These formulas describe the behavior of an electromagnetic wave at a boundary and apply to any two media, for both real and complex-valued refractive indices.

1.1.4 Total internal reflection

An important phenomenon underlying the formation of evanescent waves is the *total internal reflection* (TIR). If the first medium has a refractive index larger than that of the second medium ($n_1 > n_2$) and if the incidence angle θ_1 is sufficiently large, Snell's law,

$$\sin \theta_2 = \frac{n_1}{n_2} \sin \theta_1 \quad (1.16)$$

gives complex values of the angle θ_2 . This happens when the incidence angle θ_1 is greater than

$$\theta_c = \sin^{-1} \frac{n_2}{n_1}, \quad n_2 < n_1 \quad (1.17)$$

where θ_c is called *critical angle* of incidence. Under this condition of incidence, there is no energy flow across the interface. Instead, all the light energy is totally reflected from the surface and the Fresnel coefficients are complex numbers of unit module, i.e. $|r_s| = |r_p| = 1$. Interestingly, at total reflection, the transmission coefficient $|t_s|$ and $|t_p|$ are not vanishing, meaning that even though the light energy is totally reflected, the electromagnetic fields still penetrate into the second medium. In these circumstances, the electric field intensity decreases exponentially moving away from the interface. Such a wave is called *evanescent wave*. The attenuation occurs within a distance which is only several wavelengths.

1.2 Transfer matrix method

In the previous Section, the principles of transmission and reflection at a single interface are discussed. In a sample consisting of several layers, the transfer matrix method is used to describe multiple reflections and transmissions [13, 17, 18]. Instead of accounting for multiple reflections by solving Fresnel's formulæ for each single interface, one single characteristic matrix is obtained and has to be evaluated. The electric field $E(z, t)$, propagating along the z axis, consists of a right-traveling ($+k$) and a left-traveling ($-k$) wave of angular frequency ω and can be written as

$$E(z, t) = Ae^{i(kz - \omega t)} + Be^{-i(kz + \omega t)} \quad (1.18)$$

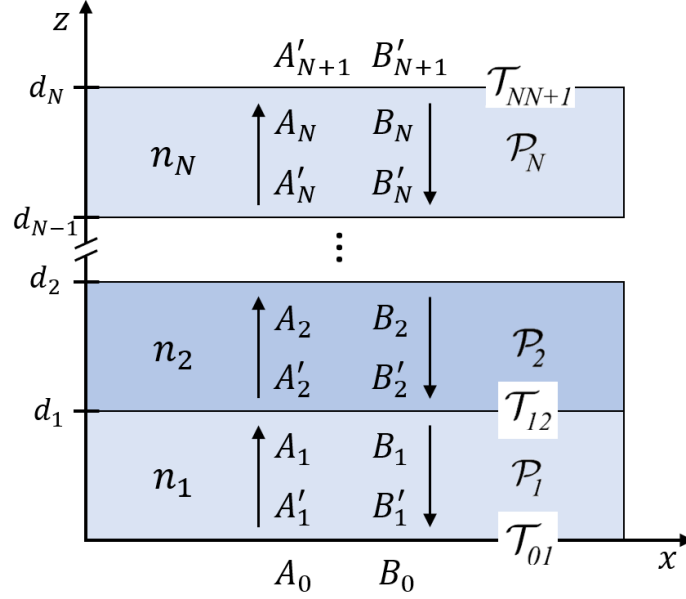


Figure 1.2: A multilayered dielectric medium with the plane-wave amplitudes associated with n^{th} layer.

If the two amplitudes A and B of $E(z, t)$ are represented as column vectors, one can account for propagation through the bulk of the layer (index j) with (complex) refractive index n_j and thickness d_j by using the diagonal propagation matrix \mathcal{P}_j

$$\begin{pmatrix} A'_j \\ B'_j \end{pmatrix} = \mathcal{P}_j \cdot \begin{pmatrix} A_j \\ B_j \end{pmatrix} = \begin{pmatrix} e^{i\phi_j} & 0 \\ 0 & e^{i\phi} \end{pmatrix} \cdot \begin{pmatrix} A'_j \\ B'_j \end{pmatrix} \quad (1.19)$$

where ϕ_j is the respective phase shift, given by:

$$\phi_j = k_j d_j = \frac{2\pi}{\lambda_0} n_j d_j \cos \theta_j \quad (1.20)$$

with λ_0 the wavelength in free space.

To link the amplitudes of the waves on the two sides of the interfaces the *transmission matrices* \mathcal{T}_{jk} are introduced as:

$$\begin{pmatrix} A_j \\ B_j \end{pmatrix} = \mathcal{T}_{jk} \cdot \begin{pmatrix} A'_k \\ B'_k \end{pmatrix} = \frac{1}{t_{jk}} \begin{pmatrix} 1 & r_{jk} \\ r_{jk} & 1 \end{pmatrix} \cdot \begin{pmatrix} A'_k \\ B'_k \end{pmatrix} \quad (1.21)$$

where t_{jk} and r_{jk} are the Fresnel transmission and reflection coefficients, introduced in the previous Section.

Each interface is represented with a transmission matrices, and the bulk of each layer is represented by a propagation matrix. Such recipe can be extended to the case of multilayer stacks, and this is the main advantage of the transfer matrix method, reducing the evaluation of Fresnel equations for multiple reflections to simple matrix multiplications. For example, a stack consisting of N layers can be represented as:

$$\begin{pmatrix} A_0 \\ B_0 \end{pmatrix} = \mathcal{T}_{01} \cdot \left(\prod_{l=1}^N \mathcal{P}_l \cdot \mathcal{T}_{l,l+1} \right) \cdot \begin{pmatrix} A'_{N+1} \\ B'_{N+1} \end{pmatrix} = \mathcal{M} \cdot \begin{pmatrix} A'_{N+1} \\ B'_{N+1} \end{pmatrix} \quad (1.22)$$

where A_0 , B_0 and A'_{N+1} , B'_{N+1} denote the field amplitudes to the left and right of the layer stack and correspond to ambient or the substrate, respectively. The matrix \mathcal{M} is the characteristic matrix of the entire structure, including the substrate and the ambient medium. It can be represented in the following 2×2 form:

$$\mathcal{M} = \begin{pmatrix} M_{11} & M_{12} \\ M_{21} & M_{22} \end{pmatrix} \quad (1.23)$$

In general, for multilayer structures, the expressions for M_{jk} become complicated, but the reflectance R and the transmittance T can be calculated as:

$$R = |r|^2 = \left| \frac{M_{21}}{M_{11}} \right|^2 \quad \text{and} \quad T = |t|^2 = \left| \frac{1}{M_{11}} \right|^2 \frac{\tan \theta_0}{\tan \theta_{N+1}} \quad (1.24)$$

In this framework, all transfer matrix calculations are performed with the commercial software "FDTD 3D electromagnetic simulator"¹.

1.2.1 One dimensional photonic crystal

To illustrate the use of transfer matrix method in the calculation of reflection and transmission of a multilayer structure, the case of a periodic sequence of dielectric layers with alternating refractive indices (n_j) is considered. In this case, multiple reflections occur which can interfere constructively if the thickness of each layer is $d_j = \lambda_d/4n_j$, where $j = H, L$ represents high and low refractive medium, respectively. In this case, the phase shift of the reflected parts equals $2 \cdot \pi/2$. In addition, the amplitude reflection coefficients for the interfaces have alternating signs. Therefore, all reflected components from the interfaces interfere constructively, having an overall phase shift of 2π , which results in a strong reflection at

¹Lumerical, Inc.

a certain design wavelength λ_d . This device is called distributed Bragg reflectors (DBR), because of the analogy with the Bragg reflections of x-rays at crystal planes. Despite the reflected light at a single dielectric interface is only few percent, a DBR with $2N + 1$ layers can strongly increase the reflectivity.

According to Eq. 1.22, the characteristic matrix for a DBR with a final top layer of high refractive index is given by:

$$\begin{pmatrix} M_{11} & M_{12} \\ M_{21} & M_{22} \end{pmatrix} = \mathcal{T}_{0H}(\mathcal{P}_H \mathcal{T}_{HL} \mathcal{P}_L \mathcal{T}_{LH})^N \mathcal{P}_H \mathcal{T}_{HS}, \quad (1.25)$$

where the indices 0 and S stands for ambient and substrate, respectively.

The propagation matrix for quarter-wave layers (with $\phi_j = \pi/2$), independent of the material, is given by:

$$\mathcal{P} = \begin{pmatrix} i & 0 \\ 0 & -i \end{pmatrix} \quad (1.26)$$

After calculating the dynamical matrices \mathcal{T} , the matrix multiplication in Eq. 1.25 is carried out. The maximum reflectance of a DBR consisting of $2N + 1$ layers can be calculated using Eq. 1.24:

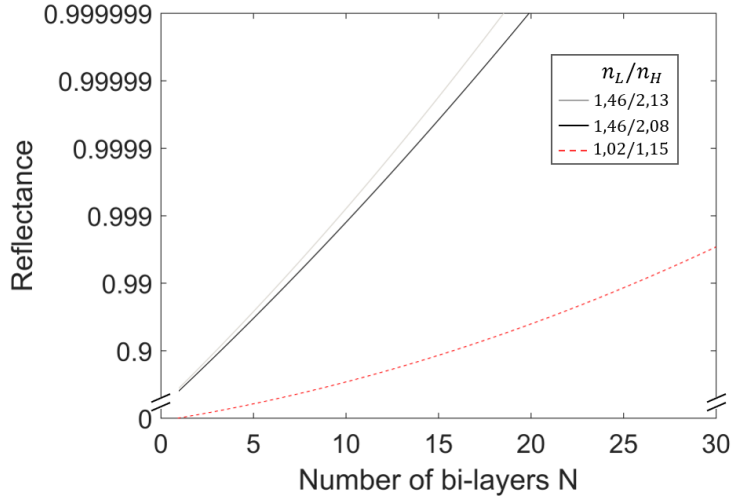


Figure 1.3: Calculated maximum reflectance versus number of bi-layers in the DBR, with material combination: $n_H = 2.13$ (Si_3N_4) or $n_H = 2.08$ (Ta_2O_5) and $n_L = 1.46$ (SiO_2). Red dashed line represents the case of effective indices $n_H = 1.15$ and $n_L = 1.02$

$$R = \left(\frac{1 - (n_s/n_0)(n_L/n_H)^{2N}}{1 + (n_s/n_0)(n_L/n_H)^{2N}} \right)^2 \quad (1.27)$$

For large N , the reflectance R approaches unity exponentially as a function of N . Figure 1.3 illustrates the reflectance of a DBR as a function on the number of layers N , for three different sets of refractive indices. The black and grey lines correspond to experimentally obtained refractive indices used in this thesis for DBR composed of $\text{Ta}_2\text{O}_5/\text{SiO}_2$ ($n_H/n_L = 2.08/1.46$) and $\text{Si}_3\text{N}_4/\text{SiO}_2$ ($n_H/n_L = 2.13/1.46$). The red dashed reflectance profile corresponds instead to the effective index contrast of the circular DBR, described later in Chapter 3. It is worth noting that, in this case, more layers are required to reach high reflectance values due to the small effective index contrast ($n_H/n_L = 1.15/1.02$). All the calculated curves do not account for losses in the materials nor the respective dispersion, meaning that, for realistic media, it is not possible to reach $R = 1$ by increasing the number of layers.

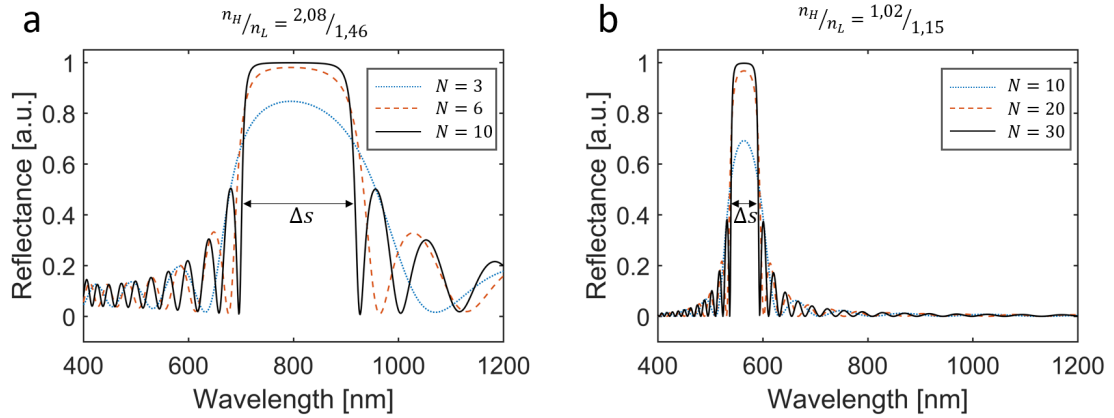


Figure 1.4: Calculated reflectance profiles at normal incidence of lossless DBR mirrors. Increasing the number of layer pairs N , the stop band becomes more pronounced, while the extension Δs is set by the difference in refractive index. **a)** $n_H/n_L = 2.08/1.46$ (materials $\text{Ta}_2\text{O}_5/\text{SiO}_2$). **b)** $n_H/n_L = 1.15/1.02$ (effective indices in circular DBR, see Chapter 3).

In Figure 1.4, the reflectance spectra of DBRs with varying number of layers are calculated using the transfer matrix method. The number of layer pairs ranges from $N = 3, 6, 10$ in the case of DBR composed of $\text{Ta}_2\text{O}_5/\text{SiO}_2$ ($n_H/n_L = 2.08/1.46$), while $N = 10, 20, 30$ for the case of $n_H/n_L = 1.15/1.02$. In both cases, the reflectance within a certain spectral range increases with increasing number of layers. This range is called *stop band* and is analogous to the band gap occurring in semiconductor crystals. When the ionic potential, that in semiconductor gives rise to

the electronic band structure, is replaced by the dielectric function and the electronic wavefunction is replaced with an electromagnetic wave, a periodic dielectric structure produces a photonic band structure. At the origin of the band gap is the periodicity of either the electronic crystal or the DBR as a crystal for photons. This is why such structure is called *one dimensional photonic crystal* (1DPC) [19]. The extension of the stop band (also called *forbidden band*) can be approximated as [20]:

$$\Delta s = \frac{2\lambda_d \Delta n}{\pi n} \quad (1.28)$$

where Δn denotes the difference in refractive indices of the composing materials and $n = (n_H + n_L)/2$. In Figure 1.4, the extensions of the stop bands are remarkably different in the two cases, due to the different refractive indices contrast.

1.3 Bloch surface waves

So far, reflection and transmission properties of layered media have been discussed. In addition to these properties, layered media can also support confined electromagnetic propagation, the so-called guided waves (or guided modes). In this Section, the guiding properties of 1DPC sandwiched between two semi-infinite bounding media are discussed. To study the propagation of confined modes, the electric field distribution in bounded 1DPC can be written as $E(z, t) = E(z)e^{i\omega t}$, with:

$$E(z) = \begin{cases} B_0 e^{q_0 z}, & z < 0 \\ A_j e^{-ik_{jz}(z-z_j)} + B_j e^{ik_{jz}(z-z_j)}, & z_{j-1} \leq z < z_j \\ A'_s e^{-q_s(z-z_N)} & z_N \leq z \end{cases} \quad (1.29)$$

with:

$$\begin{aligned} k_{jz} &= \left[\left(\frac{n_j \omega^2}{c} \right) - k_{\parallel}^2 \right]^{1/2}, \\ q_0 &= ik_{0z} = \left[k_{\parallel}^2 - \left(\frac{n_0 \omega^2}{c} \right) \right]^{1/2}, \\ q_s &= ik_{sz} = \left[k_{\parallel}^2 - \left(\frac{n_s \omega^2}{c} \right) \right]^{1/2}, \end{aligned} \quad (1.30)$$

where k_{\parallel} is the propagation constant along the x axis and k_{jz} is the z component of the wave vector in the layer whose index of refraction is n_j . For confined

mode, the two parameters q_0 and q_s must remain positive, meaning that the electromagnetic field intensity exponentially decreases moving away from the 1DPC in the bounding media.

Following the formulation discussed in Section 1.2, the characteristic matrix \mathcal{M} can be obtained as reported in Eq. 1.22, relating the field amplitudes on both sides of the 1DPC:

$$\begin{pmatrix} 0 \\ B_0 \end{pmatrix} = \begin{pmatrix} M_{11} & M_{12} \\ M_{21} & M_{22} \end{pmatrix} \begin{pmatrix} A'_s \\ 0 \end{pmatrix} \quad (1.31)$$

where the amplitudes A_0 and B'_s have been set to 0 for confined modes whose field amplitudes must vanish at infinity.

Once the Eq. 1.31 is obtained, the mode condition is given by:

$$M_{11} = 0, \quad (1.32)$$

where M_{11} is a function of ω , k_{\parallel} , indices n_j and thicknesses d_j . Eq. 1.32 can be used for a specific structure (n_j , d_j) and a specific frequency ω (or wavelength λ) to solve for the propagation constant k_{\parallel} of all the confined modes. The effective refractive index of each mode can be simply calculated as $n_{eff} = k_{\parallel}(2\pi/\lambda_0)^{-1}$. Once the propagation constants k_{\parallel} of the confined modes are obtained, the wavefunction of the modes can also be obtained by using the matrix method. Figure 1.5 shows the wavefunctions with the corresponding effective refractive index of the modes calculated at $\lambda_0 = 570$ nm for a 1DPC with $N = 6$ pairs of Ta₂O₅/SiO₂, corresponding to the structure described later in Chapter 4. The wavefunction of TE _{j 0} has exactly j zero crossings. What is remarkable is the wavefunction shown in Figure 1.5h, which is very different from the rest. Its energy is mostly confined near the interface 1DPC/Air. This mode is called *Bloch surface wave* (BSW), and has crucial importance in this thesis.

The BSW dispersion relation can be easily visualized through the reflectance map, calculated using the transfer matrix method. In this case, formula 1.24 can be used to calculate the reflectance from the multilayer sustaining BSW for a range of wavelengths and propagation constants k_{\parallel} . When the propagation constant matches the BSW wavevector k_{BSW} , the BSW is excited and a narrow dispersed dip appears in the reflectance profile, since the energy of the BSW is confined at the interface. Figure 1.6 shows the reflectance map corresponding to the multilayer structure of Figure 1.5a, showing the well-defined dispersion relation of the TE-polarized BSW. The angles of incidence θ with respect to the 1DPC normal is used for the x -axis, θ being directly related to the propagation constants as $k_{\parallel} = (2\pi/\lambda_0)n_s \sin \theta$. The BSW dispersion relation appears above the glass/air critical angle θ_c and lies within the stop-band of the 1DPC. The BSW wavevector can be calculated as:

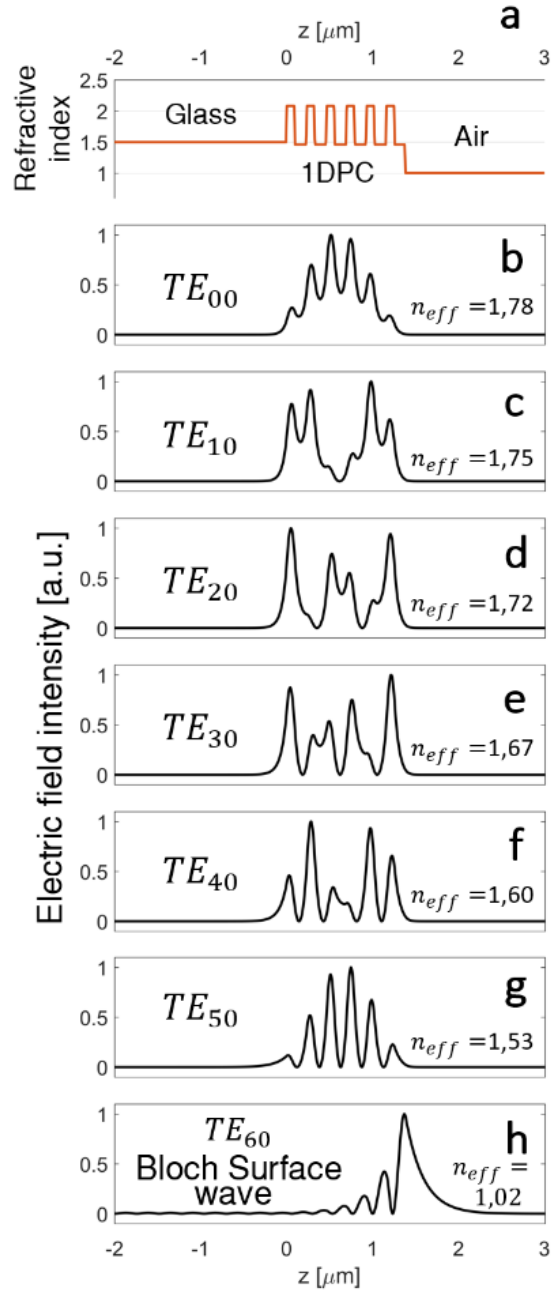


Figure 1.5: Wavefunctions at $\lambda_0 = 570$ nm of multilayer structure depicted in **a**, composed of a glass substrate ($n_s = 1.5$), a 1DPC with materials $\text{Ta}_2\text{O}_5/\text{SiO}_2$ ($n_H/n_L = 2.08/1.46$, $d_H/d_L = 95$ nm/ 137 nm, last layer SiO_2 , 127 nm) and air. The n_{eff} for each mode is reported. **b-g** Internal TE_{j0} modes of the multilayer, each presenting j zero crossings. **h** Bloch surface wave confined at the interface 1DPC/air.

$$k_{BSW} = k_0 n_s \sin \theta_{BSW} \quad (1.33)$$

where k_0 is the free space wavevector and θ_{BSW} is the coupling angle. The propagation of such mode in the direction normal to the 1DPC surface is prohibited both in the external dielectric medium (because of TIR) and in the multilayer, since it lies within the stop-band. The width of the resonance is ultimately associated to the overall losses and, consequently, to the decay length of the mode. The top layer of the 1DPC is truncated, interrupting the periodicity of the underlying layers, in order to tune the dispersion of the BSW or to maximize the field intensity at the interface [21].

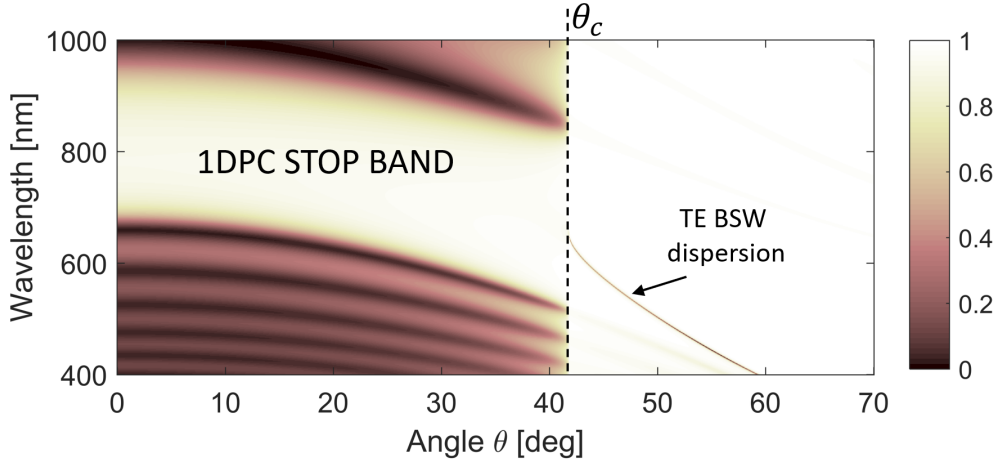


Figure 1.6: Reflectance map referred to the multilayer structure reported in Figure 1.5a. Below the glass/air critical angle, θ_c , the 1DPC stop band is highlighted by the high reflectance region. Above θ_c the reflectance is high for every (λ, θ) point in the map because of TIR, except for the narrow dispersion relation of the BSW.

1.3.1 Leakage radiation

Due to the evanescent nature of BSWs, it is not possible to directly couple freely propagating light in air to BSW both in excitation and in collection. Since the BSW momentum is larger than the free-space momentum of the ambient medium above the 1DPC, a strategy to increase the momentum of the incident light is required. A simple strategy, widely used also in plasmonics, is to couple the 1DPC with a prism, as in the Rather Kretschmann or in the Otto configuration. In the ideal case of a semi-infinite 1DPC, the reflectivity inside the stop band is 1. In real systems with a finite number of layers, an evanescent tail is always crossing the 1DPC, giving rise to a non-perfect reflectance. Such evanescent tail allows to couple the far-field

radiation to BSW whenever the substrate has a refractive index higher than the effective index of BSW [22]. The inverse process is also possible, i.e. the coupling of BSW to far-field. While the BSW propagates at the 1DPC/air interface with wavevector k_{BSW} , some radiation can reach the substrate, showing a propagative behaviour without attenuation at the coupling angle θ_{BSW} . This radiation is called *leakage radiation*. In an ideal lossless and transversally infinitely extended 1DPC with a finite number of layers, all the energy coupled to the BSW will be given back through the leakage radiation in the glass substrate. For this reason, a small fictitious absorption must be included in the materials properties when performing transfer matrix calculation to extract the dispersion relation of the BSW from the reflectance map. This is done by adding a small imaginary part ($\sim 10^{-3}$) to the refractive index of the top layers of the 1DPC, to ensure a correct absorption of the leakage radiation and the appearance of the BSW dip in the reflectance map. This is necessary because of the plane wave nature of the excitation used in the TMM.

BSWs have recently gained a great interest [23] because of the opportunities they offer in flat photonics at visible and near- and mid-infrared frequencies [24–36], BSWs can be considered as the photonic counterpart of Surface Plasmon Polaritons (SPPs), although the physics is completely different: in the case of a metallic surface, the localization of the field at the metal/dielectric interface is due to a negative dielectric constant in the metal [37], while BSWs localization occurs because of interference effects in the 1DPC [38]. Due to the phenomenological analogy among SPPs and BSWs, many of the concepts and methods that apply to SPPs can be imported when dealing with BSWs. Compared to SPPs, BSWs exhibit some inherent advantages, mainly related to the lack of ohmic losses. This leads to higher quality factor resonances with consequently longer typical propagation distances [36]. Moreover, BSW feature narrower mode resonances and spectral and polarization tenability, existing both in TE or TM polarization for properly designed multilayers. The high energy confinement of BSW on top of 1DPC [21] can be particularly advantageous to exploit coupling effects involving nanosources or absorbers deposited on the surface [35, 39–45]. This concept is treated in Chapter 3, which will illustrate how the high energy confinement of BSW is exploited to enhance the spontaneous emission decay rate of emitters embedded in BSW cavity.

1.4 Tamm plasmon polaritons

In the previous Section the properties of Bloch surface waves established at the truncation interface of 1DPC have been discussed. BSWs have a wave vector exceeding that of light in vacuum, and therefore cannot be directly excited by light that is simply incident on the surface of the 1DPC. However, there exist electromagnetic surface waves that can have a zero in-plane wave vector and therefore can be produced by direct optical excitation. Such waves are called Tamm plasmons

polaritons (TPPs), in analogy with electron states predicted by Tamm that can occur in the energy band gap at a crystal surface. TPPs emerged recently from the complex interplay between a metal layer and a periodic dielectric structure - such as DBR - and have been studied by Kaliteevski *et al.* [46]. According to their considerations, the metal/DBR structure results in the formation of localized surface states at the interface. The confinement of the electromagnetic field is due to the negative dielectric constant of metals below the plasma frequency ω_p and the photonic band gap (stop band) of the DBR [47]. Similarly to BSWs, TPPs show interesting features:

- they are localized inside the DBR stop bands;
- the dispersion $\omega(\vec{k}_{\parallel})$ is parabolic in shape;
- in contrast to surface plasmon polaritons, Tamm plasmon polaritons can be excited in both polarizations, in TE and TM;
- the splitting between the TE and TM polarized branches is proposed to scale quadratically with the in-plane k vector;
- their in-plane wave vector is close to zero and they can therefore be excited via direct optical excitation, conversely to BSWs;
- the dispersion relation can be modified by changing the thickness of both the metal layer itself and the adjacent dielectric layers.

Sasin *et al.* reported the experimental observation of TPPs formed at the interface between a gold film and a GaAs/AlAs DBR [48]. In a further step, efficient out-coupling and beaming of TPPs was demonstrated by Lopez-Garcia *et al.* [49], introducing a grating on the air-metal interface providing enhanced directionality of the transmitted beam. Recently, the coupling of TPP to a monolayer of WSe₂ with the formation of exciton-polariton has been studied [50] and the enhancement of spontaneous emission in Tamm plasmon structures has been demonstrated [51]. In Chapter 2, an original concept for beaming and sorting the fluorescence emission coupled to TPPs is discussed.

1.5 Multilayer fabrication and preparation

In the following, the principal fabrication techniques implemented for the production of the multilayers of this thesis work are briefly discussed.

1.5.1 Plasma enhanced chemical vapor deposition

Plasma enhanced chemical vapor deposition (PECVD) is a chemical vapor deposition process used to deposit thin films from a gas state (vapor) to a solid state on a substrate. Chemical reactions are involved in the process, which occur after creation of a plasma of the reacting gases. This technique allows the element incorporation to be controlled by changing the percentage of the feedstock gases in the reactor [52] with a thickness control at the nanometric scale [53]. The PECVD is a modification of the CVD process, in which a plasma is used as a source of energy in order to obtain the dissociation of the reactive gases at temperatures at which they would not dissociate thermally. A plasma is any gas in which a significant percentage of the atoms or molecules are ionized. There are three constituents: neutral atoms or molecules (depending of the type of gas), ions and electrons. The ratio between the number of ionized particles and the neutral ones is called degree of ionization. The degree of ionization of the plasmas used for PECVD can vary in the range $10^{-6} \div 10^{-4}$.

1.5.2 Plasma-ion assisted deposition

This technique belongs to the Physical Vapour Deposition (PVD) methods that are conducted in high vacuum conditions. Material from a thermal vaporization source reaches the substrate with no collision with gas molecules in the space between the source and substrate. The trajectory of the vaporized material is line-of-sight. The vacuum environment also provides the ability to reduce gaseous contamination in the deposition system to a low level. Typically, vacuum deposition takes place in the gas pressure range of 10^{-9} to 10^{-5} mbar depending on the level of gaseous contamination that can be tolerated in the deposition system. The material vaporized from the source has a composition which is in proportion to the relative vapor pressure of the material in the molten source material. Thermal evaporation is generally done using thermally heated sources such as tungsten wire coils or by high energy electron beam heating of the source material itself. Generally the substrates are mounted at an appreciable distance away from the vaporization source to reduce radiant heating of the substrate by the vaporization source. For the PIAD technology a plasma ion source is installed in the center of the reaction chamber. The high energetic ions that are emitted from the source and that are accelerated towards the substrate holder allow to densify the growing layer very effectively without heating of the substrates. The result is the production of consistent film properties over a larger area than that covered with strictly ion sources such as IAD. With IAD, current density is contained within a more restricted solid angle and therefore limited area coverage.

1.5.3 Atomic layer deposition

Although not directly involved in the production of the samples considered in the following chapters, an important technique for multilayer fabrication implemented in this thesis work is the atomic layer deposition (ALD). Introduced by Suntola and Antson in 1977 for the deposition of ZnS thin films [54], is essentially based on a chemical vapor deposition (CVD) process, although the ALD layers are more conformal, homogeneous and controlled. This is due to the cyclic, self-saturating nature of ALD process [55].

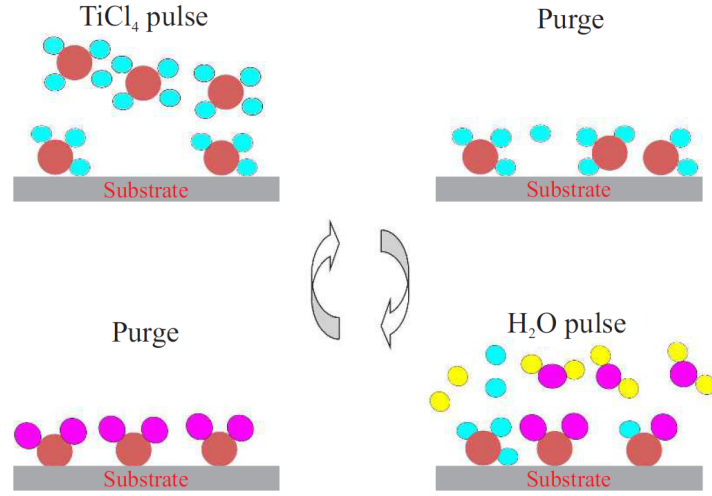


Figure 1.7: Illustration of the TiO₂ coating mechanism by atomic layer deposition with TiCl₄ and H₂O precursors. Reproduced from [56]

During atomic layer deposition a film is grown on a substrate by exposing its surface to alternate gaseous species (typically referred to as precursors) in certain duration so that the material has time to react with the substrate surface. In each of these pulses the precursor molecules react with the surface in a self-limiting way, so that the reaction terminates once all the reactive sites on the surface are consumed. An example of ALD process for TiO₂ film, using TiCl₄ and H₂O precursors, is illustrated in Fig. 1.7. The ALD process is done from two different precursors, i.e., the reactant and the counter reactant. Each material is pulsed in the gas form for a certain time to optimally react. Then the excess material is purged and replaced by an inert carrier such as nitrogen or argon. Regulation of the temperature of the process is essential, since any temperature out of range can lead to poor, defective or non-ALD layers.

The ALD technique provides thin layers of material and its thickness can be controlled by the number of cycles in the atomic scale. The gaseous reaction of the materials with the surface allows a smooth and uniform layer even in vertical surfaces and high aspect ratio patterns. In contrast to chemical vapor deposition,

the precursors are never present simultaneously in the reactor, but they are inserted as a series of sequential, non-overlapping pulses and the process temperature is relatively low [55]. For growing metal oxide layers, H_2O_2 , H_2O , O_3 or O_2 from a plasma can be used as the oxidant. In the case that the reactive oxidant is from a plasma source, the deposition process is called plasma enhanced ALD (PEALD) coating. Application of reactive plasma sources can allow to deposit the layers at lower temperatures and they can be used for less reactive metals.

Chapter 2

Tamm plasmon coupled fluorescence in nanohole structure

2.1 Coupling of emitters with photonic structures

According to the *Fermi's "golden rule"* applied to the decay properties of an emitter, both the emission rate and the direction of emission can be affected by the Local Density of electromagnetic States (LDOS) [57]. The available electromagnetic modes in which photons can be radiated from a specific location are quantified by the LDOS, in analogy with the electronic density of states (DOS). For example, in the case of an ideal point-like emitter in free space, the available modes are the infinite propagating plane waves, that are the eigen-modes of the vacuum. The emission in this case results in a spherical isotropic radiation pattern.

The spatial variation of refractive index near the emitter can strongly modify its emission properties, according to the local photonic band structure [58]. Because of Bragg's diffraction causing constructive or destructive interference along specific directions, the radiation pattern can be angularly dependent [59]. For example, a three-dimensional photonic crystal can completely inhibit the radiative emission for a range of frequencies lying in the complete band gap [60].

In the past, photonic crystals have been employed in order to achieve high directionality of the emission, for application in different field such as biosensing [61] and quantum information [62]. However they suffer from some inherent limitations. First of all, as the electric field distribution associated with the photonic modes is usually distributed inside the high refractive index material [63], the emitter itself has to be buried inside the photonic structure in order to efficiently transfer the energy to the guided modes. This can be a limiting factor especially in sensing applications. Another main disadvantage regarding photonic structure is that the spatial dimensions required are of the order of the wavelength because of the diffraction limit. Resonant metallic nanostructures exhibiting surface plasmons can overcome such limitation. In particular, the exploitation of localized surface

plasmon resonances (LSPRs) on metallic nanoparticles has led to the possibility of localizing an extremely intense electromagnetic field in a deep subwavelength volume, giving rise to the concept of optical nanoantenna [64].

This concept has been widely exploited in many fluorescence-based techniques, where the omnidirectional emission of fluorophores makes it difficult to capture a significant fraction of the total emission. It is well-known that an emitter lying in close proximity with a metallic surface can couple to the surface plasmon, resulting in the so called surface plasmon coupled emission (SPCE) [65]. This effect occurs because of the strong modification of the LDOS induced by the resonant metallic structure. This kind of near-field effect has been used to develop plasmonic nanoantennas [66–70]. Examples include large single-molecule fluorescence enhancements produced by a bowtie nanoantenna made of two closely placed triangle gold nanoparticles [71] and the optical Yagi-Uda antennas that are analogous to a traveling wave phase array antenna and can induce a strong directionality to the coupled fluorescence emission [72]. A nanoaperture surrounded by a periodic set of shallow grooves in a gold film has also been proposed for beaming and sorting the fluorescence emission. For each fluorescence wavelength, the emitted power is oriented along a specific direction with a given angular width, thus enabling a micrometer-size dispersive antenna [73–77]. Periodic plasmonic structures (such as finite-sized hexagonal arrays of nanoapertures milled in gold film) have also been exploited to enable directional emission from single fluorescent molecules in the central aperture [78]. The total emission intensity, integrated over the whole solid angle, is often enhanced many fold as compared to the corresponding total emission from a free-space dipole. This effect is thought to be due to several factors, such as an increased excitation rate due to high light-induced fields in the structures, an increased quantum yield due to increased radiative rates, and a decreased photobleaching [79, 80]. In previous works, controlling the directionality of emission by means of plasmonic elements was demonstrated using complicated metal nanostructures, while these effects were not reported with an isolated metal nanoaperture [78, 81].

In this chapter, the possibility to obtain a highly directional fluorescent emission from a single nanoaperture in a metal film is shown. This effect is obtained by fabricating the nanoaperture on a metallic film deposited on a multilayered dielectric structure exhibiting a photonic band gap, supporting Tamm plasmon polaritons (TPPs) [46, 82] (see Figure 2.4a for a schematic view of the structure). TPPs features, reported in Section 1.4, have already been exploited to obtain coupled fluorescence directed along the surface-normal [83, 84]. However, as the TPP maximum amplitude is located beneath the metallic film, an efficient coupled fluorescence is obtained only if emitters are sandwiched between the top dielectric and the metal coating. This novel nanoaperture-based approach can overcome this geometrical limitation and it does not require spatially extended structures. The nanoaperture can greatly reduce the fabrication requirements and complexity

of metal nanostructures. The main results presented in this Chapter have been published in [85].

2.2 Tamm plasmon polariton coupled fluorescence on flat metallic film

The enhanced density of electromagnetic states at the interface between the dielectric multilayer and the metallic film modifies the emitting properties of a light emitter thereon located [86]. The multilayer design proposed here is composed by six pairs of an high index layer Si_3N_4 ($n_h = 2.13$ at 580 nm) and a low index layer of SiO_2 ($n_l = 1.46$ at 580 nm). The thicknesses are respectively 55 nm and 105 nm. On top of the multilayer, a 200 nm thick layer of silver is deposited. The structure was fabricated by the plasma enhanced chemical vapor deposition technique, described in Section 1.5.1, and it is sketched in the inset of Figure 2.1b. The top Si_3N_4 layer that is in contact with the silver film is about 53 nm thick, which enables the Tamm plasmon resonant wavelength at 580 nm with near-normal incidence. The fabrication was performed entirely by the équipe of Prof. Douguo Zhang. In Figure 2.1a and 2.1b the reflectance maps calculated with transfer matrix method for s-polarization and p-polarization are shown. In contrast to a conventional surface plasmon polariton, optical Tamm states can be formed in both the s and p polarizations. In the inset of Figure 2.1b, the photonic band gap opened by the multilayer structure without the silver film is shown, demonstrating that the Tamm Plasmon dispersion lies in the bandgap region.

As already discussed in Section 1.4, TPP are confined at the interface between the Bragg mirror and the metal film. It is possible to calculate the field distribution inside the structure by implementing the transfer matrix method. In Figures 2.2a and 2.2c the TPP electric field intensity profile of the multilayer design proposed here are reported, for normally incident excitation. As expected from the Reflectivity maps, when the incident wavelength is 580 nm, the TPP mode is excited at normal incidence, while other internal modes are excited at non-normal incidence (Figures 2.2b and 2.2d).

In order to evaluate the near-field coupling of an emitter with the Tamm Plasmon, a 2D FDTD model is implemented using the software Lumerical (Figure 2.3a and 2.3b). The modelling domain is a vertical cross-section of the multilayer and the emitter is placed immediately below the interface between the top Si_3N_4 layer and the silver film. The entire domain is surrounded by perfectly matched layers (not shown in the figure) so that boundary reflection are avoided and the domain resembles an open domain.

The field radiated by the dipolar emitter should match the polarization of the mode in order to have an effective coupling. In the case of the Tamm plasmon mode this is true in both s and p polarizations, since the mode exists in both the

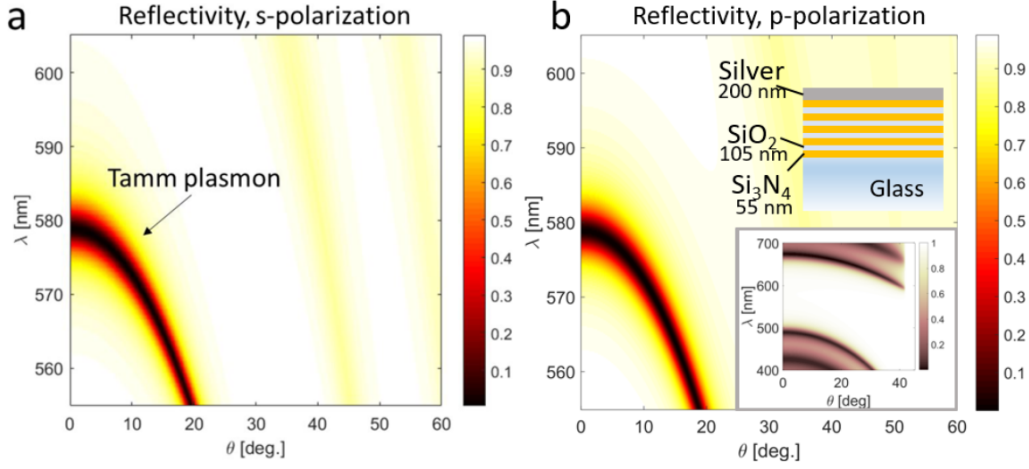


Figure 2.1: **a)** Calculated reflectivity map, for s-polarization, function of the incident wavelength and the angle of incidence with respect to the normal to the surface. **b)** Calculated reflectivity map for p-polarization. Both **a)** and **b)** are referred to the multilayer design sketched in the inset. The band gap opened by the 1DPC (i.e. the multilayer deprived of the top metal layer) is shown in the inset. The TPP dispersion lies inside the band gap region.

polarizations, as seen in the reflectance maps above. It should be noted that an effective near-normal radiation can only happen for the s-polarized dipolar emitter, since the p-polarized emitter does not emit along the dipolar axis.

The modeling result shows that there is a cone of light transmitted through the multilayer into the glass (Figure 2.3a). Such transmission is well understood as the signature of the TPP coupling. In fact, due to the near-zero wavevector of the TPP mode, the TPP coupled fluorescence cannot propagate transversally to the multilayer structure but can only leak into the glass substrate. According to the momentum conservation law, the leakage radiation propagates into the substrate at a specific angle determined by the TPP dispersion relation according to the following relation:

$$k_{TPP} = k_0 n_{glass} \sin(\theta_{TPP}) \quad (2.1)$$

Where k_{TPP} is the TPP wavevector, k_0 is the free-space wavevector, n_{glass} is the substrate refractive index (in this case $n_{glass} = 1.51$) and θ_{TPP} is the leaking angle.

Since TPP are characterized by a well-defined dispersion relation, different wavelengths will couple to TPP with different wavevector and will be therefore out-coupled at different angles. A tool provided by Lumerical allows to compute the far-field distribution. The standard Lumerical Stratton-Chu near to far-field projection technique is applied to project the near-field to a 1 m radius semi-circle

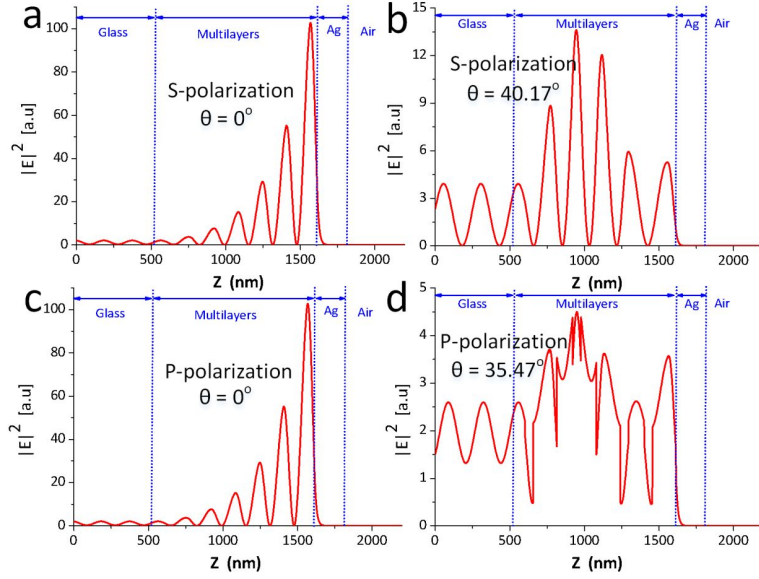


Figure 2.2: Calculated electric field intensity (E^2) distributions within the Tamm plasmon structure, with incident angles fixed at the resonant angle of TPPs (0° in **a** and **b**) and internal mode (40.17° in **b**, 35.47° in **d**). The incident wavelength is 580 nm. The light is s-polarized (**a**, **b**) and p-polarized (**c**, **d**). The optical field distribution of the Tamm plasmon mode is the same for two polarization states. The s-polarized internal mode has a different field distribution from that of p-polarization. Reproduced from [85].

away from the structure in the glass side. A broadband excitation pulse corresponding to a band of different oscillating frequencies has been set for the dipole in the simulation, and the corresponding far-field radiation pattern has been computed for each of them. In the polar plot in Figure 2.3c and 2.3d, three exemplary calculated far-field patterns at three different wavelengths are presented where a change in the output angle is observable. Away from the wavelength corresponding to near-normal radiation (580 nm), the radiation is no more directed to the normal direction.

2.3 Coupling of fluorophores in single nanoapertures

As reported in the previous Section, TPPs are characterized by an electromagnetic energy distribution that is highly localized at the interface between the metallic film and the multilayer and have close-to-zero in-plane wavevector components (k_{TPP}) at certain wavelengths. Nanoapertures in the metallic film are

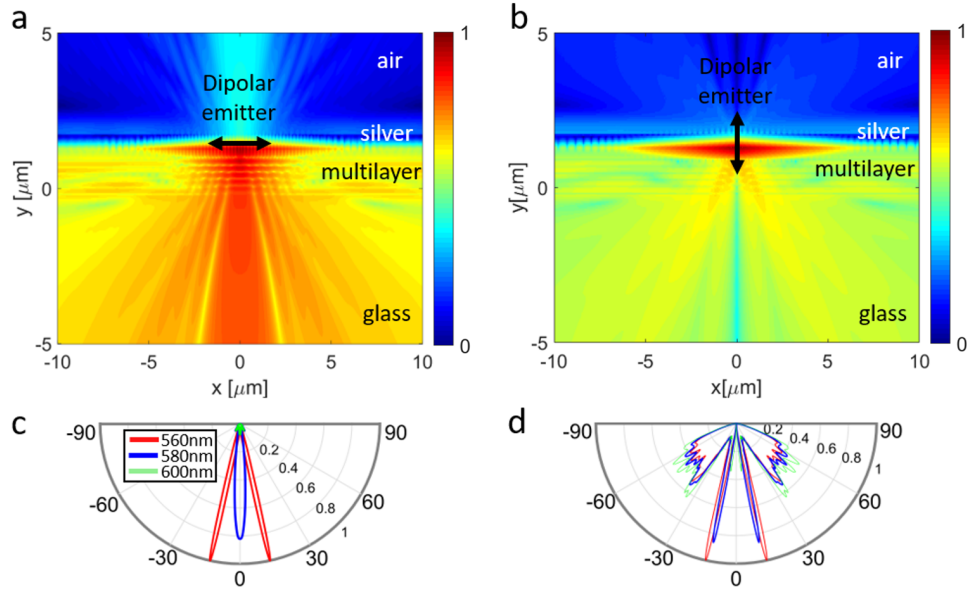


Figure 2.3: Calculated near-field distribution of the electric field intensity radiated by an emitter modeled with a dipole. The dipole axis is **a)** parallel or **b)** normal to the surface plane, showing no emission normally to the surface in **b)**. **c)**, **d)** Calculated far-field radiation pattern corresponding to the near-field distribution in **a)** and **b)** for different radiated wavelengths. The radiation pattern shows the dispersive behaviour of the TPP-coupled fluorescence and the highly directional emission in **c)**.

thus necessary in order to guarantee an efficient coupling of the emitters, that must be sandwiched between the metallic coating and the top dielectric otherwise. Nanoapertures are fabricated by focused ion beam milling in silver films. Figure 2.4 presents the experimental configuration (a) together with scanning electron microscopy (SEM) view of the sample (b). The silver essentially eliminates transmission through the structure and confines the observation volume to the isolated aperture. The diameter (D) of the aperture is about 620 nm. Also, several diameters (D) of the aperture are considered in the subsequent experiments. An ethanol solution containing fluorescent molecules (rhodamine B, RhB) with 10^{-4} M concentration was spotted on top of the sample to fill the aperture. The excitation laser light is focused from the bottom of the sample (glass substrate) by means of a NA= 1.35 oil immersion objective (Figure 2.5). The illumination wavelength is set at 532 nm and the polarization is linear. To analyze the angular fluorescence emission, the fluorescence intensity distribution is collected by means of back focal plane (BFP) imaging onto a scientific camera (Andor, Neo sCMOS). The experiment was entirely conducted by the équipe of Prof. D. Zhang and Prof. J. R. Lakowicz.

In BFP images, the fluorescence intensity is distributed according to the emission direction. More specifically, the radial coordinate scales as $n \sin(\theta)$, where n is the refractive index of the external medium [87, 88] and θ is the polar emission angle with respect to the optical z -axis. In the setup, an oil-immersion objective is used, therefore, $n = 1.515$ (refractive index of the oil matched that of the glass substrate) and the polar angle θ is the fluorescence emission angle in the oil medium. Upon averaging over the azimuthal angle, fluorescence radiation patterns can be calculated as a function of the polar angle θ . Another CCD (Lumenera's INFINITY2-1M digital CCD camera) is used for front focal plane (FFP, or direct space) imaging. In the measurements, rhodamine B (RhB) dyes are used. The fluorescence spectrum (Figure 2.4d) collected by means of a spectrometer (ihR 550, HORIBA Scientific) is a broad one, typical for the RhB emission. To collect spectrally resolved fluorescence images from the TPP structure, three bandpass filters are used, with center wavelengths at 560 ± 2 , 580 ± 2 , and 600 ± 2 nm (full width at half-maximum = 10 ± 2 nm).

2.3.1 Angular distribution of radiation in far field

Experimental FFP and BFP images with a single nanoaperture ($D = 620$ nm) at three selected fluorescence wavelengths are presented in Figure 2.6. The FFP images clearly show that the fluorescence is only emitted from the nanoaperture location, thus demonstrating that silver film is thick enough to block the fluorescence from emitters outside the aperture. The BFP images display remarkable differences with the three selected emission wavelengths. At wavelength of 580 nm, a beam surrounded by a ring at a larger angle is observed. At 560 nm, the central

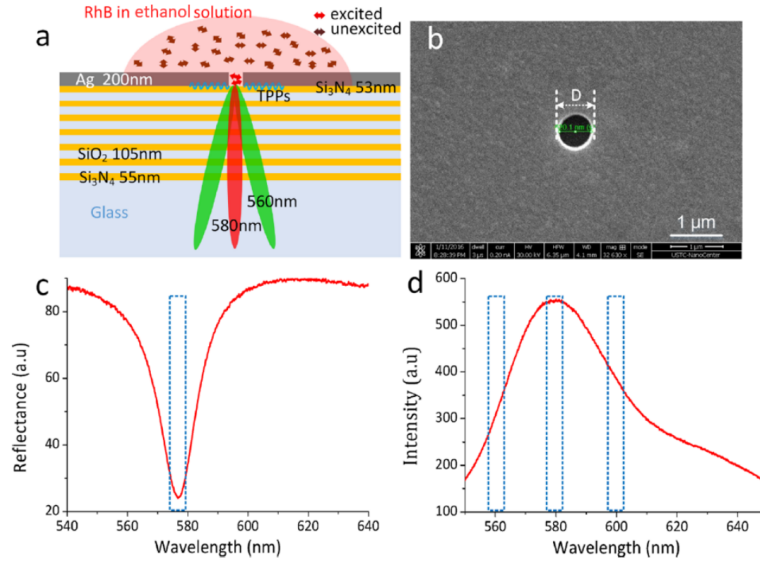


Figure 2.4: **a)** Schematic view of the Tamm plasmon structure. Rhodamine dyes in a solution of ethanol are spotted on top of the sample to fill the nanoaperture. **b)** SEM image of the metal aperture milled in a silver film 200 nm thick. The diameter (D) of the aperture is about 620 nm. **c)** Reflection spectrum from the sample shows a dip located at 577 nm wavelength. **d)** Fluorescence spectrum of the RhB molecules dissolved in ethanol solution. The peak wavelength is located at 580 nm. Three narrow bandpass filters with wavelengths at 560, 580 and 600 nm were used to select fluorescence wavelength. The filters spectral width is 10 nm. Reproduced from [85].

beam expands to a ring, whereas at 600 nm, no central beam is found.

To better evaluate the differences in the radiation patterns, a polar plot (Figure 2.6g) of radiated flux per solid angle (θ) is reconstructed by averaging the radiated power over the azimuthal angle (ϕ). In the data processing, the fluorescence intensity on the positions of the same polar angle (θ) but with different azimuthal angle (ϕ , ranging from 0° to 360°) will be summed, then this sum represents the fluorescence intensity at this selected polar angle (θ) as shown in Figure 2.6g. The angular resolution of the objective is estimated to be 0.2° . A narrow beam with an angular width of about 19.4° (full width at half-maximum) appears in the direction normal to the glass for emission wavelength at 580 nm. At 560 nm emission wavelength, the fluorescence is directed at a polar angle $\theta = 17.6^\circ$, with an intensity minimum along the direction normal to the sample surface. Based on previous works [83, 84], emission peaks at 0° ($\lambda = 580$ nm) and 17.6° ($\lambda = 560$ nm) correspond to the Tamm plasmon coupled emissions (TPCEs), where TPPs are confined between the metal film and the dielectric multilayers. The emission peaks at 32.6° (for $\lambda = 580$ nm) and 38.8° (for $\lambda = 560$ nm) are associated to fluorescence coupled to internal modes

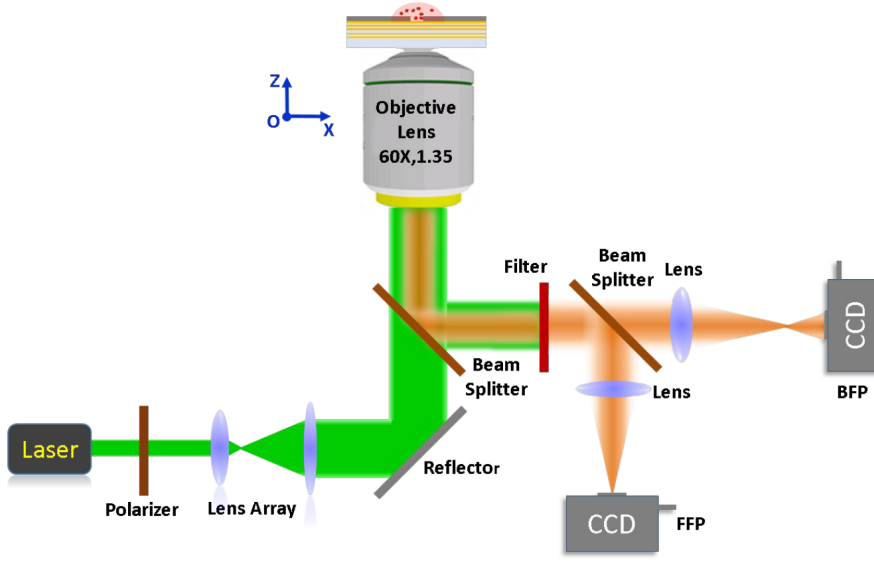


Figure 2.5: Schematic of the experimental setup. A laser beam at 532 nm wavelength is expanded by a lens array to fully fill the rear aperture of an oil immersed objective (60X, NA= 1.35). A linear polarizer is put after the laser source. The emission from the sample is collected by the same objective and then directed into two cameras. One is used to record the fluorescence intensity distribution on the back focal plane of the objective and the other is for the front focal plane image. Three band pass filters with center wavelengths at 560, 580 and 600 nm are used to select the fluorescence at particular wavelength to reach the two detectors. Reproduced from [85].

of the dielectric multilayer (referred to as internal mode coupled emission, IMCE). The IMCE angles are determined by the mode in-plane wavevector components at the corresponding wavelengths. Similarly, because of the small in-plane wavevector components of TPPs, the observed TPCE is directed almost normally to the sample. In fact, at $\lambda = 580$ nm, the dominant Tamm plasmon resonant angle (TPRA) is nearly 0° . The TPRA increases as the fluorescence wavelength decreases. For example, at $\lambda = 560$ nm, the observed TPRA is 17.6° [89]. On the other hand, if the fluorescence wavelength increases, for example, at $\lambda = 600$ nm (Figure 2.6f and 2.6g), the corresponding TPP coupled emission disappears, as no Tamm plasmons are available at this wavelength. The changes of TPRA with the wavelength are consistent with the calculated angle-dependent reflectivity curves (Figure 2.1), where the TPRA is 17.3° (for p-polarization) or 18.1° (for s-polarization) for 560 nm wavelength and 0° for 580 nm wavelength. The structure does not support Tamm plasmons at $\lambda = 600$ nm and no resonant dip appears at that wavelength. The optical field of internal modes is mainly confined inside the dielectric multilayer

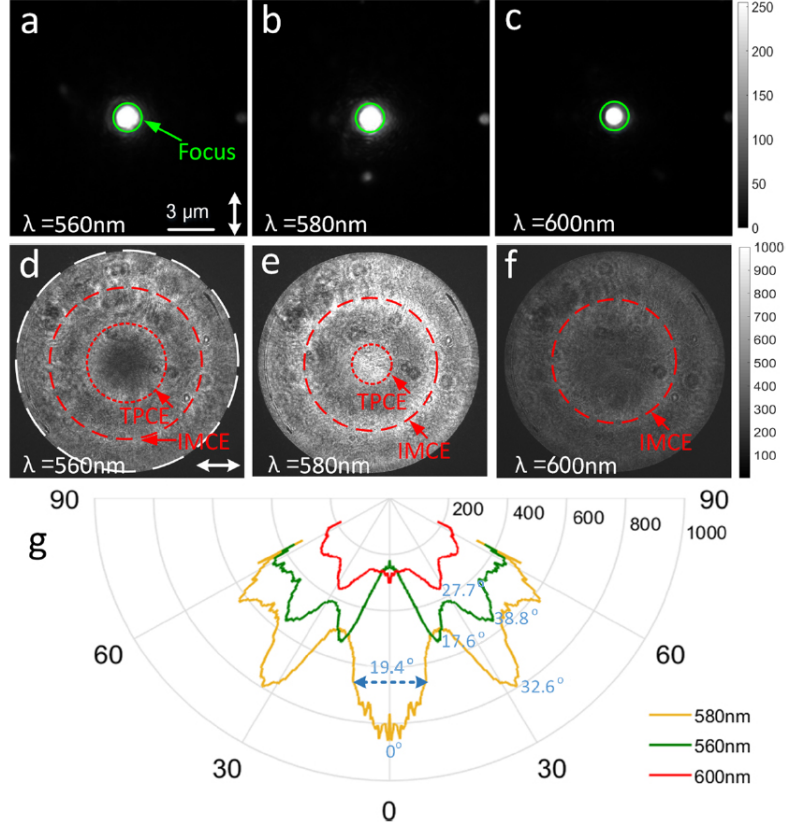


Figure 2.6: FFP fluorescence images from the sample at three selected wavelengths, 560 nm **a**), 580 nm **b**), and 600 nm **c**). **d**), **e**), and **f**) are the corresponding BFP images. Arbitrary units are used for the colorbar. The green circles on **(a-c)** label the focused spot of the excitation laser beam (532 nm wavelength). The white dashed circles on **d**) represent the largest collection angle ($\theta = 63^\circ$) determined by the NA of the objective (1.35). The short red dashes represent Tamm plasmon coupled emission (TPCE) and the long red dashes internal mode coupled emission (IMCE). The polar angles (θ) of TPCE and IMCE are 17.6° and 38.8° **d**) and 0° and 32.6° **e**), respectively. For the wavelength at 600 nm, only IMCE appears at 27.7° . **g**) Angular radiation patterns in the polar angle (θ) as derived from BFP images (**d-f**). The arrows (**a**, **d**) show the polarization of the incident laser beam (vertical direction for FFP images and horizontal direction for BFP images). The angular resolution of the objective is estimated to be 0.2° . Reproduced from [85].

(Figure 2.2b, 2.2d), with evanescent tails leaking out in the outer medium. However, a weak coupling of fluorophores with the internal modes is still observed. These experimental results demonstrate that the interplay of a single aperture in a metallic film with a dielectric multilayer may result in a directional sorting of the fluorescence emitted by dyes within the aperture itself, whereas no significant directional feature is observed for nanoapertures on metal-coated glass substrate [78, 81]. More importantly, the results shown in Figure 2.6 indicate that emitters can still couple with Tamm plasmons without being necessarily located underneath the metal film.

Experimental results are well supported by rigorous calculations. The near-field interaction of the emitter with the structure is investigated by means of 3D FDTD model (Lumerical Inc.). Single dipoles are placed at the bottom of a 600 nm diameter aperture, in a central position, with dipole momentum oriented either perpendicular (vertical) or parallel (horizontal) to the sample surface. Upon calculation of the near-field energy distribution in a close volume surrounding the sources, a far-field projection is performed to get the free-space emitted power in the glass half-space. Results are shown in Figure 2.7. When dealing with horizontally oriented dipoles, the radiation patterns presented in Figure 2.7a-c are calculated by averaging the emitted power from multiple dipoles having momentum laying on the sample surface with a varying azimuthal orientation over a 2π range. In this way, the axial symmetry about the dipole momentum of the emitters is eliminated. Moreover, azimuthally homogeneous intensity distributions, that provide a closer picture to the experimental observations, are obtained. The FDTD calculations have been performed by considering emitters with a well-defined orientation and position with respect to the nanoaperture to illustrate the coupling mechanism with photonic and plasmonic modes of the structure. It is worth recalling, however, that the experimental observations are related to RhB molecules in ethanol, which are continuously moving and rotating at random, in time. At $\lambda = 560$ nm (Figure 2.7a,d), both horizontal and vertical dipoles are shown to contribute to TPCE at leakage angles according to the Tamm plasmon dispersion curve for s- and p-polarizations (see Figure 2.1). At $\lambda = 580$ nm, Tamm plasmons have small in-plane wavevector components and an electric field oriented mainly parallel to the multilayer surface. Therefore, horizontally oriented dipoles will preferentially contribute to TPCE (Figure 2.7b), which is angularly distributed within a narrow beam about the surface normal. Vertically oriented dipoles are substantially polarization-mismatched with TPPs, thus resulting in a weak TPCE (Figure 2.7e). At $\lambda = 600$ nm, no Tamm plasmons are available (see Figure 2.1) and all dipoles weakly couple to internal modes of the multilayer, depending on their polarization orientation (Figure 2.7c,e).

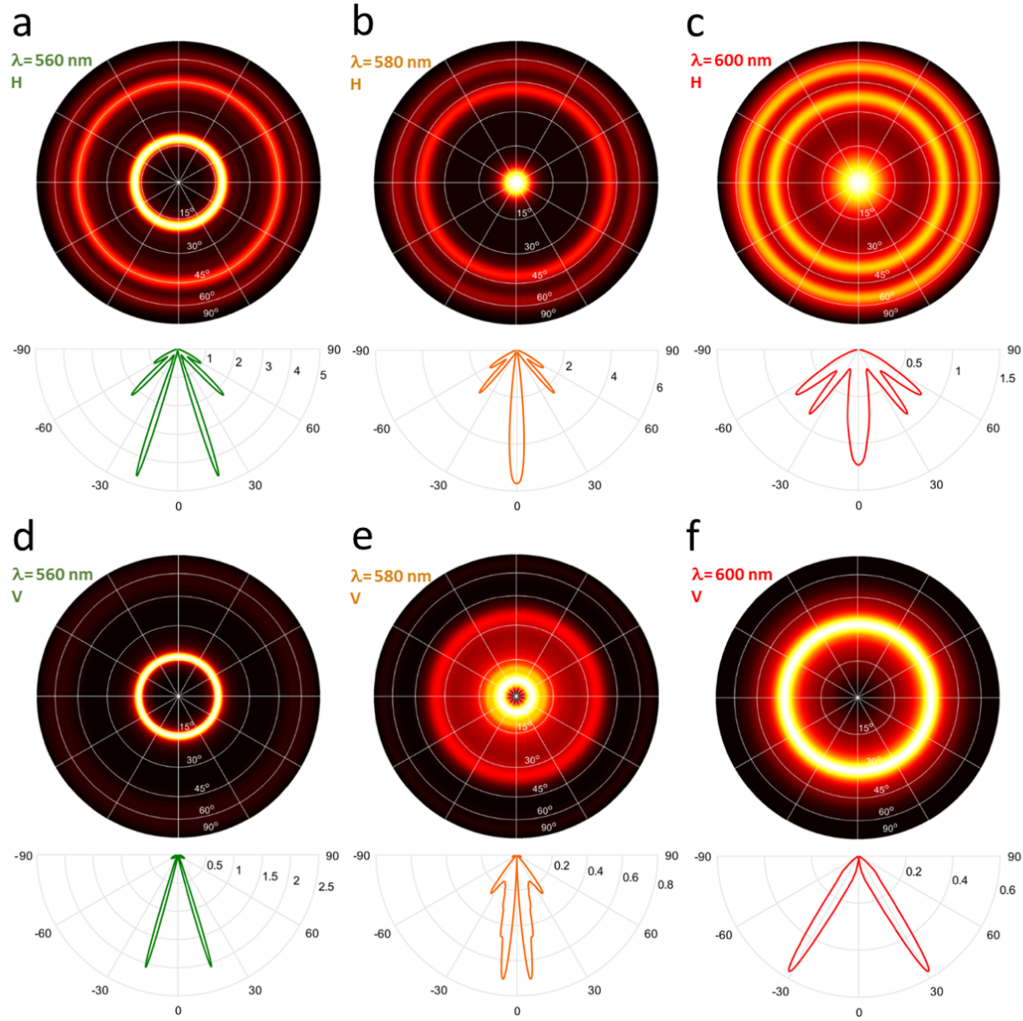


Figure 2.7: Calculated angularly resolved (normalized) power emitted at 560, 580 and 600 nm wavelength in the glass substrate from horizontally oriented dipoles (a-c) and vertically oriented dipoles (d-f) placed within a 600 nm diameter aperture. Reproduced from [85].

2.3.2 Effect of the diameter of the nanoaperture

In the following experiment, four isolated apertures with diameters $D = 200, 400, 800$ and 1000 nm are investigated to show the effect of the aperture diameter on the directional coupled emission. Nanoaperture SEM micrographs, FFP and the corresponding BFP fluorescence images are shown in Figure 2.8. The emission radiation patterns from single apertures are also shown, as observed on the BFP. For aperture having $D = 200$ nm, the IMCE is suppressed relative to the TPCE at $\lambda = 560$ nm and 580 nm, and only one emission peak (TPCE) is dominant in the radiation pattern (Figure 2.8 a). With an increasing aperture diameter, the IMCE becomes stronger and finally approaches the intensity of TPCE in the case of $D = 1000$ nm (Figure 2.8 d).

This effect can be explained by assuming that coupling with TPPs occurs preferentially in proximity of the bottom aperture boundaries, close to the lateral metallic walls. Instead, all dipoles filling the inner area of the aperture will preferentially couple with the multilayer internal modes or directly to the free space, as TPPs are not available anymore. As a result, for an increasing aperture diameter, the TPCE intensity is expected to increase proportionally, but the relative TCPE intensity over the total emission intensity follows an opposite trend. Apart from a change of the intensity ratio between TPCE and IMCE, the TPCE angular width at 580 nm wavelength is also increased gradually with increasing diameter. The minimum angular width is 12.5° , observed at $D = 200$ nm (Figure 2.8 a). Differently from previous reports on plasmonic antennas that can direct the fluorescence beam along a specific direction for each emission wavelength, in this case, fluorescence is directed along two specific directions (TPCE and IMCE). The influence of the aperture size on the directional sorting of fluorescence emission provides a means to control the intensity ratio of fluorescence beams along the two specific directions by tuning the relative weights of TPCE and IMCE.

2.3.3 Effect of the shape of the nanoaperture

Finally, triangular and squared apertures are demonstrated to control the fluorescence emission. One of the advantages of single nanoapertures in manipulating the fluorescence emission is that single apertures can be fabricated with low cost over large scale for high-throughput sensing. Each aperture can work as a single antenna to manipulate the fluorescence emission, and the aperture array can be seen as a set of parallel antennas. The advantage of this arrangement is investigated by considering two arrays of 5×5 triangular and square nanoapertures, as shown in Figure 2.9a,e. The side length is 804 nm for the triangular and 532 nm for the square aperture, which results in nearly equal area for both types. The period of the aperture arrays is $1.5 \mu\text{m}$, which is larger than the Tamm plasmon propagation length l in the wavelength range of rhodamine B emission. The propagation length

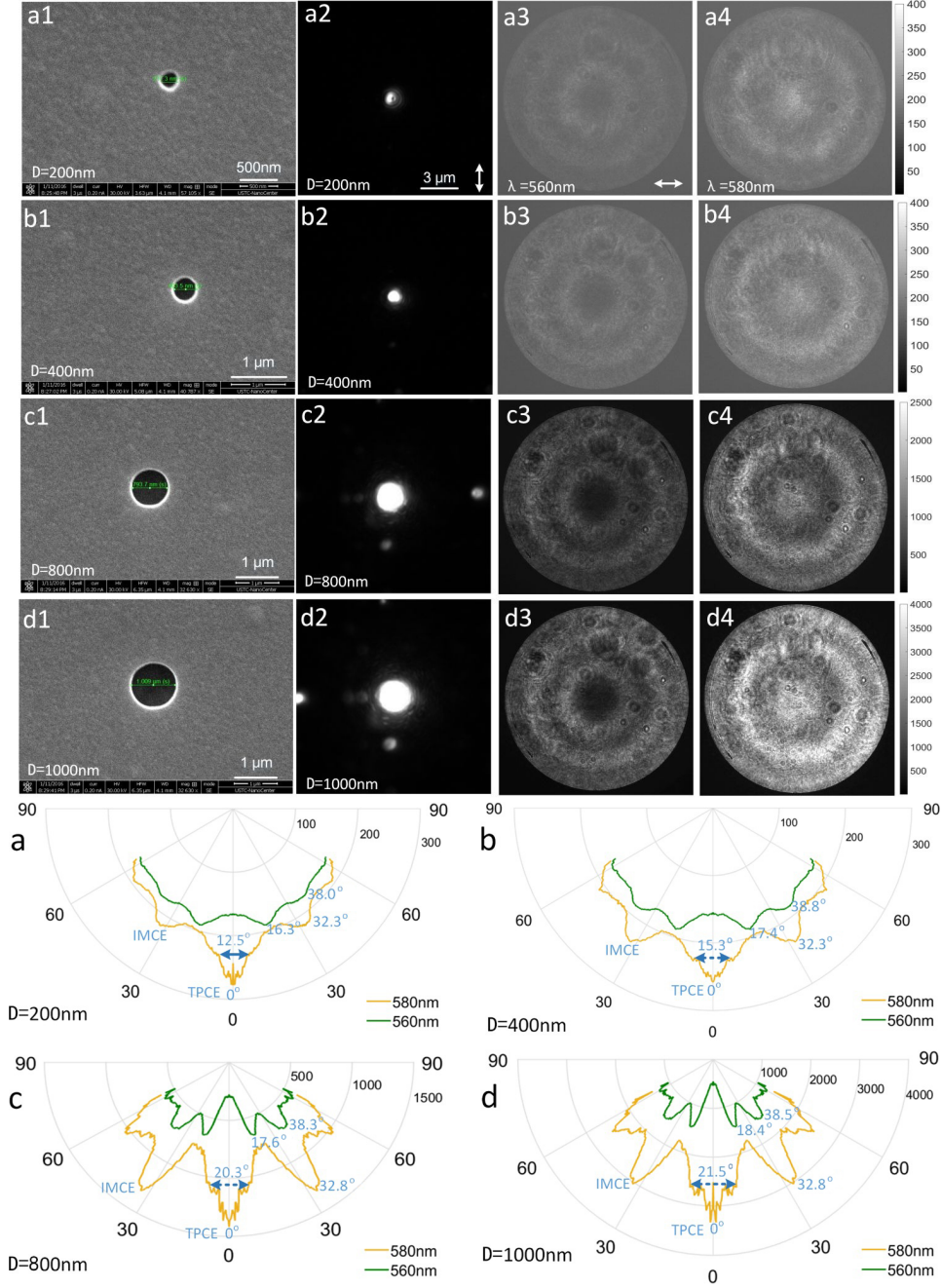


Figure 2.8: SEM images, FFP and BFP fluorescence images from the single nanoaperture with diameter D of about 200 nm (a1-a4), 400 nm (b1-b4), 800 nm (c1-c4), 1000 nm (d1-d4). Arbitrary units are used for the colorbar. Two band pass filters with center wavelengths at 560 nm and 580 nm are used. The arrows (a2, a3) show the polarization of the incident laser beam (vertical direction for FFP images and horizontal direction for BFP images). a)-d) Angular radiation patterns in the polar angle (θ) from single nanoaperture with diameter D of about 200 nm (a), 400 nm (b), 800 nm (c), and 1000 nm (d). Adapted from [85].

of the Tamm plasmon grows as the propagation constant increases [90] and it is estimated to be $l \approx 1.1 \mu\text{m}$ for the highest propagation constant available for coupling within the spectra of rhodamine B emission. The excitation laser beam was focused onto the central aperture of the two arrays (Figure 2.9b,f). The FFP fluorescence images show that the maximum of fluorescence intensity is associated to the central aperture. The BFP images at two selected fluorescence wavelengths (560 nm (Figure 2.9c,g) and 580 nm (Figure 2.9d,h)) are similar to Figure 2.6d,e. Despite a different shape, TPCE is beamed normally to the sample (at 0°) for 580 nm and at 20.0° for 560 nm emission (Figure 2.9i,j).

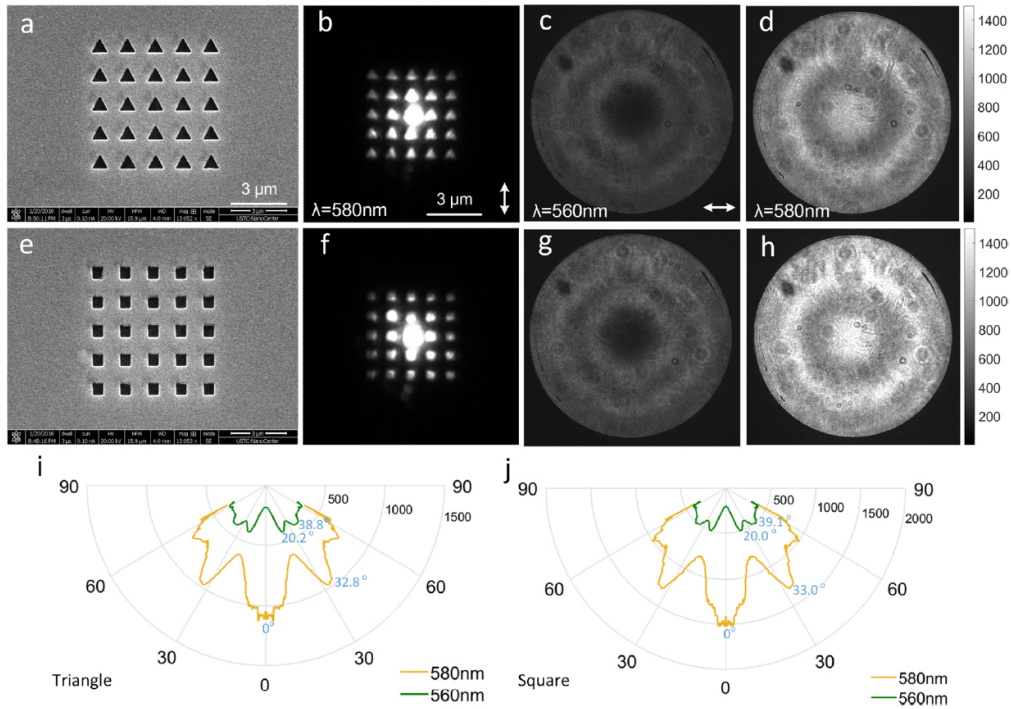


Figure 2.9: SEM images (a, e), FFP (b, f), and BFP (c, d, g, h) fluorescence images from the samples with 5×5 apertures array. The apertures are filled with ethanol solution of rhodamine B. The nanoapertures have a triangular shape with side length 804 nm (a-c) and a square shape with side length 532 nm (d-f). (i, j) The radiation patterns derived from the corresponding BFP images, (c, d) and (g, h), respectively. The arrows (b, c) show the polarization of the incident laser beam (vertical direction for FFP images and horizontal direction for BFP images). Arbitrary units are used for the colorbar. Adapted from [85].

This observation suggests that the angular dispersion of the coupled emission is independent of the aperture shape, as far as dye molecules can be near-field coupled to the Tamm plasmon confined beneath the silver coating. In the experiment, if the laser beam is focused into other apertures of the array, the radiation pattern does

not change, meaning that each aperture can work independently as an individual antenna. If the distance between each aperture is further increased to several micrometers, the eventual coupling between apertures can be totally ignored. Because the angular distributions are the same for a single aperture and the 5×5 aperture arrays, the overall TPP resonance was not significantly affected by the selective removal of metal corresponding to each aperture. This is a favorable result of the use of these structures in DNA sequencing or other highly multiplexed assays.

2.4 Conclusions

The present results, fruit of the collaboration with Prof. D. Zhang and Prof. J. R. Lakowicz, significantly extend the scope of previous observations concerning fluorophores coupled to Tamm plasmon structures [89, 91–93]. In those works the fluorophores were located under a continuous metal film. Embedding molecules below the metal film is not favorable for applications in fluorescence sensing or imaging, especially for liquid samples. In this chapter it is demonstrated that coupling can also occur when fluorophore is located within the apertures in the metal film of a Tamm structure, regardless of the aperture shape. In this configuration, fluorescent probes can be located inside the metal aperture without necessarily being buried below the metal film. The aperture can also be filled with probes at different emission wavelengths to implement a high-throughput sensing.

Chapter 3

Bloch surface wave cavity for spontaneous emission decay rate enhancement

Since the pioneer work of Purcell [94] it is well known that the emitting properties of a light source can be strongly modified by the photonic environment. If an emitter couples to a resonator, its spontaneous emission rate (SE, inverse of the relaxation time) is governed by the quality factor (Q) and modal volume (V) of the resonator. The Purcell factor $F_p = \gamma/\gamma_0 \propto Q/V$ quantifies the enhancement of the spontaneous emission rate γ compared to its free space value γ_0 . The spontaneous emission can be also inhibited in a photonic crystal, as Yablonovitch proposed in 1987 [1], since no mode is supported in the band gap. His work was notably motivated by elimination of unwanted spontaneous emission in semiconductor lasers or solar cells. He also discussed the possibility to improve laser emission by restricting the spontaneous emission to a chosen electromagnetic mode. This has opened the way to fluorescence control in optical microcavities with applications as bio-chemical sensing, photovoltaic systems, quantum cryptography and light nanosources (for a review, see [95] and [96]). The main results presented in this Chapter have been published in [97].

3.1 Purcell factor

Let us take a closer look at two parameters Q and V , which will play an important role through this chapter. The quality factor Q is defined as the ratio between optical energy stored in the cavity and energy loss per-oscillation cycle. It also determines the linewidth in frequency of the resonance. A mathematical expression can be written as:

$$Q \propto \frac{\text{Energy stored in cavity}}{\text{Energy dissipation per oscillation cycle}} \approx \frac{\omega_0}{\Delta\omega} \approx \frac{\lambda_0}{\Delta\lambda} \quad (3.1)$$

where ω_0 , λ_0 are resonating angular frequency and wavelength of the cavity and $\Delta\omega$, $\Delta\lambda$ are the linewidth in frequency and wavelength domain.

The modal volume V characterizes the electric field confinement of a specific optical mode and can also be expressed as:

$$V = \frac{\iiint |E_n|^2 d\mathbf{r}}{\text{Max}(|E_n(\mathbf{r}_n)|^2)} \quad (3.2)$$

where E_n is the electric field associated to the n^{th} optical mode, with the maximum at the n^{th} mode antinode \mathbf{r}_n . A very interesting point is that Q and V , that are properties of the cavity mode independently of the emitter properties, can describe the light-matter interaction in a cavity and quantify the Purcell factor. To understand how this can be true, we can refer to Fermi's golden rule, according to which the spontaneous emission decay rate in a cavity can be expressed as a function of the partial local density of states (P-LDOS) of the cavity at the emitter position \mathbf{r} :

$$\frac{\gamma(\mathbf{r})}{\gamma_0} = \frac{\rho_i(\mathbf{r}, \omega)}{\rho_i^0(\omega)} \quad (3.3)$$

In this expression, $\rho_i(\mathbf{r}, \omega)$ is the partial local density of states, according to the dipole orientation ($i = x, y, z$), and $\rho_i^0(\omega) = \rho^0(\omega)/3 = \omega_0^2/(3\pi c^3)$ is the free space P-LDOS (units $s \cdot m^{-3}$). Finally, the LDOS is the key parameter to describe spontaneous emission in a cavity. It is possible to show that the spectral shape of the P-LDOS is explicitly related to the Q factor and the spatial shape is explicitly related to the mode volume V . A full treatment of the Purcell factor in a medium of optical index n_1 leads to [14]

$$F_p = \frac{\gamma}{n_1 \gamma_0} = \frac{3}{4\pi^2} \left(\frac{\lambda}{n_1} \right)^3 \frac{Q}{V} \quad (3.4)$$

where γ refers to the coupling to a given bound mode of the cavity (so that the mode volume can be defined). By looking at this formula, it is clear that the highest light-matter interaction in a cavity, and so the highest Purcell factor, is achieved for high Q/V ratio.

3.2 State of the art for optical resonators for Purcell effect

Figure 3.1 shows estimated Q and V values for various optical resonator devices. On the top right corner are dielectric microcavities, subject of intensive studies since decades [8, 10, 97–116]. Optical microcavities exhibit huge resonance qualities ($Q > 1000$ and up to 10^9) enabling to reach high Purcell factors. Nevertheless, they present the main disadvantage to badly confine optical modes. In fact, the mode confinement is diffraction limited. Dielectric optical cavities are able to enhance the emission drastically ($F_p > 100$) given the high quality factors of their resonances. Anyway the high quality factors are often achieved at the expense of the mode volume.

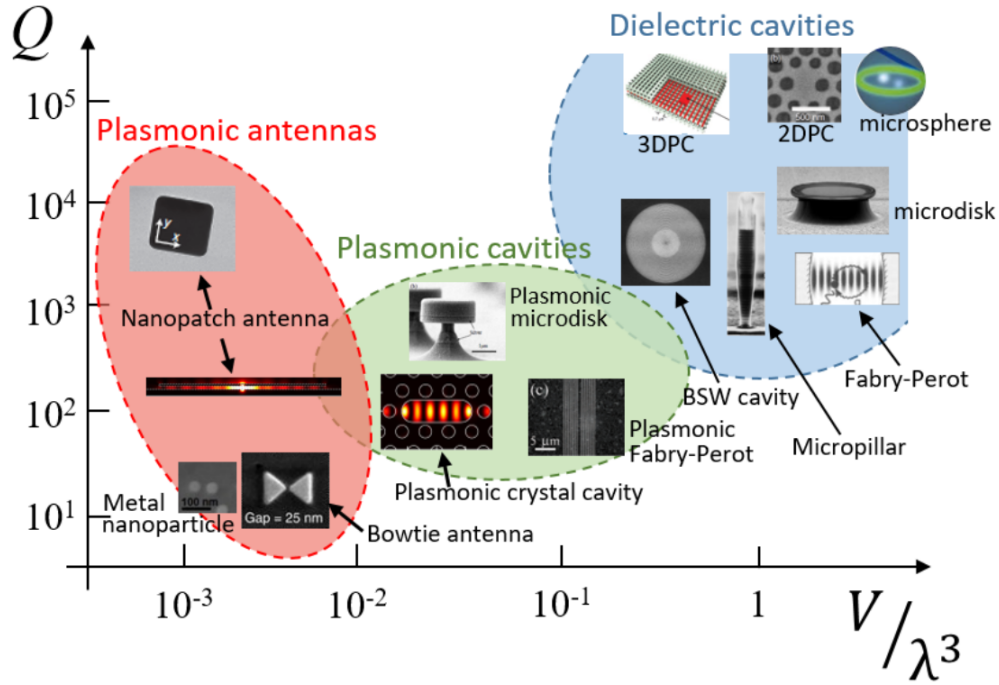


Figure 3.1: Overview on typical Q and V values for various kinds of optical resonators. Adapted from [10, 97, 98, 111, 117–121]

In order to overcome these limitations, plasmonic nanostructures are a promising alternative. With the ability of concentrating light within the sub-wavelength scale, plasmonic cavities are capable of exploring light-matter interactions in a regime that cannot be achieved with dielectric structures. Several kinds of dielectric resonators have been transposed into plasmonic paradigm in last decades, exploiting the sub-wavelength domain with structures such as plasmonic crystal cavities [117, 122], surface-plasmon whispering gallery resonators [123–126], and

other plasmonic cavities [118, 127, 128]. Some of these devices are shown in figure 3.1, where they occupy the central region with relatively small Q factors but very small modal volume. However, applications of these plasmonic cavities are strongly limited by the lossy nature of metals and the metal-induced quenching effect. Therefore, a plasmonic cavity must be designed and modified with a clear purpose for the application.

The smallest modal volumes are achieved by plasmonic nano-antennas. Nano-antennas have the ability to concentrate optical field into a volume as small as $10^{-3}\lambda^3$, hence provide strongly enhanced light-matter interaction at the field maximum [71, 119–121, 129–131]. However, the lossy nature of the metal eliminates the possibility for forming extremely high Q plasmonic cavities. Therefore, instead of being designed to confine the fields for a long time, these resonators are usually designed to couple well with radiation modes so they can either concentrate incident fields into a small spot or guide emission from molecules in the device to free space radiation. They usually have relative low Q (< 10), as shown in the bottom left corner of Figure 3.1. The fact that the Q is so low for these antennas allows broad band emission enhancement but at the cost of their frequency selectivity. Finally, an important class of devices to manage the spontaneous emission at the nanoscale introduced recently are based on metamaterials [45, 132–135].

3.2.1 The concept of Bloch surface wave cavity

So far, we have seen there exist two widespread approaches to target the management of light emission, based on plasmonic structures and dielectric photonic cavities. Both approaches have demonstrated a high potential in controlling spectral, angular and temporal features of the emission, exhibiting rather complementary advantages, and many efforts are nowadays undertaken to find hybrid solutions taking the best from the two sides. However, in order to reach higher Purcell factors for SE, the emitters have to be located in close proximity of the LDOS local maxima [9]. In dielectric PCs, this might be difficult to attain, as photonic modes are preferentially confined within high-index regions of the structure, [10] with only evanescent tails leaking in the surrounding medium. In plasmonic resonators, although high LDOS can be produced at dielectric/metallic interfaces, a main limitation is found in the strong absorption at visible wavelengths [136]. When dealing with nanoresonators, a general issue is represented by the typically low directionality of the power radiated in free space. Although individual objects, such as metallic resonant nanostructures [71, 129], can be designed to shape their angular radiative pattern, an accurate control on the coupled-emission direction can be achieved by employing more spatially extended [137, 138] or periodic structures.

In this chapter I will illustrate an original concept for enhancing the radiative decay rate and directing the emission of organic dyes located on the surface of a

patterned dielectric multilayer stack. The multilayer (also referred as one dimensional photonic crystal, 1DPC) supports Bloch surface waves (BSW), discussed in Section 1.3, which are exploited as a mean to resonantly transfer energy from emitters to free-space, through a resonant coupling effect. The high energy confinement of BSW on top of properly designed multilayers [139] can be particularly advantageous to exploit coupling effects involving nanosources or absorbers deposited on the surface [35, 39–45], for example, in sensing applications [140, 141]. In the present case, BSWs are exploited for a 2-fold goal, namely, to enhance the decay rate of fluorescent molecules within a surface circular cavity and to deliver the radiated coupled power away from the cavity region toward a diffractive element for further free-space out-coupling.

3.3 Bloch surface wave coupled fluorescence on flat multilayer structure

The 1DPC consists of a dielectric multilayer made of a stack of Ta₂O₅ (high refractive index) and SiO₂ (low refractive index) layers, deposited on a glass coverslip (150 μm thickness) by plasma ion-assisted deposition under high vacuum conditions (APS904 coating system, Leybold Optics). The stack sequence is substrate–[Ta₂O₅–SiO₂] × 10 – Ta₂O₅ – SiO₂–PMMA with 23 layers in total, including PMMA. The Ta₂O₅ layer (refractive index $n_{\text{Ta}_2\text{O}_5} = 2.08$) is 95 nm thick, and the SiO₂ layer (refractive index $n_{\text{SiO}_2} = 1.46$) is 137 nm thick. The top SiO₂ layer on top of the stack is 127 nm thick. On top of the structure is a 75 nm thick layer of dye-doped PMMA that is spun for pattern fabrication ($n_{\text{PMMA}} = 1.48$). The multilayer supports TE-polarized BSW localized at the top interface, at wavelengths below 600 nm. BSWs are tightly bound to the surface and can propagate for several hundreds of microns, as the number of stack layers is large enough to reduce significantly losses due to radiation leakage through the glass substrate [142]. In figure 3.2a and 3.2b the reflectance maps calculated with transfer matrix method for TE-polarized BSW for bare multilayer and PMMA-topped multilayer is shown. The deposition of the PMMA layer redshifts the BSW dispersion curve by virtue of the well known dielectric loading effect [36]. In the inset of figure 3.2b, a cut of the map at a fixed wavelength ($\lambda = 570$ nm, along the blue dashed line) shows that the resonance has a FWHM of ~ 0.05 degrees. The width of the resonance is ultimately associated to the overall losses and, consequently, to the decay length of the mode. A cross section of the electric field distribution along the structure (figure 3.2c and 3.2d, flat and PMMA-topped respectively) puts in evidence that the mode has its maximum in close proximity to the truncation interface and that it is exponentially decaying in the air. Moreover the redshift of the dispersion due to the presence of PMMA provides more confinement to the mode, as the dispersion lies more deeply into the photonic band gap of the 1DPC at $\lambda = 570$ nm.

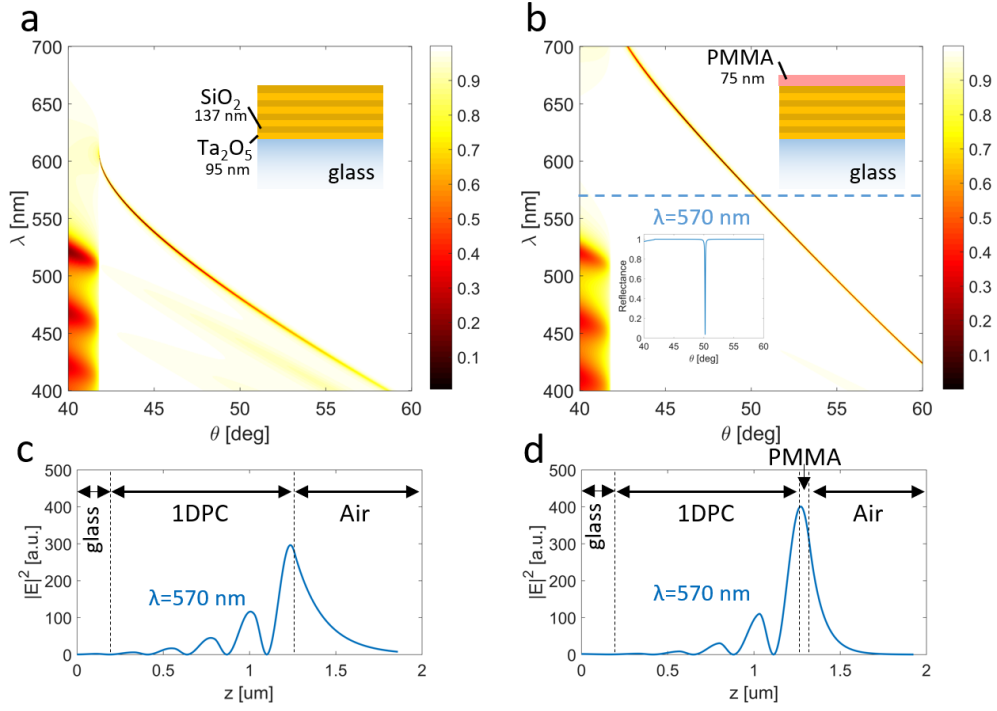


Figure 3.2: Calculated reflectivity map for TE-polarized BSW, bare multilayer and PMMA-topped multilayer **a)** and **b)**, respectively. In the insets, the sketches of the multilayer structures. A cut of the dispersion relation in **b)** at $\lambda = 570$ nm is reported in the inset of **b)**. In **c)** and **d)** the BSW electric field intensity profile along the orthogonal direction with respect to the multilayer surface are reported.

It is possible to evaluate the near-field coupling of an emitter with BSW by modeling the system in 2D FDTD model implemented in "FDTD Solutions" by Lumerical, as already shown for the case of coupling to Tamm plasmon in Section 2.2. The field radiated by the dipolar emitter can couple to the BSW only if the TE polarization is matched (figure 3.3a). By placing the emitter with its dipole moment oriented orthogonal to the sheet, the Poynting vector lies in-plane and the BSW propagates along the truncation interface, as reported in figure 3.3a. Conversely, the emitter does not couple to the BSW if it is oriented perpendicularly to the surface, as in figure 3.3b.

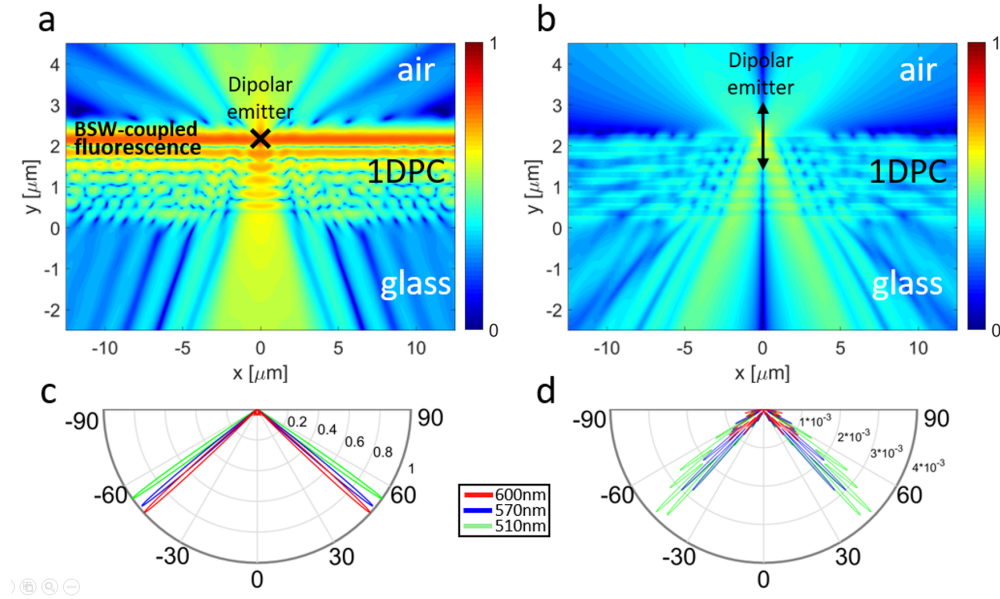


Figure 3.3: Calculated near-field distribution of the electric field intensity radiated by an emitter modeled with a dipole. The maps have been apodized in order to get rid of the diverging dipole sources. The dipole axis is **a)** parallel or **b)** normal to the surface plane, showing no coupling to TE BSW in **b)**. **c)**, **d)** Calculated far-field radiation pattern corresponding to the near-field distribution in **a)** and **b)** for different radiated wavelengths. The radiation pattern shows the dispersive behaviour of the BSW-coupled fluorescence and the highly directional emission in **c)**.

According to the momentum conservation law, the leakage radiation propagates into the substrate at a specific angle determined by the BSW dispersion relation according to the following relation:

$$k_{BSW} = k_0 n_{glass} \sin(\theta_{BSW}) \quad (3.5)$$

where k_{BSW} is the BSW wavevector, k_0 is the free-space wavevector, n_{glass} is the substrate refractive index (in our case $n_{glass} = 1.51$) and θ_{BSW} is the leaking angle.

In figure 3.3c and 3.3d are reported three far field patterns at different wavelengths, where a change in the output angle is observable.

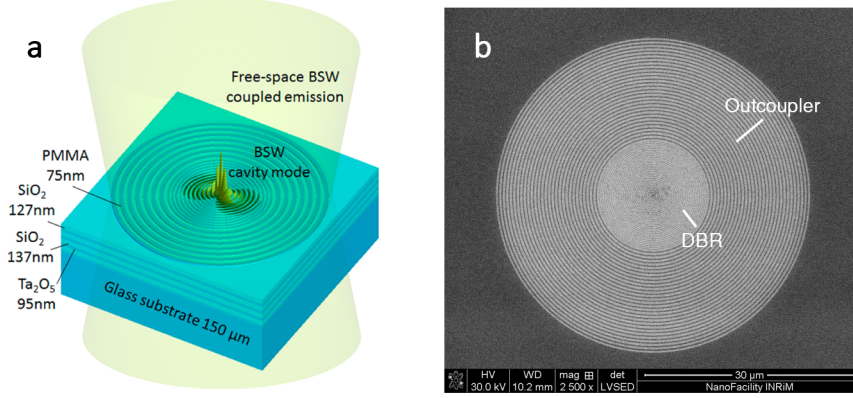


Figure 3.4: **a)** Sketch of the device showing the dielectric multilayer topped by a patterned dye-doped PMMA layer. The circular cavity and the grating outcoupler are etched in the PMMA layer. **b)** Scanning electron microscope image showing the top layer of the multilayer, patterned with the circular DBR and the grating outcoupler using electron beam lithography. Adapted from [97]

3.4 Bloch surface waves circular cavity

A schematic of the original device analyzed is illustrated in figure 3.4a. The 1DPC is patterned with concentric rings. The pattern includes an inner region associated with a circular cavity and an outer region corresponding to a circular grating outcoupler. The cavity is constituted by a central spacer surrounded by periodic corrugations acting as a distributed Bragg reflector (DBR) for BSWs in a specific spectral range. An organic dye, Atto-532 (fluorescence range from 530 to 650 nm, peaked at $\lambda_{ATTO} = 570$ nm), is dissolved in PMMA before spinning, at a concentration of 0.01 mg mL^{-1} . Cavity and outcoupler structures are fabricated by electron beam lithography.

In the framework of two-dimensional optics [143], this structure represents an example of a circular Fabry-Pérot cavity for BSW [144], additionally provided with an external diffractive light outcoupler (figure 3.3b). The organic dyes embedded within the PMMA spacer volume are excited by a tightly focused pulsed laser beam. A portion of the emitted fluorescence couples to the BSW cavity mode, depending on the randomly distributed orientations and positions of the dye molecules in PMMA [136]. The cavity is circular in order to maximize the likelihood of the emitters to couple to the BSW cavity mode, which has an in-plane electric field

associated thereto. Since the DBR has a finite number of periods, such a BSW-coupled fluorescence can tunnel through the DBR annular region, thus reaching the outcoupler and being diffracted out-of-plane in both air and glass. The outcoupler period is designed to diffract BSW-coupled fluorescence at the zeroth order, along a direction perpendicular to the sample surface.

3.4.1 Numerical model

2D

Similarly to surface plasmon polaritons [127], periodic surface reliefs can operate as DBRs for BSW, thus, opening frequency gaps in the dispersion curve, wherein the mode propagation is forbidden [36]. We set up a 2D computational model of the silica-tantalia 1DPC terminated with a binary DBR inscribed in the 75 nm thick PMMA layer (Figure 3.5a). Numerical modeling is performed using the FDTD method in Lumerical Inc. software. First, a two-dimensional slice of the structure is used to compute the BSW modes supported by the 1DPC (topped with the PMMA layer). Next, BSW modes at specific wavelengths and effective refractive index are selected for injection into the simulation region, directed toward the corrugation acting as a distributed Bragg reflector. The reflected power is collected by a frequency-domain field and power monitor. Depending on the grating period, BSWs can be partially transmitted or reflected. At each wavelength, the normalized power delivered by back-reflected BSWs is collected and used to calculate the spectrally resolved reflectivity map shown in Figure 3.5a. The spectral width of the stop-band is generally determined by the effective refractive index contrast Δn_{eff} introduced by the DBR. At $\lambda_0 = 570$ nm, a n_{eff} between 1.02 and 1.15, modulated with a spatial period $\Lambda_{DBR} = 260$ nm produces a 30 nm wide stop-band in the wavelength range from 550 to 580 nm (Figure 3.5b). The stop band is designed to be roughly centered about the emission spectrum of the dye embedded in PMMA. According to the 2D model, the inner spacer can be sized such that one or more BSW cavity modes are allowed (Figure 3.5c). For diameters D ranging from 540 to 580 nm, the BSW cavity is single-mode, the mode spectral position being tunable within the DBR stop band. In an exemplary design with $D = 570$ nm and $\Lambda_{DBR} = 260$ nm, a cavity mode occurs at $\lambda_0 = 570$ nm, as shown by a reflectivity dip in the stop band reported in Figure 3.5d. Although simplified, this 2D approach is useful to set the cavity geometrical parameters. However, the calculation of the cavity Q -factor, the mode volume and the corresponding field distribution requires a more realistic 3D model.

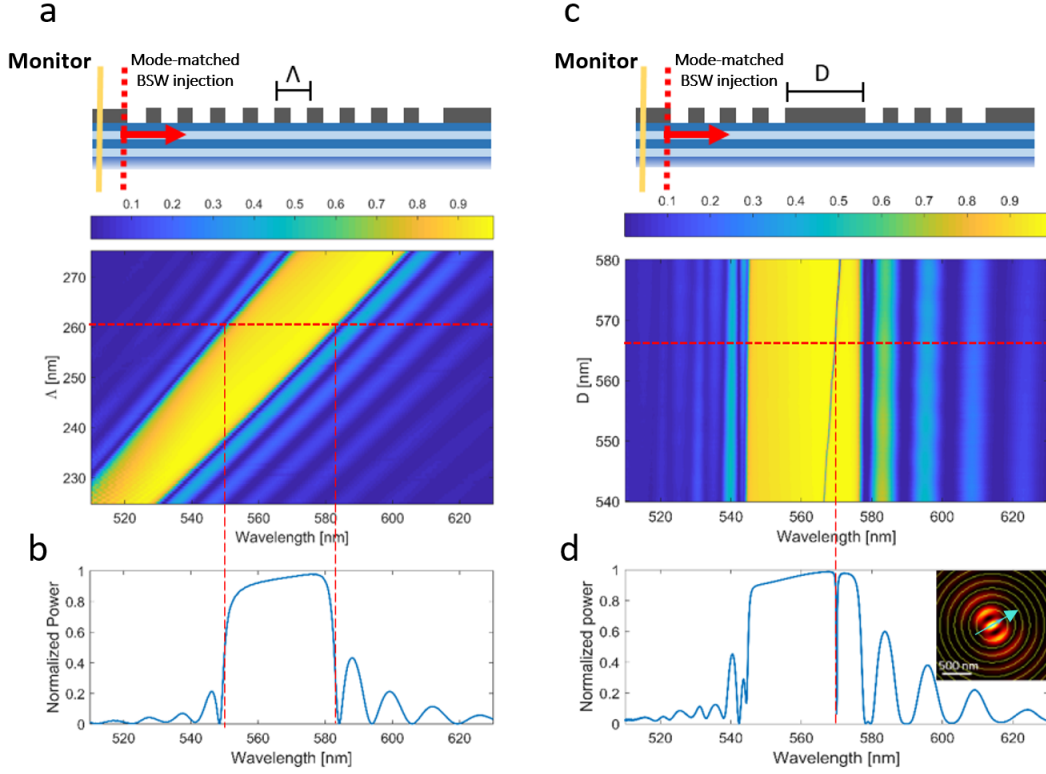


Figure 3.5: **a)** Sketch of the 2D model used to calculate the DBR period. A BSW mode is launched parallel to the multilayer surface, toward a grating inscribed in the PMMA film. The reflected power is collected by a monitor, located behind the BSW injection position. A dispersed, high reflectivity spectral band appears for different corrugation periods. **b)** BSW reflectivity spectrum resulting from a grating period $\Lambda_{DBR} = 260$ nm. The stop band is about 30 nm wide. **c)** Sketch of the two-dimensional model used to calculate the cavity spacer diameter. A weakly dispersed cavity mode appears for different spacer diameters. **d)** Exemplary cavity spectrum at $\lambda_0 = 570$ nm resulting from a spacer diameter $D = 570$ nm. The cavity mode appears as a narrow reflectivity dip within the stop band. Inset: Intensity distribution $|E(x, y)|^2$ referred to the electromagnetic field emitted at λ_0 by a single dipole located in the cavity spacer, embedded 35 nm beneath the PMMA top surface. The dipole momentum is oriented as indicated by the cyan arrow. Reproduced from [97].

3D

Q -factor and Purcell factor are calculated based on a 3D model of the cavity, wherein single dipolar emitters are positioned within the cavity spacer. As the dipole-cavity coupling strength depends on the position and orientation of the dipole momentum with respect to the cavity geometry, the most favorable configuration has been considered, that is, emitters are always located in the spacer center, 35 nm beneath the surface, with the dipole momentum oriented parallel to the surface, thus maximizing the mode coupling to TE-polarized BSWs. For each emission wavelength, the corresponding nearfield distribution $|E(x, y)|^2$ is calculated over a plane 10 nm above the PMMA surface (Figure 3.5d, inset) and integrated. Furthermore, the Q factor is estimated as $\lambda_0/\Delta\lambda$ from the cavity near-field spectrum obtained by Fourier-transforming the time-varying values of the electromagnetic field as sampled in multiple locations (randomly distributed) within the spacer.

The Q factor is found to be $Q = \lambda_0/\Delta\lambda \approx 1440$ for a cavity configuration having 30 DBR periods ($\Lambda_{DBR} = 260$ nm) and spacer diameters D ranging from 550 to 570 nm. The Purcell factor is calculated as the power flow ratio from the emitter in the cavity and in a homogeneous medium (PMMA). The power flow is calculated by monitoring the energy dissipation rate of the emitter. In order to do this, the simulation time window needs to be set large enough to guarantee a complete decay of the radiated electromagnetic energy, with a negligible residual energy within the simulation domain. To cross-check the reliability of the numerical results, the Purcell factor is also calculated by using the quality factor Q and the mode volume V of the cavity at the resonance wavelength λ_{cavity} into 3.4, as will be discussed later in this chapter. The cavity mode volume is obtained by performing numerically the integral in $V = \int \epsilon(\mathbf{r})|E(\mathbf{r})|^2 dV / \text{Max}\{\epsilon(\mathbf{r})|E(\mathbf{r})|^2\}$.

3.5 Time-resolved spectroscopic setup

The measurement apparatus can perform a spectral and temporal measurement of light emitted from the sample surface, with spatial and angular resolution. In Figure 3.6a, a sketch of the setup is presented. The illumination is provided by means of an upper stage mounting a NA = 0.95 objective (Olympus MPlan Apo 100 \times) working in air and the collection is performed by a NA = 1.49 oil immersion objective (Nikon APO TIRF 100 \times). The illumination objective focuses a circularly polarized $\lambda = 505$ nm pulsed laser onto the sample (15 ps pulses, 80 MHz repetition rate obtained by means of a Spectra Physics Tsunami Ti:Sa system in combination with an Inspire Blue harmonic generator), which is positioned on a 3-axis piezo stage (Physik Instrument). When measuring the decay rate of emitters coupled to the cavity mode, the excitation laser is accurately focused onto the spacer only, in order to minimize uncoupled emission radiated from other locations. Emitted fluorescence is collected by the oil immersion objective and then spectrally filtered (550 Long

pass, Thorlabs) in order to block the laser radiation. A three-lens telescope system produces two intermediate image planes wherein spatial masks (e.g., a diaphragm or a beam blocker) can be inserted. The sample direct plane is then imaged either onto a CMOS camera (Thorlabs HR-CMOS DCC3260M) or on the entrance slit of a spectrometer (Acton SpectraPro 300, Princeton Instruments), thanks to a tiltable mirror. Only fluorescence emission coming from specific spatial regions defined according to the spatial masks can be then spectrally and temporally analyzed by the streak camera system (Hamamatsu). Spectroscopic measurements related to direct plane imaging mode are performed with a 600 lines/mm grating, leading to a spectral resolution down to 0.18 nm. In BFP imaging mode, the grating is changed to a 150 lines/mm, in order to increase the level of the detected signal, although at the expense of the spectral resolution. The time range of the streak camera is 2 ns, which is large enough to measure the uncoupled background Atto 532 lifetime. In front of the telescope system, a flipping lens performing Fourier transformation is used to produce a BFP image of the collection objective onto the CMOS camera and the spectrometer entrance slit. By selecting specific portions of the BFP image, light propagating within corresponding angular ranges is spectrally and temporally analyzed.

3.6 Experimental results

3.6.1 Spectral signature of BSW-coupled emission

Experimentally, dye molecules dispersed within the PMMA spacer are excited by a $\lambda = 505$ nm pulsed laser beam. When the whole cavity is illuminated with a broad laser spot, a fluorescence image as shown in Figure 3.7a is observed. All excited dipoles radiate either in the free space or coupled to BSWs, according to the local density of states (LDOS) available at their specific locations. As the BSW-coupled radiation propagates along the structure surface, it gets weakly scattered by the structure reliefs. The combination of the direct free-space emission and the BSW-coupled radiation scattering results in a broad fluorescence distribution that appears spatially homogeneous over the illuminated area. Part of the BSW-coupled fluorescence from dipoles spread all over the illuminated structure resonates within the cavity and gets scattered at the spacer, as indicated by the bright spot located at the cavity center. Unfortunately, this fluorescence spot includes a large amount of radiation emitted by dipoles excited out of the spacer, which are insensitive to the cavity mode LDOS. In order to reduce the emission from dipoles out of the spacer, the laser excitation needs to be tightly focused in the cavity center (Figure 3.7b). After a proper spatial filtering by means of a diaphragm, as illustrated in the previous Section, the image of the very cavity center can be then collected for the spectral and temporal analysis.

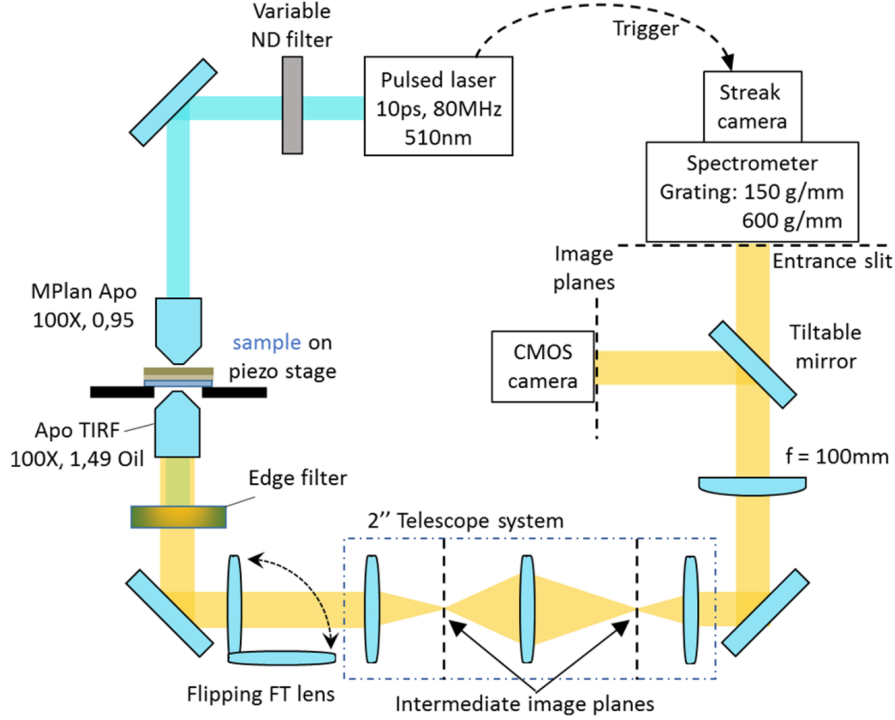


Figure 3.6: Optical setup for time-resolved spectral measurements with space/angular resolution capabilities. A flipping lens allows the imaging system to switch from a BFP image or a direct-plane image detection. By properly employing masking elements (e.g., diaphragms or beam-blockers) on the two intermediate image planes, specific portions of either the direct-plane or the BFP images can be selectively projected on the spectrometer entrance slit. Reproduced from [97].

The spectroscopic signature of a typical BSW cavity-coupled emission reveals a two-peak profile, as shown in Figure 3.7c. The two peaks are separated by roughly 1 nm and are well fitted by a pair of Lorentzian profiles centered at $\lambda_1 = 564.3$ nm and $\lambda_2 = 565.1$ nm, with FWHM $\Delta\lambda_1 = 0.6$ nm and $\Delta\lambda_2 = 0.4$ nm, respectively. We account these two peaks to a slight deviation of the cavity from a perfectly circular shape. An elliptical spacer would lead to the appearance of two distinct modes associated with the orthogonal directions parallel the ellipse major and the minor axis. As illustrated in Figure 3.5c, a variation of the spacer width as small as 10 nm results in a corresponding spectral shift of the mode resonance by about 1.3 nm. This effect is found for all the considered samples. Corresponding estimations for the cavity quality factor result in $Q_1 = 940$ and $Q_2 = 1413$.

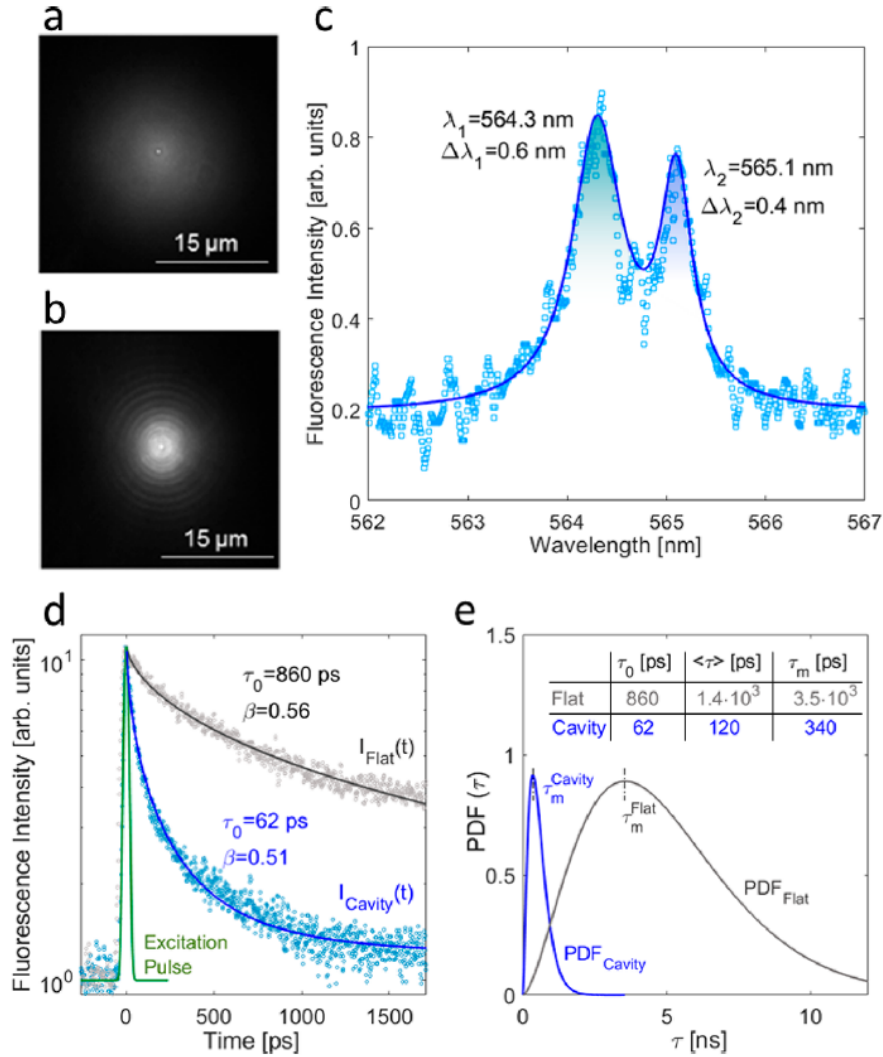


Figure 3.7: **a)** Fluorescence image of a BSW cavity (with no outcoupler) illuminated by a wide laser spot. **b)** Same cavity illuminated by a laser beam focused on the spacer. Fluorescence surrounding the central bright spot is associated with BSW cavity-coupled emission that is radially propagating and scattered by the DBR corrugations. **c)** Emission spectrum collected from direct-plane imaging of the cavity center. **d)** Time-resolved decay of BSW cavity mode-coupled emission $I_{cavity}(t)$ (blue circles) and free-space emission from a flat 1DPC region $I_{flat}(t)$ (grey circles). Solid lines relate to corresponding stretched exponential fitting functions. The theoretical excitation pulse is represented as a Gaussian pulse with a 15 ps temporal width. **e)** Probability density distributions of time constants $PDF_{cavity}(\tau)$ (blue line) and $PDF_{flat}(\tau)$ (grey line) associated with the stretched exponential fits in **d)**. Reproduced from [97].

3.6.2 Temporal signature of BSW-coupled emission

A time-resolved decay of the BSW cavity-coupled emission $I_{cavity}(t)$ can be obtained upon integration of the detected fluorescence over the spectral region including the resonance peaks. For comparison purposes, the fluorescence intensity $I_{flat}(t)$ collected from a homogeneous, flat region (aside from the cavity structure) is also considered. As commonly acknowledged, a single exponential function is unsuitable to fit the observed temporal signals, because fluorescence results from multiple independent emitters, which are possibly cavity coupled with different strengths and corresponding decay rates, depending on continuous variations of relative positions and orientations. In these circumstances, a stretched exponential (Kohlrausch) function is usually employed [113, 119, 145], which is also suitable in case the emitters are embedded within soft matrices or bound to dielectric surfaces [146]. For the fitting operation, we employ a normalized time-varying stretched exponential function, written as:

$$I(t) = \exp \left[- \left(\frac{t}{\tau_0} \right)^\beta \right] = \int_0^\infty P_\beta(s) \exp \left[- \left(s \frac{t}{\tau_0} \right) \right] ds \quad (3.6)$$

where $P_\beta(s)$ is a parametric probability density function (PDF) for the normalized decay rate $s = \tau_0/\tau$ [147], τ_0 is a characteristic time constant of the decay and $0 < \beta \leq 1$ is the stretch factor [146]. The PDF is given by

$$P_\beta(s) = \frac{1}{\pi} \sum_{n=1}^{\infty} \frac{(-1)^{n+1} \Gamma(n\beta + 1)}{n! s^{n\beta+1}} \sin(\pi n\beta) \quad (3.7)$$

such that $\int_0^\infty P_\beta(s) ds = 1$. From the experimental time-resolved intensities, a background level is estimated by averaging the detector counts collected ahead of the excitation pulse. The signal is then background-subtracted and normalized before the fitting procedure with the function $I(t)$ above. Experimental signals $I_{cavity}(t)$ and $I_{flat}(t)$, together with the associated fitting functions (added to the background level), are shown in Figure 3.7d in a semilogarithmic plot. As expected, the observed fluorescence signals depart significantly from single-exponential profiles and are well fitted by Kohlrausch functions with $\beta = 0.51 \pm 0.01$, $\tau_0 = 62 \pm 3$ ps for the BSW cavity-coupled emission and $\beta = 0.56 \pm 0.15$, $\tau_0 = 860 \pm 30$ ps for the emission from the flat area. The deviation of $I_{flat}(t)$ from a monoexponential profile can be due to local aggregation effects (also observed, for example, in clusters of quantum dots [129]), while $I_{cavity}(t)$ is strongly affected by the LDOS provided by the resonant structure. The two decay mechanisms experienced by dipole either within or outside the cavity lead to time constant distributions PDF_{cavity} and PDF_{flat} shown in Figure 3.7e. PDFs are calculated from the β and τ_0 parameters from the fitting procedure. Far from the cavity, where no coupling effects to the resonant structure take place, fluorescence is emitted according to a continuous distribution of lifetimes τ spanning over a range of more than 10 ps and peaked on

a highest-probability value $\tau_m^{flat} = 3.5$ ns. An average lifetime for the uncoupled emission can be calculated as $\langle \tau^{flat} \rangle = \int_0^\infty \tau P_{\beta=0.56}(s) ds = 1.4$ ns. On the other hand, the transient fluorescence from dipoles in the cavity is observed to occur on shorter time scales than outside. The PDF_{cavity} distribution is well separated from PDF_{flat}, with the highest-probability lifetime $\tau_m^{cavity} = 340$ ps and an average time constant $\langle \tau^{cavity} \rangle = \int_0^\infty \tau P_{\beta=0.51}(s) ds = 120$ ps. An average decay rate enhancement by 1 order of magnitude is obtained by considering the ratio $\langle \tau^{flat} \rangle / \langle \tau^{cavity} \rangle \cong 12$. However, this value underestimates the maximum lifetime decrease experienced by emitters whose orientation and spatial position accomplish a full coupling to the BSW cavity mode.

In order to gather more insights on the observed enhanced decay rate, we propose an alternative fitting model based on a two-exponential function

$$I(t) = A_{fast} \cdot \exp\left[-\frac{t}{\tau_{fast}}\right] + A_{slow} \cdot \exp\left[-\frac{t}{\tau_{slow}}\right] \quad (3.8)$$

which substantially assumes the total signal intensity as steadily given by two independent terms with constant amplitude over time. Fluorescence from the cavity has a fast component with a time constant $\tau_{fast} = 45 \pm 2$ ps, and a slow component with $\tau_{slow} = 366 \pm 10$ ps. The fast component here is dominant over the slow component, the relative contributions being given by the normalized amplitudes $A_{fast}^{(N)} = A_{fast} / (A_{fast} + A_{slow}) = 0.71$ and $A_{slow}^{(N)} = A_{slow} / (A_{fast} + A_{slow}) = 0.29$, respectively. A weighted sum of the fast and slow lifetimes results in $A_{fast}^{(N)} \tau_{fast} + A_{slow}^{(N)} \tau_{slow} = 138$ ps, which is close to the average time constant $\langle \tau_{cavity} \rangle = 120$ ps previously calculated from the PDF_{cavity} distribution. According to this interpretation, a significant amount of the overall fluorescence is emitted within a very short time scale, thanks to the coupling to the cavity mode. By retaining this fast component only, an estimate of an improved decay rate enhancement for cavity-coupled dipoles can be calculated as $\langle \tau_{flat} \rangle / \tau_{fast} \cong 31$. The change of decay rate, quantified as the Purcell factor F_P (see section 3.1), is related to the Q factor and the modal volume of the resonance through the formula 3.4. Based on a FDTD 3D model (see section 3.3.1), the BSW cavity mode volume for a $Q = 1440$ cavity is $V = 2.23(\lambda/n)^3$. This leads to a factor $F_P = 49$, which represents the maximum expected decay rate enhancement for fully coupled dipoles. The observed decay rate enhancement $\langle \tau_{flat} \rangle / \tau_{fast} \cong 31$ is consistent with a Purcell factor $F_P = 32$ calculated for the lowest-quality cavity mode ($Q_1 = 840$), assuming a mode volume as previously shown.

3.7 Directional BSW cavity-coupled emission in free-space

Generally speaking, the BSW-coupled radiation occurs according to a well-defined dispersion curve, as we have seen in section 3.2. Upon application of the Bragg law, suitable diffraction gratings can be designed such that the BSW-coupled radiation in given spectral ranges is diffracted along specific directions [142, 148]. In the following, we consider cavities having the BSW resonant mode peaked at $\lambda_0 = 560$ nm, surrounded by a circular diffractive element. A sketch of this structure is reported in figure 3.8. In order to diffract BSW-coupled radiation at λ_0 normally to the multilayer surface, a circular grating outcoupler having period $\Lambda_{outcoupler} = 520$ nm is introduced.

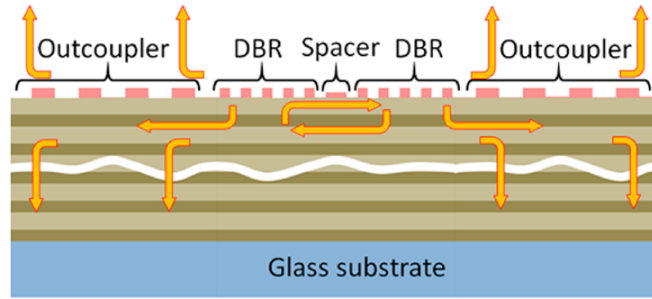


Figure 3.8: Working principle of the device showing the mechanism of emission coupling to the BSW cavity mode and corresponding diffraction by means of the outcoupler. Adapted from [97].

3.7.1 Numerical model

FDTD calculations are performed on a complete 3D model (including cavity and outcoupler). The source is represented by a single oscillating electric dipole buried in the center of the cavity spacer, with the dipole momentum lying parallel to the surface. Emission wavelength is $\lambda_0 = 560$ nm, thus, matching the cavity mode. By far-field projecting the calculated near-field energy distribution around the structure, the angularly resolved radiated power in the top and bottom half-spaces (air and glass, respectively) can be obtained. Angularly resolved radiation patterns are calculated by projecting near-field power values collected by monitors surrounding the cavity and the outcouplers. Once the radiation intensity $|E(\theta, \phi)|^2$ is obtained, an integration in spherical coordinates is performed over proper angular integration intervals according to $\iint |E(\theta, \phi)|^2 \sin(\theta) d\theta d\phi$, leading to the emitted power values in the surrounding media. A normalization to the overall power emitted in a 4π solid angle is also performed. In Figure 3.9a,b, the integrated emitted power in air

and glass within a $NA = 0.09$ about the multilayer normal is plotted as a function of the number of outcoupler corrugation periods. Upon a comparison with two reference cases represented by a dipole within a flat 75 nm thick PMMA slab on the multilayer and a dipole at a glass-air interface, we found that the presence of the outer grating greatly enhances the directionality of the emitted radiation from the dipole coupled to the BSW cavity mode, provided the momentum-matching according to the Bragg's law. Extraction performances increase with an increasing number of periods considered. As an example, for 30 outcoupler periods, the power collected within $NA = 0.09$ in air is enhanced up to 26 and 62 times with respect to the dipole on a bare glass-air interface and on the flat multilayer, respectively. Similarly, in the glass medium, the diffracted BSW cavity-coupled power is 20 and 36 times larger as compared to the glass-air and the flat multilayer cases. These enhancement factors are merely due to an energy angular redistribution and are not taking into account the Purcell factors previously discussed, as normalized powers are here concerned.

3.7.2 Angular distribution with back focal plane technique

In order to appreciate the angular distribution of the emitted power, radiative patterns are calculated in the glass substrate for emitters in PMMA-topped flat 1DPC area and within the BSW cavity. In these calculations, multiple emitters are included, having random 3D orientations and emitting at $\lambda_0 = 560$ nm. Dipoles located over a flat 1DPC area radiate in free space, with some coupling to TE- or TM-polarized leaky modes sustained by the multilayer (sometimes called “internal” modes [149]). As a result, multiple rings beyond the critical angle are observed, as shown in Figure 3.9c. On the contrary, BSW coupled fluorescence is hampered to leak into the glass substrate because of the large number of the structure layers.

Experimental observations performed by means of BFP imaging are in good agreement with the calculated pattern (Figure 3.9d). When the dipoles located in the cavity spacer are considered, a significant amount of power is beamed at emission angles close to the 1DPC surface normal (Figure 3.9e). This is expected, as the BSW cavity-coupled emission produced inside the cavity can tunnel through the surface DBR corrugations and are then diffracted by the surrounding outcoupler. Experimentally, a similar BFP image is observed, as shown in Figure 3.9f, wherein the normally diffracted radiation intensity almost saturates the camera. The divergence of such a diffracted BSW cavity mode-coupled fluorescence is well below $NA = 0.09$, as indicated in the figure.

3.7.3 BFP spectral and temporal analysis

The BFP image can be spatially filtered by means of a diaphragm and then directed to the spectrometer entrance slit. In this way, only fluorescence diffracted

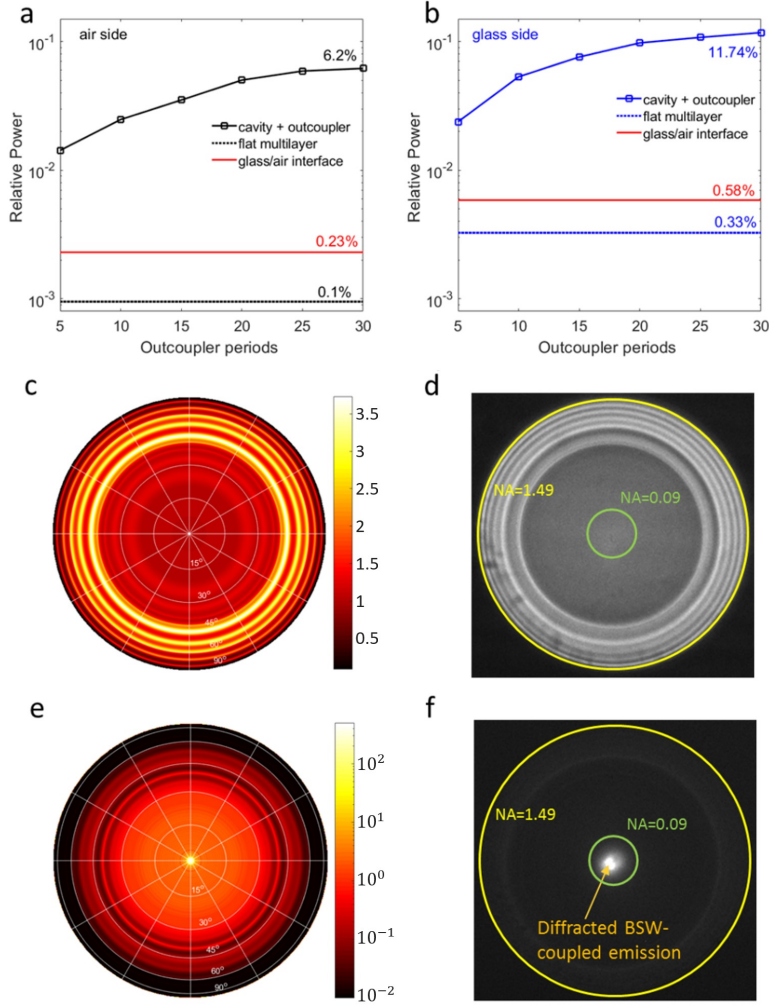


Figure 3.9: Calculated BSW cavity-coupled emission power from a single dipole located in the cavity spacer, diffracted within a $\text{NA} = 0.09$ about the multilayer normal in air **a**) and in glass **b**). For comparison purposes, single dipoles within a 75 nm thick PMMA layer on top of a 1DPC and on a bare glass-air interface are also considered. Power is normalized to the overall power emitted in a 4π solid angle. **c**) Calculated radiated intensity $|E(\theta, \phi)|^2$ in glass from multiple dipoles with 3D random orientations in a flat 75 nm thick PMMA layer on 1DPC. Color scale is linear. Emission wavelength is $\lambda = 560$ nm. **d**) Back focal plane image of fluorescence collected from a flat region of the PMMA-topped 1DPC by means of a $\text{NA} = 1.49$ oil immersion objective. **e**) Calculated radiated intensity $|E(\theta, \phi)|^2$ in glass from multiple dipoles with random 3D orientations in the cavity spacer center. Color scale is logarithmic to avoid color saturation at $\theta = 0^\circ$. Emission wavelength is $\lambda = 560$ nm. **f**) Back focal plane image of fluorescence collected from cavity and outcoupler, wherein the cavity spacer only is illuminated by a tightly focused laser beam. Reproduced from [97].

at small angles about the optical axis is collected. The spectrometer slit aperture had to be kept as large as 200 μm and a 150 lines/mm grating is used in order to gather a signal high enough on the detector, at the expense of the spectral resolution attainable. As expected from design, a strong evidence of a BSW cavity-coupled fluorescence is observed (Figure 3.10a). A closer analysis reveals that the peak can be well-fitted by a pair of Lorentzian functions, spectrally separated by 1.4 nm, as a spectral signature of the BSW cavity-coupled emission. A higher background intensity is also observed. The peak centered at $\lambda \approx 570$ nm is likely to be associated to the band edge mode relative to the DBR.

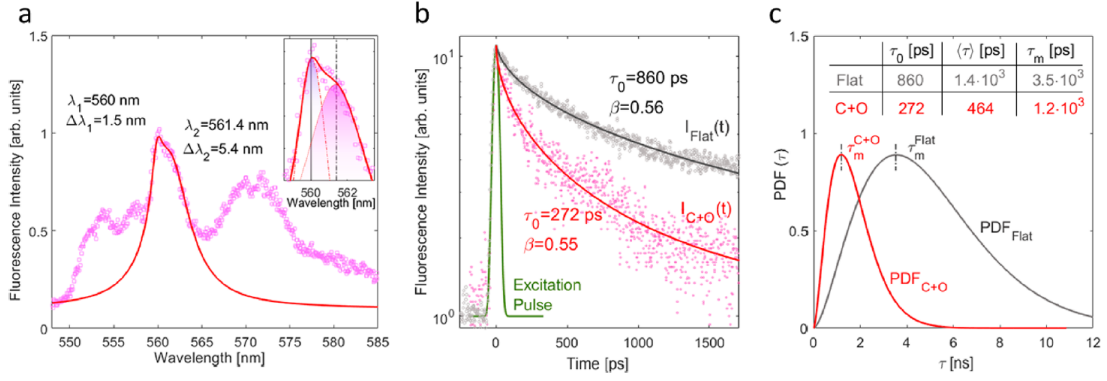


Figure 3.10: **a)** Diffracted fluorescence spectrum collected at the central region of the BFP. The BSW cavity-coupled emission is well-fitted by a pair of Lorentzian functions. **b)** Time-resolved decay of fluorescence collected from the central region of the BFP for cavity and outcoupler, $I_{c+o}(t)$ (pink circles) and for a flat 1DPC region, $I_{flat}(t)$ (grey circles). Solid lines refer to stretched exponential functions used for fitting. **c)** Probability density distributions of time constants $\text{PDF}_{c+o}(\tau)$ (red line) and $\text{PDF}_{flat}(\tau)$ (grey line) associated with the stretched exponential fits in **b)**. Average time constant $\langle \tau \rangle$ and most probable time constant τ_m are summarized in the inset. Adapted from [97].

As temporal traces are concerned, fluorescence diffracted from a cavity + out-coupler system, $I_{c+o}(t)$, is observed to decay faster than the fluorescence from a flat area (Figure 3.10b), as a result of the cavity coupling. In analogy to the previous analysis, a stretched exponential function is used for data fitting, resulting in a characteristic time constant $\tau_0 = 272 \pm 25$ ps and a stretch parameter $\beta = 0.55 \pm 0.03$. From the corresponding time constant distribution PDF_{c+o} presented in Figure 3.10c, a highest-probability lifetime $\tau_m^{(c+o)} = 1.2$ ns and an average lifetime $\langle \tau^{(c+o)} \rangle = \int_0^\infty \tau P_{\beta=0.55}(s) ds = 464$ ps are also obtained. Moreover, when fitting with a two-exponential function, a fast and a slow components are found, with time constants and normalized amplitudes $\tau_{fast} = 95 \pm 13$ ps, $A_{fast}^{(N)} = 0.48$, and $\tau_{slow} = 810 \pm 45$ ps, $A_{slow}^{(N)} = 0.52$, respectively. Differently from the cavity-only

case considered above (Figure 3.7), the far-field fluorescence signal diffracted by the outcoupler has a more important contribution associated with the slow component. This result suggests that the higher background level observed in the spectrum of Figure 3.10a is related to the emission from uncoupled (slowly decaying) molecules, which are laser-excited, despite the spatial mismatch with respect to the cavity. This limiting aspect is due to the dispersed distribution of dye on the photonic surface. Taking into consideration the fast component only, an increase of the fluorescence lifetime $\langle\tau_{flat}\rangle/\tau_{fast} \cong 15$.

Overall, the combination of the enhanced decay rate and the angular redistribution of free-space radiation is estimated to provide a final increase of the power emitted within a $NA = 0.09$ and a spectral range $\Delta\lambda \approx 1$ nm (in illumination saturation condition) by roughly 2 orders of magnitude.

3.8 Conclusions

In this chapter we have analyzed a novel photonic structure, constituted by a dielectric multilayer patterned with an annular structure having an inner circular cavity and an outer diffraction grating. The overall structure supports a localized BSW resonant mode within the cavity and dispersed propagating BSW modes outside. Thanks to the availability of BSW modes, we managed to increase the decay rate of fluorescent emitters located in the cavity center and to diffract the corresponding coupled emission in free space with high control. The evidence of a fast decaying BSW cavity-coupled emission within $NA = 0.09$ in the far field demonstrate the effectiveness of the mechanism proposed. It is observed, however, that the diffracted fluorescence contains a higher contribution from uncoupled radiation, thus, resulting in a correspondingly larger time constant with respect to fluorescence directly imaged from the cavity center. We account for this background as due to the overall fluorescent PMMA structure on top of the multilayer. In fact, despite the laser illumination being tightly focused, dye molecules spread all over the cavity are unavoidably excited and (at least, partially) coupled to propagating BSW that are then diffracted in free space. Stated otherwise, it is highly likely that BSW-coupled emission excited elsewhere outside the cavity spacer contribute to the far-field intensity detected along the optical axis because of diffraction. This effect is expected to disappear in case localized sources such as single quantum dots, diamond crystals or precisely defected 2D flakes are employed [150, 151]. With this respect, our approach offers an advantage for emitters to be deposited and possibly manipulated directly on the structure surface, thus, reducing fabrication efforts for source(s) integration.

Chapter 4

Vortex beam generation by spin-orbit coupling in Bloch surface waves

Axis-symmetric grooves milled in metallic slabs have been demonstrated to promote the transfer of orbital angular momentum (OAM) from far- to near-field and vice versa, thanks to spin-orbit coupling effects involving surface plasmons (SP). However, the high absorption losses and the polarization constraints, which are intrinsic in plasmonic structures, limit their effectiveness for applications in the visible spectrum, particularly if emitters located in close proximity to the metallic surface are concerned. In this chapter, an alternative mechanism for vortex beam generation is presented, wherein a free-space radiation possessing OAM is obtained by diffraction of Bloch surface waves (BSWs) on a dielectric multilayer. A circularly-polarized laser beam is tightly focused on the multilayer backside by means of an immersion optics, such that TE-polarized BSWs are launched radially from the focused spot. While propagating on the multilayer surface, BSWs exhibit a spiral-like wavefront due to the polarization-selective coupling mechanism. A spiral grating surrounding the illumination area provides for the BSW diffraction out-of-plane, by imparting an additional azimuthal geometric phase distribution defined by the topological charge of the spiral structure. At infinite, the constructive interference results into free-space beams with defined combinations of polarization and OAM satisfying the conservation of the total angular momentum, based on the incident polarization handedness and the spiral grating topological charge. As an extension of this concept, chiral diffractive structures for BSWs can be used in combination with surface cavities hosting light sources therein.

4.1 Angular momenta of light

4.1.1 Spin angular momentum and polarization structure of light

An electromagnetic wave is specified by its frequency and direction of propagation as well as by the direction of oscillation of the field vector, i.e. the polarization state of the electromagnetic wave. By virtue of the transverse nature of electromagnetic wave, the variation of the electric field vector is confined in a plane perpendicular to the direction of propagation. For a monochromatic plane wave propagating in the z direction, the electric field vector is given by:

$$\mathbf{E}(z, t) = \mathbf{E}_0 e^{i(\omega t - kz)} \quad (4.1)$$

where k is the wave vector in the direction of z and \mathbf{E}_0 is the complex polarization vector that lies in the xy plane. The end point of the electric field vector \mathbf{E} describes a curve at a typical point in space, which is the time evolution of the components (E_x, E_y) :

$$E_x = E_{0x} \cos(\omega t - kz + \delta_x), \quad E_y = E_{0y} \cos(\omega t - kz + \delta_y) \quad (4.2)$$

where the complex polarization vector \mathbf{E}_0 has been defined as $\mathbf{E}_0 = \mathbf{x}E_{0x}e^{i\delta_x} + \mathbf{y}E_{0y}e^{i\delta_y}$, with E_{0x} and E_{0y} positive numbers and \mathbf{x} and \mathbf{y} unit vectors.

It is convenient to express the polarization vector \mathbf{E}_0 in the form of Jones vector, which describes efficiently the polarization state of a plane wave:

$$\mathbf{J} = \begin{pmatrix} E_{0x}e^{i\delta_x} \\ E_{0y}e^{i\delta_y} \end{pmatrix} \quad (4.3)$$

The Jones vector contains complete information about the amplitudes and the phase of the electric field vector components. The normalized Jones vectors for the right- and left-hand circularly polarized light waves are given by:

$$\begin{aligned} \mathbf{R} &= \frac{1}{\sqrt{2}} \begin{pmatrix} 1 \\ -i \end{pmatrix} \\ \mathbf{L} &= \frac{1}{\sqrt{2}} \begin{pmatrix} 1 \\ i \end{pmatrix} \end{aligned} \quad (4.4)$$

These two circular polarizations are mutually orthogonal $\mathbf{R}^* \cdot \mathbf{L} = 0$ and can be used as a basis for any polarization states, which can be represented as a superposition of \mathbf{R} and \mathbf{L} .

Circularly polarized light carries an intrinsic spin angular momentum (SAM) of $\pm\hbar$ per photon, as deduced by Poynting in the early 1900s [152]. This finds confirmation in the photon picture of absorption and emission of light from atomic systems, where the angular momentum is conserved between the interacting optical field and the electronic state.

By properly combining the Eqs. 4.2, it is possible to find the curve described by the tip of the electric vector in the xy plane as time evolves [13]:

$$\left(\frac{E_x}{E_{0x}}\right)^2 + \left(\frac{E_y}{E_{0y}}\right)^2 - 2\frac{\cos\delta}{E_{0x}E_{0y}}E_xE_y = \sin^2\delta \quad (4.5)$$

where $\delta = \delta_y - \delta_x$. Eq. 4.5 is the equation of the polarization ellipse, represented in Figure 4.1a. A complete description of the polarization state of a light wave requires the orientation of the major axis of the ellipse with respect to the x axis, i.e. the *orientation angle* α , and the *ellipticity angle* ϵ , as indicated in Figure 4.1a. Right-handed circular (RHC), left-handed circular (LHC) and linear polarizations (LP) correspond to $\epsilon_{RHC} = \pi/4$, $\epsilon_{LHC} = -\pi/4$ and $\epsilon_{LP} = 0$ respectively. Linear polarization along x axis or y axis correspond to $\epsilon = 0 \wedge \alpha = 0$ and $\epsilon = 0 \wedge \alpha = \pi/2$, respectively. The parameters α and ϵ can be represented also on the Poincaré sphere, which is a unitary sphere with its cartesian coordinates (S_1, S_2, S_3) equals to the normalized Stokes parameters [153].

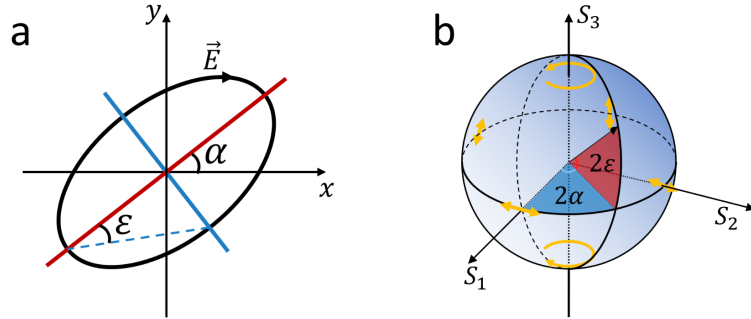


Figure 4.1: Schematic diagrams of **a** polarization ellipse and **b** Poincaré sphere. Note the north and south poles of the Poincaré sphere stand for RCP and LCP, respectively. On the equator of the Poincaré sphere, the corresponding polarization states are linear with the orientation varying with the azimuthal position.

4.1.2 Stokes parameters

In the previous section, the polarization description of a monochromatic plane wave is discussed. By virtue of its nature, a monochromatic plane wave must be

polarized. However, if the light is not absolutely monochromatic, the polarization state may be constantly changing. In this case, the light is said to be partially polarized, and to describe the polarization state of this type of radiation, the Stokes parameters are necessary:

$$\begin{aligned}
 S_0 &= \langle E_{0x}^2 + E_{0y}^2 \rangle, \\
 S_1 &= \langle E_{0x}^2 - E_{0y}^2 \rangle, \\
 S_2 &= 2\langle E_{0x}E_{0y} \cos \delta \rangle, \\
 S_3 &= 2\langle E_{0x}E_{0y} \sin \delta \rangle,
 \end{aligned} \tag{4.6}$$

where the amplitudes E_{0x} , E_{0y} and the relative phase δ are assumed to be time dependent. Some Stokes parameters of principal interest are given by:

- **Unpolarized light.** Since there is no preference between E_{0x} and E_{0y} , S_1 reduces to zero. The time average makes S_2 and S_3 also equal to zero. So the Stokes representation, for normalized field ($S_0 = 1$) is (1,0,0,0),
- **Linear horizontal polarization.** $E_{0y} = 0$, so the Stokes representation is (1,1,0,0),
- **Linear diagonal polarization.** In this case, $E_{0x} = E_{0y}$. If $\delta = 0$ it can be represented as (1,0,1,0), if $\delta = \pi$ (1,0,-1,0),
- **Right circular polarization.** $\delta = -\pi/2$, so it is represented by (1,0,0,-1).

Stokes polarimetry is used to completely characterize the polarization state of light, by using the four normalized Stokes parameters, which all have the dimension of intensity. Experimentally the Stokes parameters can be retrieved through six intensity measurements, by properly setting a quarter-wave plate and a linear polarizer on the optical axis [154] and projecting the light onto 3 different basis: H-V (horizontal-vertical), 45-135 (diagonal and anti-diagonal) and RHC-LHC (right- and left-handed circular). In this way, 6 intensity measurements are obtained, $I(H)$, $I(V)$, $I(45)$, $I(135)$, $I(RHC)$ and $I(LHC)$, each representing the projection of the light on a specific polarization channel. The 6 measurements can be combined to obtain the Stokes parameters:

$$\begin{aligned}
S_0 &= I(\text{H}) + I(\text{V}) \\
S_1 &= I(\text{H}) - I(\text{V}) \\
S_2 &= I(45) - I(135) \\
S_3 &= I(\text{RHC}) - I(\text{LHC})
\end{aligned} \tag{4.7}$$

Next, the polarization ellipse parameters α and ϵ can be retrieve using:

$$\begin{aligned}
\epsilon &= \frac{1}{2} \cdot \arg \left(\sqrt{S_1^2 + S_2^2} + iS_3 \right) \\
\alpha &= \frac{1}{2} \cdot \arg (S_1 + iS_2)
\end{aligned} \tag{4.8}$$

4.1.3 Orbital angular momentum

So far, the polarization characteristics of electromagnetic waves have been discussed and the SAM has been introduced. In addition to the SAM, there exist another type of angular momentum, namely the orbital angular momentum (OAM). The OAM is the component of angular momentum of a light beam that is dependent on the field spatial distribution, and not on the polarization. The existence of the OAM was suggested by Darwin in the 1930s [155] in the attempt to explain that quadrupole transitions in atomic systems necessitated an angular momentum exchange between light and atom corresponding to integer multiples of \hbar . By this he meant that the radiated photon must carry away not only spin but also OAM, and he gave expressions for each of these components [155]. Despite the work of Darwin and others, it was not until 1992 that Allen and co-workers [156] recognized that a light beam having helical phasefronts carried an orbital angular momentum distinct from, and additional to, the SAM of the photon. In particular, they derived that beams with l interwoven helical phasefronts carry an OAM of $l\hbar$ per photon. When such a light beam is represented by optical rays, these rays are skewed with respect to the beam direction.

4.2 Vortex beam

Figure 4.2 shows the phase structure and intensity property of light carrying OAM of various l values. When $l \neq 0$, the azimuthal phase term $e^{jl\phi}$ and the

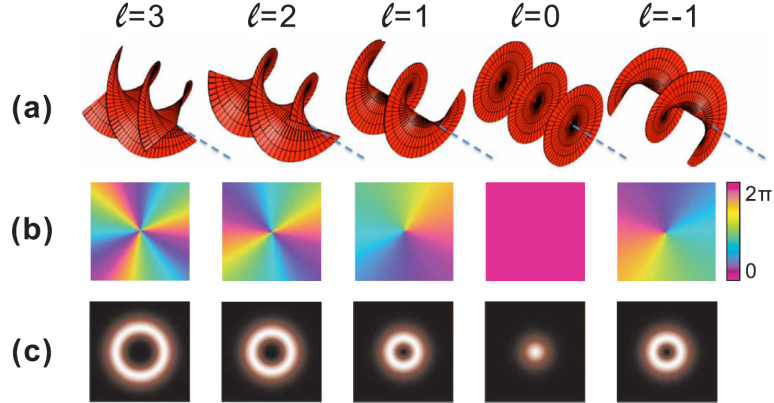


Figure 4.2: Phase and intensity properties of light beams with a vortex charge number $l = -1, 0, 1, 2, 3$ (from right to left): **a)** Schematic snapshots of the instantaneous phase. Helical phase fronts occurs when $l \neq 0$. The blue dash lines indicate the wave propagation. **b)** Phase profiles in a transverse plane [157]. **c)** Intensity distributions in a transverse plane. Annular intensity patterns can be seen when $l \neq 0$. Reproduced from [158]

common propagation phase term $e^{jk_z z}$, together, define an intertwined helical phase structure for OAM-carrying light (Fig. 4.2a). The topological number of this twist equals to $|l|$ while the twist handedness is defined by the sign of l . Due to its vortex-like feature, OAM-carrying light is well-known as "optical vortex" or "vortex beam". Vortex beams represent a family of structured beams generally characterized by a phase singularity along the optical axis, a doughnut intensity distribution and an azimuthally-varying phase over a beam transverse cross-section [159, 160]. Figure 4.2b shows the corresponding phase distributions in the transverse plane. We can see a phase dislocation or phase singularity at the center of the beams when $l \neq 0$. Such a phase singularity impart these beams an annular intensity profile as shown in Fig. 4.2c. The effective radii of these bright rings are also quantized, proportional to l [161].

The azimuthal phase item that defines the OAM is linked to the spatial variation of the light intensity and is independent of the polarization structure. Therefore, we can see that the optical SAM and OAM manifest the different degrees of freedom of light. When the polarization state is spatially inhomogeneous, the term vectorial vortex beams is often used [162].

In recent years, vortex beams have gained an increasing popularity because of several new applications into different domains such as micro-particle manipulation and trapping [163–165], compact laser sources [166, 167], microscopy [168, 169] and optical communications [170, 171]. Conventional methods for producing vortex beams [172] involve the use of (possibly tunable) anisotropic media such as liquid

crystal [173, 174] and q-plates [175] or hierarchically structured holograms encoding proper phase functions [176–179]. More recently, metasurfaces, which can be either dielectric or plasmonic, have been introduced in order to gather more degrees of freedom in OAM manipulation [180, 181], through the control of so-called spin-orbit coupling effects mediated by the metasurface topology [182]. Metasurfaces are mainly employed as free-space beam converters, which have found applications also within laser cavities [183]. The concept of beam conversion through metasurfaces relies on a spatially-dependent phase manipulation of the scattered field. The output vortex beams result from a coherent sum of the scattered radiation originating from different portions of the surface, which is illuminated as a whole. However, this approach can be hardly adopted when the input field has a limited spatial extension (as for focused beams or localized coherent sources such as optical antennas or cavities), unless some mode coupling is intervening [184]. This is indeed the case in structured metallic films, wherein the generation of free-space vortex beam carrying OAM occurs upon spin-orbit coupling and scattering/diffraction of plasmonic modes by means of nano-slits [185–187], properly arranged nano-apertures [188], possibly combined with circular diffraction gratings [189, 190]. Such results rely on the fact that OAM possessed by surface plasmons can be further manipulated and transferred to freely propagating radiation [187, 191].

In this chapter an alternative way of producing vortex beam is presented, by exploiting BSW, introduced in Section 1.3, as a mean to transfer energy, momentum and OAM to a free-space propagating beam. Such a two-step process involves a spin-orbit conversion from a focused circularly polarized beam into radially propagating BSWs and a BSW diffraction in free-space, with an additional geometric phase imparted by a chiral diffraction grating. Such a BSW-based approach can benefit from the multilayer low absorption that is potentially suitable for light source integration and an additional degree of freedom in the polarization state of coupled BSWs, which can be either TE- or TM-polarized depending on the multilayer design [192].

4.3 Spiral diffraction grating

4.3.1 The sample

The sample, sketched in Figure 4.3c, consists of a dielectric multilayer made of a stack of Ta₂O₅ (high refractive index) and SiO₂ (low refractive index) layers, deposited on a glass coverslip (150 μm thickness) by plasma ion-assisted deposition under high vacuum conditions (APS904 coating system, Leybold Optics). The stack sequence is substrate-[Ta₂O₅-SiO₂]_{x6}-Ta₂O₅-SiO₂-PMMA with 15 layers in total, including PMMA. The Ta₂O₅ layer (refractive index $n_{\text{Ta}_2\text{O}_5} = 2.08$) is 95 nm thick, the SiO₂ layer (refractive index $n_{\text{SiO}_2} = 1.46$) is 137 nm thick. The top SiO₂

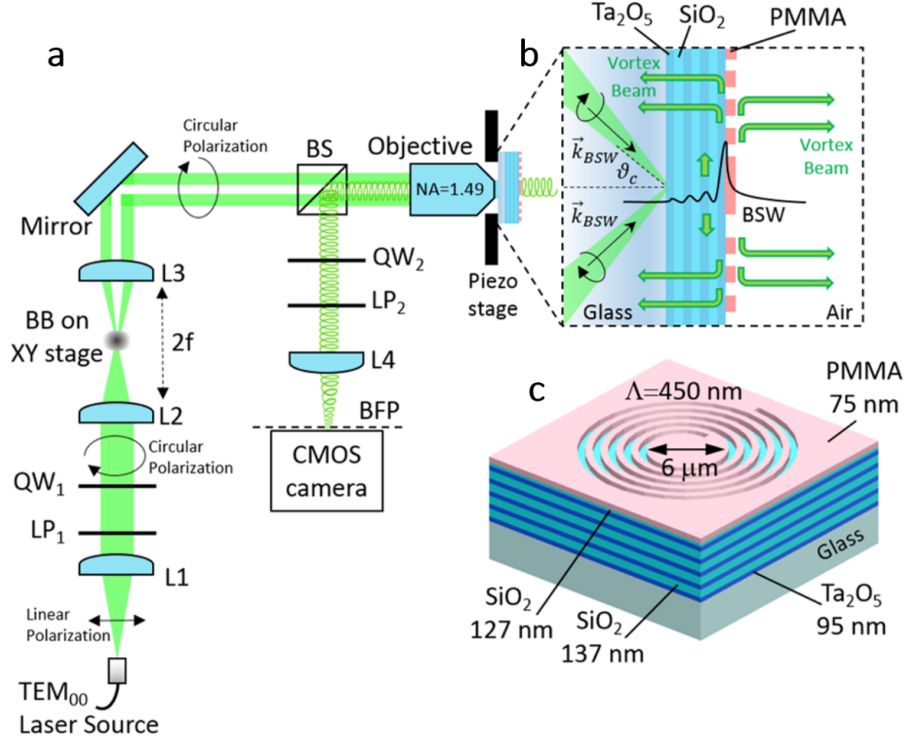


Figure 4.3: **a)** Sketch of the experimental setup. L_{1-4} Plano-Convex lenses, $LP_{1,2}$ Polarizers, $QW_{1,2}$ Quarter-wave Plates, BB Beam Blocker, BS Beamsplitter, BFP Back Focal Plane. In the exemplary BFP image, an interference pattern is shown, due to the superposition of a diffracted vortex beam and a reflected spherical wave from the sample surface. No beam blocker has been used in this case. **b)** Detailed view of the BSW coupling and diffraction mechanism. Illumination is provided by means of a beam-blocked circularly polarized laser beam focused through an oil immersion objective, such that the minimum incidence angle is slightly above the critical angle θ_c , in order to match the BSW coupling conditions. **c)** Sketch of the multilayer structure with an exemplary spiral diffraction grating fabricated in PMMA on top (not to scale).

layer on top of the stack is 127 nm thick. The stack sequence is the same as the 1DPC described in Chapter 3, unless the smaller number of layers. In this case, in fact, the purpose is not to reduce the leakage radiation or to enhance the LDOS at the surface, but to have a good coupling between the laser radiation and the BSW. On top of the structure a 75 nm thick layer of PMMA is spun for pattern fabrication ($n_{\text{PMMA}} = 1.48$). Chiral diffractive structures are fabricated by means of electron beam lithography. In Figure 4.4 SEM images of the patterned surface are shown.

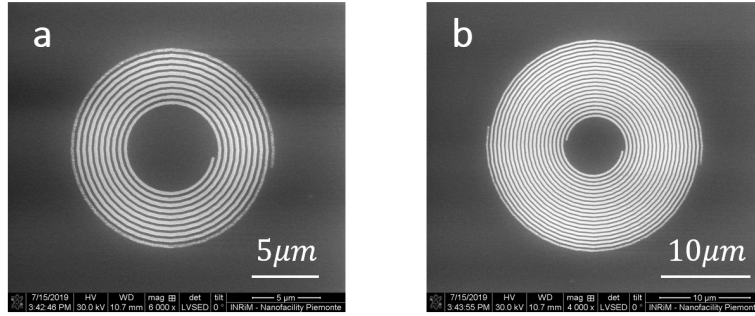


Figure 4.4: SEM image of the patterned surface of the 1DPC. The top layer of PMMA has been lithographed by means of electron beam lithography. **a)** Single-arm spiral grating. **b)** Double-arm spiral grating.

4.3.2 Experimental setup

The experimental setup is shown in Figure 4.3. A TEM_{00} doubled-frequency Nd:YAG laser beam (GEM, Laser Quantum) is collimated (L_1) and transmitted through a first polarization-control box, consisting of a linear polarizer LP_1 and a quarter wave plate QW_1 . Circular polarization states with both handedness (RH and LH) are generally produced. The laser beam is spatially filtered by means of a properly sized circular beam blocker. An oil-immersion objective ($\text{NA} = 1.49$) is back-contacted to a multilayer glass substrate, in order to focus the incoming beam onto a flat area of the top surface. The sample holder is mounted on a 3-axis piezo stage. Thanks to the beam blocker, only focused light propagating at angles larger than the glass/air critical angle θ_c can reach the sample. A fraction of the incoming power is thus available for coupling to BSWs, provided that wavelength, momentum and polarization matching conditions are fulfilled, as explained in Section 1.3. Since the coupling mechanism is polarization-sensitive and the incident electric field is circularly polarized, BSWs are spreading radially from the focused spot area, with an accumulated phase delay that is linearly varying with the azimuthal angle of the propagation direction. As a result, an omnidirectional BSW is obtained, with a peculiar spiral-like wavefront profile, analogous to plasmonic

vortices [185]. Surrounding the flat coupling region, an axis-symmetric diffractive grating is etched in the PMMA layer. The grating operates as an outcoupler, by diffracting BSWs out-of-plane in both substrate (glass) and cladding (air) media, along a direction close-to-normal to the sample surface (order of diffraction $n = -1$) [193]. Depending on the grating shape (e.g. circular or spiral-like), an additional geometrical phase profile can be imparted to the diffracted radiation. In previous applications, this feature has been exploited for steering the diffracted beam [148, 194]. When measuring the diffraction patterns from the spiral gratings, the excitation laser is accurately focused onto the geometric center of the diffraction gratings. The outcoupled power is then collected by the same high-NA objective and directed toward the collection arm of the setup, after passing through a 50/50 beam splitter. A second polarization-control box consisting of a quarter wave plate QW_2 and a linear polarizer LP_2 filters the outgoing wave onto the desired polarization state (RHC, LHC or LP). Subsequently, the lens L_4 images the BFP of the objective onto a CMOS camera (Thorlabs HR-CMOS DCC3260M). If the beam blocker is removed, an interference pattern as shown in Figure 4.5 can be obtained, due to the superposition of the light reflected by the multilayer inside the light cone ($NA \leq 1$) with the diffracted BSW patterns, eventually carrying OAM. As a result, spiral-like interference fringes can be observed depending on the OAM number l , as shown in Figure 4.5 [191].

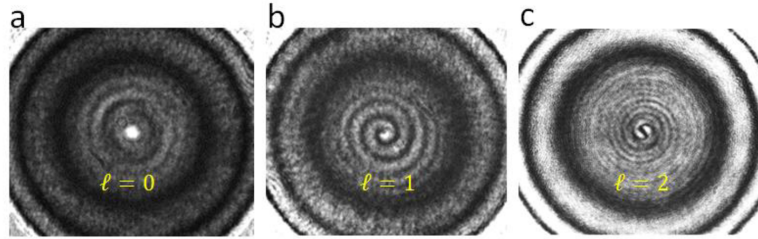


Figure 4.5: Interference patterns within $NA \leq 1$ collected when no beam blocker is used in the experimental setup. The spherical wavefront of the reflected light illuminating the sample surface below the critical angle interferes with a: **a)** $l = 0$, **b)** $l = 1$ and **c)** $l = 2$ beam.

4.4 Numerical modeling

Numerical modeling is performed using the FDTD method in the Lumerical Inc. software. In order to mimic the focused circularly polarized light coupling to BSWs, a pair of orthogonal dipolar emitters are positioned at the geometric center of the spiral grating. More specifically, the emitters are placed 10 nm above the PMMA layer, with the dipole momentum laying parallel to the multilayer surface,

such that the TE polarization of the BSW can be matched. The two oscillators are phase-shifted by $\pm\pi/2$. In this way, thanks to a near-field interaction, part of the radiated energy from the dipoles is transferred to BSWs (BSW-coupled emission, see Section 3.3). As shown in Figure 4.6, resulting BSWs are radially propagating, with a spiral wavefront due to the time-varying polarization matching conditions of the field given by the coherent sum of the radiation from the two dipoles.

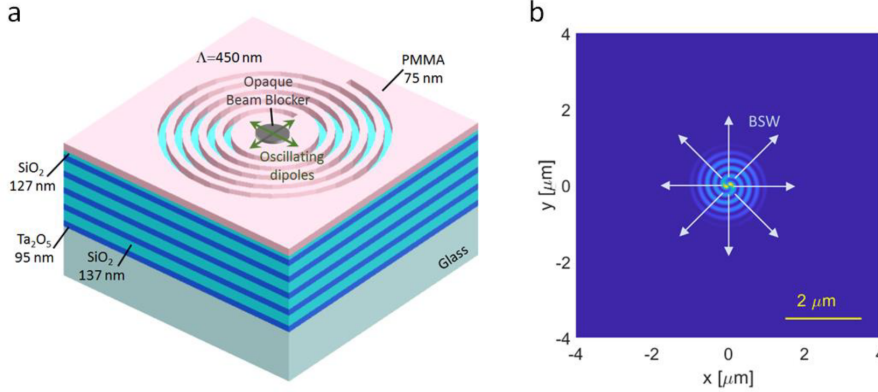


Figure 4.6: **a)** 3D sketch of the structure used in the FDTD model. A pair of orthogonal oscillating dipoles is located at the spiral center, with the dipole momenta laying on the multilayer surface. A phase delay $\pi/2$ is introduced between the oscillators. In order to avoid the direct emission of the dipoles in air, a metallic cover is placed few nanometers above the oscillators. In this way, the only contribution to the far-field pattern in air is due to the BSW-coupled emission diffracted by the grating. **b)** Exemplary near-field $E_{NF}(x, y; t) = \sqrt{E_x^2 + E_y^2 + E_z^2}$ of an omnidirectional BSW propagating radially from the dipole area towards the surrounding diffractive structure. The overall time-varying BSW near-field is given by the coherent sum of the BSW-coupled emission from the individual dipoles. The dipole excitation is time-limited to a pulse duration of 3.23 fs, peaked at $\lambda = 532$ nm with a spectral width $\Delta\lambda = 126$ nm.

The diffraction gratings are modeled as circular or spiral grooves in the PMMA layers, with a spatial period $\Lambda = 450$ nm. The total simulation region has dimensions $(15 \times 15 \times 2.6) \mu\text{m}^3$. Boundary conditions are set as perfectly matched layers. The smallest mesh size is 23 nm. The electromagnetic near-field is collected using a spatial monitor over a plane 23 nm above the PMMA layer. A near-to far-field projection technique is applied to calculate the field at a distance of 1 m from the structure, on the air side. A cylindrical perfect electric conductor, placed 50 nm above the dipole sources, have been introduced in order to avoid the direct free-space emission from the sources, which could produce interference with the BSW-diffracted radiation we want to investigate. This metallic plate mimics the role of the beam blocker in the experimental setup. With this arrangement, only

the air-side far-field patterns are calculated. However, as the propagation angles of the diffracted beams (with respect to the multilayer normal) are very small, the refraction effects are negligible and the far-field patterns are expected to be similar to those on the glass substrate side.

4.5 Analysis of spiral radiation patterns

In this Section, experimental results are presented related to (i) a circular-symmetric annular grating with topological charge $m = 0$, (ii) a single-arm spiral grating, (iii) a double-arm spiral grating. In the last two cases, both handedness of the incident polarization are considered, namely RHC and LHC polarizations, such that the incident beam SAM and the grating topological charge can have either equal or opposite sign. The polarization state of diffracted light is evaluated for each wavevector across the BFP through the polarization ellipse parameters $\epsilon(k_x, k_y)$ and $\alpha(k_x, k_y)$ [154]. The Stokes parameters are used for the evaluation of $\epsilon(k_x, k_y)$ and $\alpha(k_x, k_y)$, as explained in Section 4.1.2. For each of the following annular outcoupler considered, a complete set of the Stokes parameters S_1 , S_2 and S_3 across the BFP is presented in Appendix 1, along with 6 BFP measurements that led to the evaluation of each of them.

4.5.1 Circular outcoupler ($m = 0$)

In this configuration, a RHC circular polarization ($\epsilon = \pi/4$) is employed to couple BSWs that are then diffracted. As shown in Figure 4.7a,e, the total intensity collected on the BFP exhibits a maximum at $k_x = k_y = 0$, corresponding to a constructive interference condition for light traveling along a direction perpendicular to the multilayer surface. A linear-polarization filtering reveals the presence of a pair of spiral-like arms spreading from the central maximum that rotate as the polarization analyser is rotated (in Figure 4.7b,f the measured and calculated intensity of the x -component of the diffracted light are presented). Without the polarization filter, the spiral-like arms merge together to form a ring surrounding the central maximum. When polarization-projected onto a RHC polarization state, the intensity pattern has still a maximum in the BFP center (Figure 4.7c,g), while a weak ring is obtained for a projection onto a LHC polarization state (Figure 4.7d,h). A comparison between the distributions for the measured and the calculated parameter $\epsilon(k_x, k_y)$ on the BFP indicates that the central maximum is substantially RHC polarized, i.e. $\epsilon(0,0) \cong \pi/4$, while the outer ring is LHC polarized, i.e. $\epsilon(0,0) \cong -\pi/4$ (Figure 4.7i,l).

By enforcing the conservation of the total angular momentum \mathbf{J} , which also takes into account the topological charge m imparted by the diffraction grating, the following equation applies: $\sigma_i + m = 1 + 0 = \sigma_0 + l$, where σ_0 is the output SAM

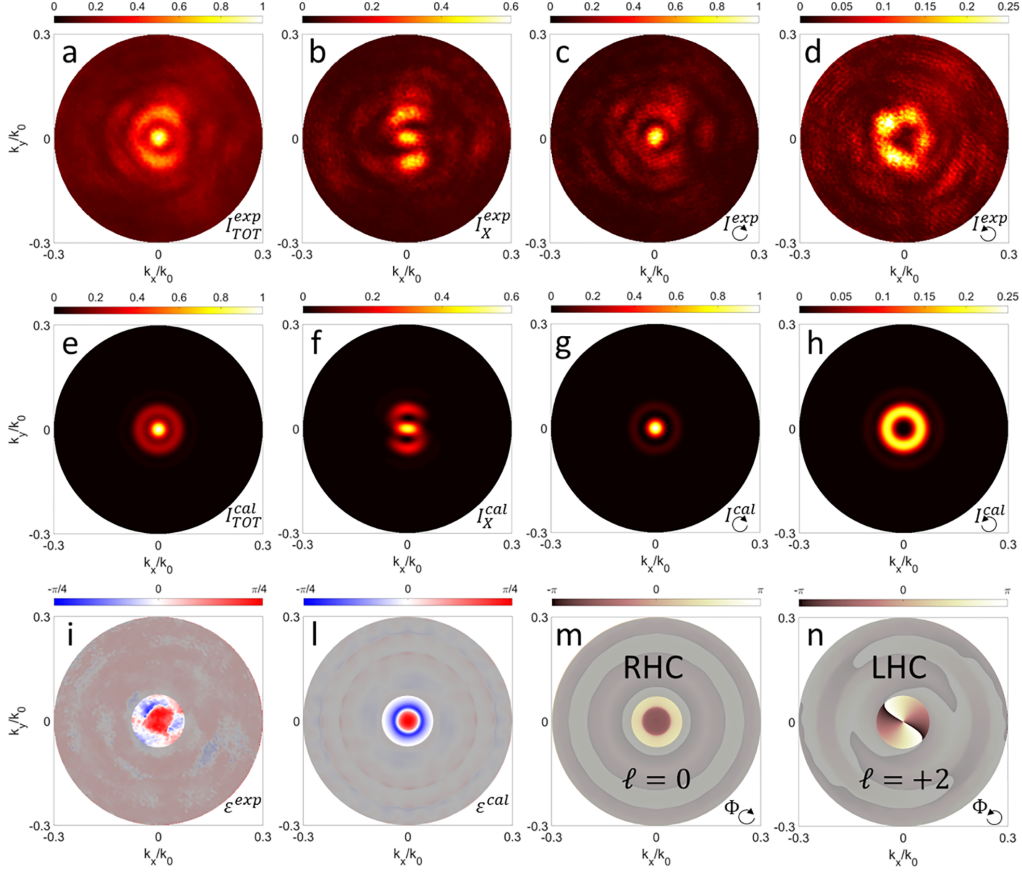


Figure 4.7: BFP Diffraction patterns from a circular outcoupler ($m = 0$). Incident polarization is RHC. **a,e**) experimental and calculated total intensity showing a central spot surrounded by a weak outer ring; **b,f**) experimental and calculated x -polarized intensity; **c,g**) experimental and calculated RHC intensity showing a central spot; **d,h**) experimental and calculated LHC intensity showing a doughnut shape; **i,l**) experimental and calculated polarization ellipse parameter $\epsilon(k_x, k_y)$ with the sign reversal from the inner area to the outer ring; **m**) calculated phase of the diffracted field with RHC polarization, showing a constant distribution; **n**) calculated phase of the diffracted field with LHC polarization, showing two 2π discontinuities.

number and l is the corresponding OAM number. The solution to this equation is not unique. In particular, two SAM-OAM configurations are possible: a RHC beam preserving the input polarization and carrying zero OAM, i.e. $\sigma_0 = +1$ and $l = 0$, and a doughnut LHC beam with a reverse polarization, with $\sigma_0 = -1$ and OAM with $l = +2$. The two beams are partially overlapped. This observation is supported by the phase distribution calculated for the RHC and the LHC polarized fields presented in Figure 4.7m,n: a flat wavefront with constant phase is found for the RHC beam ($l = 0$) and a spiral wavefront with two 2π discontinuities for the LHC beam ($l = +2$).

4.5.2 Spiral outcoupler ($m = -1$)

BSWs are first coupled with an input RHC polarization ($\sigma_i = +1$) and made interacting by a spiral grating with opposite handedness ($m = -1$). The corresponding intensity pattern is shown in Figure 4.8a,e. The phase delay profile imparted by the diffractive structure onto the diffracted BSWs results into a destructive interference such that a zero-intensity phase singularity is produced at $k_x = k_y = 0$. When filtered with the linear polarizer LP_1 (e.g. oriented along the x , y or 45° direction), two-lobe patterns are found, whose orientation is perpendicular to the analyser transmission axis (Figures 4.8b-d). Calculated intensity patterns are in good agreement with the experimental observations (Figures 4.8f-h). The distribution of the parameter $\epsilon(k_x, k_y)$ shows a substantially linear polarization corresponding to the doughnut ($\epsilon \cong 0$) (Figures 4.8i,l). The uniformity of the polarization orientation is evaluated by extracting the parameter $\alpha(k_x, k_y)$, introduced in Section 4.1.2, which provides the local orientation of the polarization ellipse (almost a line, in this case) across the BFP [154]. In Figures 4.8m,n both the experimental and the calculated distributions for $\alpha(k_x, k_y)$ indicate that the substantially linear polarization follows an axis-symmetric distribution such that the electric field is azimuthally oriented about the beam axis in $k_x = k_y = 0$. In this case, the \mathbf{J} conservation rule reads as $\sigma_i + m = 1 - 1 = \sigma_0 + l = 0$, leading to two fully overlapped beams with SAM $\sigma_0 = +1$ and OAM $l = -1$ and SAM $\sigma_0 = -1$ and OAM $l = +1$, respectively (see Figures A.3e,f and Figures A.4e,f in Appendix A). The coherent superposition of such beams having circular, yet orthogonal, polarizations is consistent with the observed azimuthal polarization state of the output beam.

When the illumination polarization is switched to LHC ($\sigma_i = -1$) the input SAM and the grating topological charge possess the same sign. The overall intensity pattern having a doughnut shape is presented in Figure 4.9a,e. At a closer look, the output results from the superposition of a pair of ring-shaped beams, which are non-interfering because of their orthogonal polarizations. A weak outer ring (Figure 4.9c,g) is imaged upon RHC filtering, while an intense inner ring (Figure 4.9d,h) is obtained upon LHC filtering. The experimental and the calculated distributions

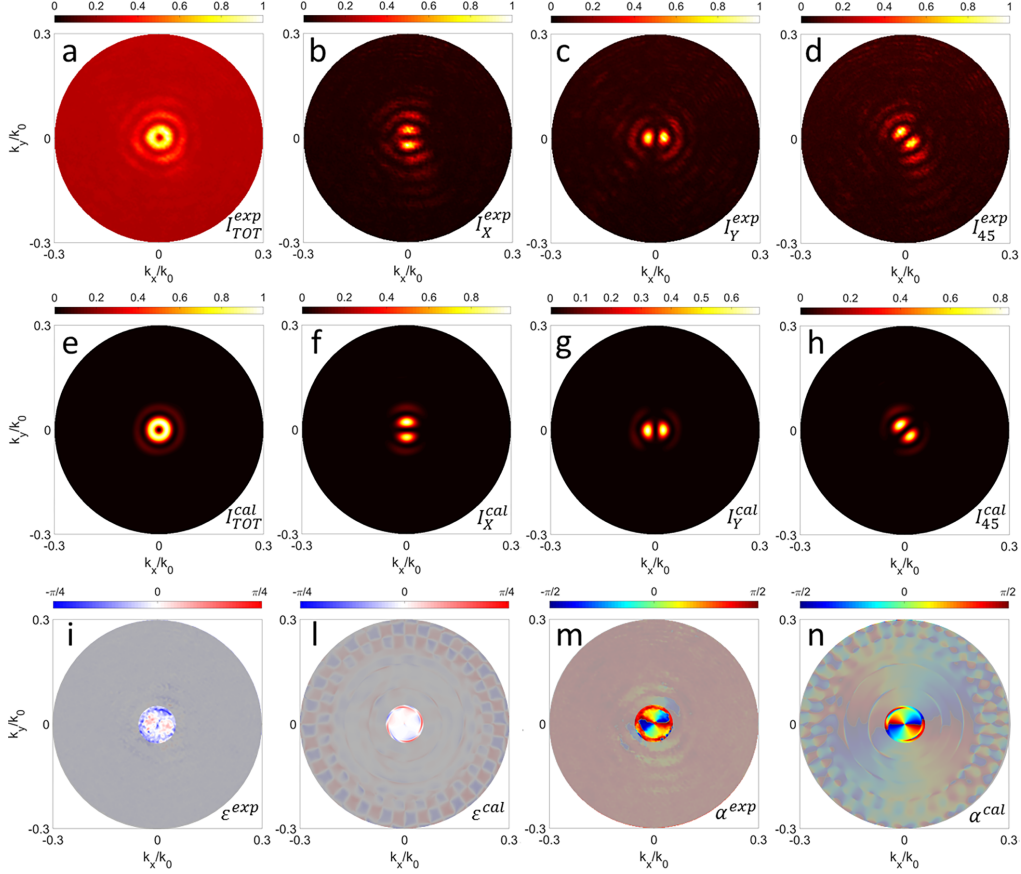


Figure 4.8: BFP Diffraction patterns from a 1-arm spiral outcoupler ($m = -1$). Incident polarization is RHC. **a,e**) experimental and calculated total intensity showing a doughnut shape; **b,f**) experimental and calculated x -polarized intensity; **c,g**) experimental and calculated y -polarized intensity; **d,h**) experimental and calculated 45° -polarized intensity; **i,l**) experimental and calculated polarization ellipse parameter $\epsilon(k_x, k_y)$ indicating a substantially linear polarization state $\epsilon \cong 0$; **m,n**) experimental and calculated ellipse parameter $\alpha(k_x, k_y)$ indicating an azimuthal orientation of the electric field.

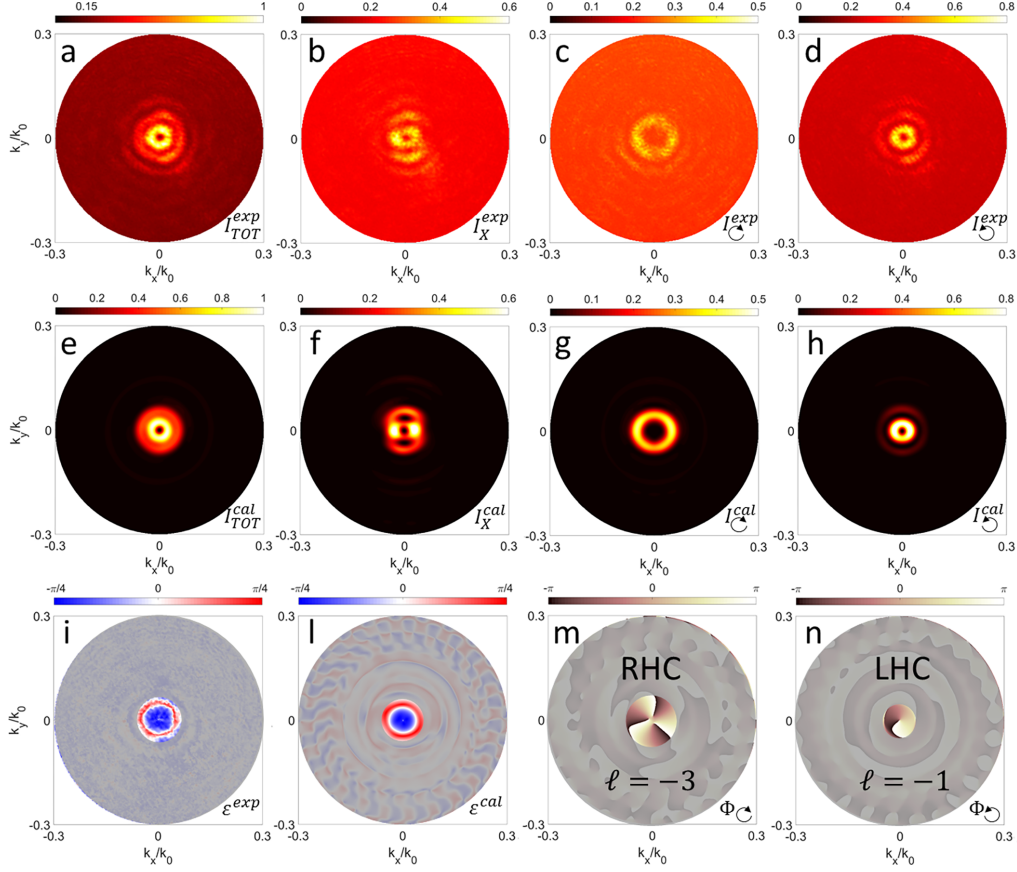


Figure 4.9: BFP Diffraction patterns from a 1-arm spiral outcoupler ($m = -1$). Incident polarization is LHC. **a,e**) experimental and calculated total intensity showing a superposition of an inner and an outer ring-shaped patterns; **b,f**) experimental and calculated x -polarized intensity; **c,g**) experimental and calculated RHC intensity, distributed according to the outer ring; **d,h**) experimental and calculated LHC intensity; distributed according to the inner ring; **i,l**) experimental and calculated polarization ellipse parameter $\epsilon(k_x, k_y)$ indicating a substantially circular polarization with handedness reversal from the inner to the outer ring; **m**) calculated phase of the diffracted field with RHC polarization, showing three 2π discontinuities; **n**) calculated phase of the diffracted field with LHC polarization, showing a 2π discontinuities.

for $\epsilon(k_x, k_y)$ (Figure 4.9i,l) confirm that the polarization state of the two beams is still substantially circular. However, a reversal of handedness from LHC to RHC can be found while moving from the inner ring toward the outer. The two partially overlapped beams must satisfy the \mathbf{J} conservation rule, i.e. $\sigma_i + m = -1 - 1 = \sigma_0 + l = -2$. A first solution to this equation is represented by a LHC polarized beam having the same SAM number as the incident radiation $\sigma_0 = -1$ and OAM $l = -1$. An orthogonal solution is a RHC polarized beam having a reversed SAM $\sigma_0 = +1$ and OAM $l = -3$. The topological charge of the diffracted vortex beams can be directly appreciated from the calculated phase distributions of the RHC and LHC polarized beams (Figure 4.9m,n), exhibiting three and one 2π discontinuities respectively, on the BFP.

4.5.3 Spiral outcoupler ($m = -2$)

As in the previous configuration, an incident RHC polarization ($\sigma_i = +1$) is first considered. The overall intensity shown in Figure 4.10a,e is obtained as the superposition of a weak outer ring and a brighter central spot. Both patterns can be individually imaged by operating a polarization filtering through a RHC state (Figure 4.10c,g) and a LHC state (Figure 4.10d,h), respectively. The distribution of the parameter $\epsilon(k_x, k_y)$ indicates that the polarization is substantially circular across the pattern. However, the bright central spot shows a LHC polarization state, which is reversed with respect to the incident radiation (Figure 4.10i). Furthermore, the outer weak ring maintains a LHC polarization, as the illumination (Figure 4.10l). The conservation of the momentum \mathbf{J} leads to $\sigma_i + m = +1 - 2 = \sigma_0 + l = -1$, which has the following two solutions associated to the observed beams: $\sigma_0 = +1$ (RHC) and $l = -2$; $\sigma_0 = -1$ (LHC) and $l = 0$. The calculated phase distributions are consistent with the total angular momentum algebra, since the RHC beam has a vortex wavefront with two 2π discontinuities, while the LHC beam has a flat wavefront (Figure 4.10m,n). A constant phase is also consistent with the existence of a central maximum at $k_x = k_y = 0$ for the LHC beam.

For a LHC polarization ($\sigma_i = -1$) a phase singularity is produced on the optical axis, and the overall intensity pattern (Figure 4.11a,e) results from the superposition of a LHC polarized inner ring (Figure 4.11c,g) and a RHC polarized outer ring (Figure 4.11d,h). Measured and calculated $\epsilon(k_x, k_y)$ show the handedness reversal occurring when departing from the optical axis toward larger propagation angles, wherein the inner ring preserves the same polarization as the incident radiation (Figure 4.11i,l). From the conservation of the momentum \mathbf{J} , we have: $\sigma_i + m = -1 - 2 = \sigma_0 + l = -3$, which has the following solutions: $\sigma_0 = +1$ (RHC) and $l = -4$; $\sigma_0 = -1$ (LHC) and $l = -2$. In this case, both beams exhibit a phase vorticity, with four 2π discontinuities for the RHC (Figure 4.11m) state and two 2π discontinuities for the LHC state (Figure 4.11n).

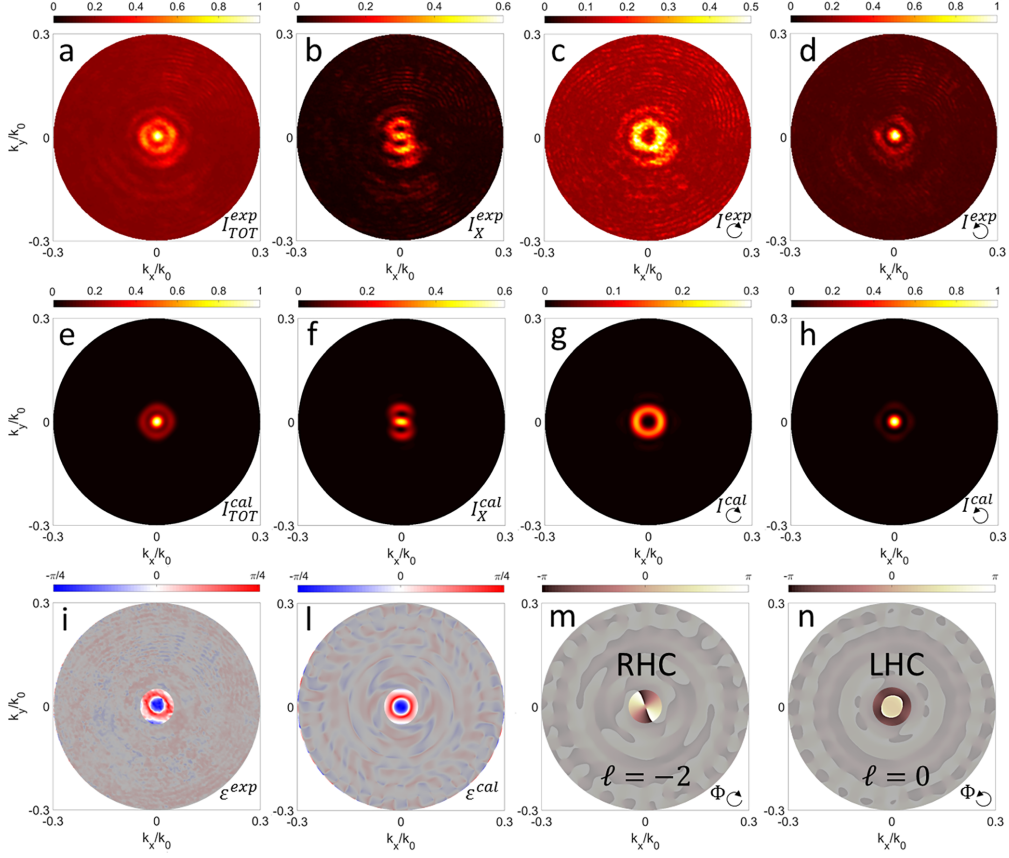


Figure 4.10: BFP Diffraction patterns from a 2-arms spiral outcoupler ($m = -2$). Incident polarization is RHC. **a,e**) experimental and calculated total intensity, given by the superposition of a central spot and a weaker outer ring; **b,f**) experimental and calculated x -polarized intensity; **c,g**) experimental and calculated RHC intensity, distributed according to the weak outer ring; **d,h**) experimental and calculated LHC intensity, distributed according to the bright central spot; **i,l**) experimental and calculated polarization ellipse parameter $\epsilon(k_x, k_y)$ indicating a substantially circular polarization, with handedness reversal from the central spot to the outer ring; **m**) calculated phase of the diffracted field with RHC polarization, showing two 2π discontinuities; **n**) calculated phase of the diffracted field with LHC polarization, showing a uniform phase distribution.

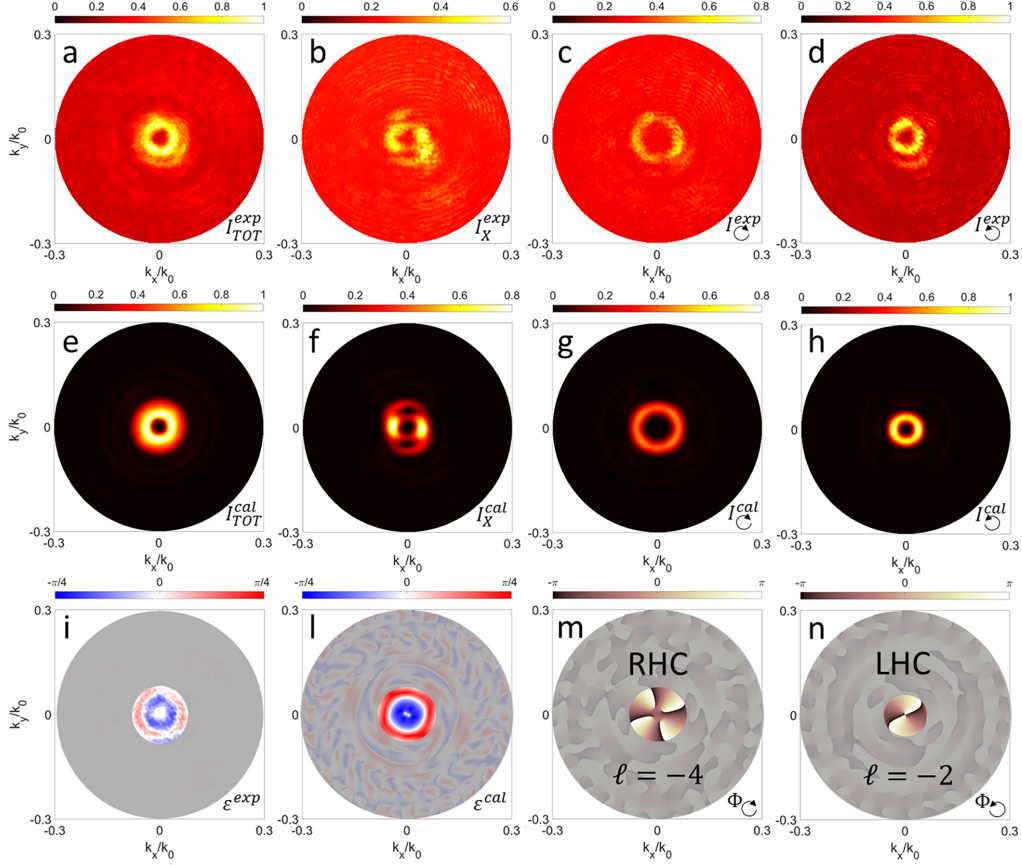


Figure 4.11: BFP Diffraction patterns from a 2-arm spiral outcoupler ($m = -2$). Incident polarization is LHC. **a,e**) experimental and calculated total intensity; **b,f**) experimental and calculated x -polarized intensity; **c,g**) experimental and calculated RHC intensity; **d,h**) experimental and calculated LHC intensity; **i,l**) experimental and calculated polarization ellipse parameter $\epsilon(k_x, k_y)$; **m**) calculated phase of the diffracted field with RHC polarization showing four 2π discontinuities; **n**) calculated phase of the diffracted field with LHC polarization, showing two 2π discontinuities.

4.6 Conclusion

To conclude, a new mechanism for the generation of vectorial vortex beams has been presented in this Chapter, based on spin-orbit interactions involving coupling and diffraction of BSWs. Generally speaking, this kind of effects relies on the coherence characteristics of the radiation involved. For this reason, a laser beam has been employed as an external free-space radiation for coupling BSWs that are subsequently diffracted, with an imparted geometrical phase. Several combinations of polarization states and OAM are obtained, as summarized in Table 1. Further options for vortex beam generation carrying OAM with other polarization configurations can be possibly produced by means of multilayers supporting TM-polarized, in addition to TE-polarized BSWs [195].

	Grating Topological Charge m	$m = 0$	$m = -1$	$m = -2$
Incident SAM σ_i				
$\sigma_i = +1$		$\sigma_o = -1$ & $\ell = +2$ $\sigma_o = +1$ & $\ell = 0$	$\sigma_o = -1$ & $\ell = +1$ $\sigma_o = +1$ & $\ell = -1$	$\sigma_o = -1$ & $\ell = 0$ $\sigma_o = +1$ & $\ell = -2$
$\sigma_i = -1$		$\sigma_o = -1$ & $\ell = 0$ $\sigma_o = +1$ & $\ell = -2$	$\sigma_o = -1$ & $\ell = -1$ $\sigma_o = +1$ & $\ell = -3$	$\sigma_o = -1$ & $\ell = -2$ $\sigma_o = +1$ & $\ell = -4$

Figure 4.12: Summary of the SAM-OAM combinations obtained by diffraction of BSWs coupled from either RHC or LHC polarized incident light.

The numerical model developed here suggests that the presented approach is likely to work regardless of the coupling mechanism for BSWs. For example, in the perspective of advanced engineered light sources for free-space applications, BSWs can be launched from a single emitter on the multilayer surface by virtue of near-field interactions (BSW-coupled emission, see Section 3.3) [39, 196]. Then, chiral diffractive structures can be used as outcouplers surrounding single sources or even planar BSW cavities (e.g. as described in ref. [97]) hosting light sources within. Provided the coherence requirements for the BSW-coupled radiation leaking out of the cavity are satisfied, the diffraction mechanism for free-space vortex generation remains as reported in the text above. While nanocavities can be chiral themselves, with a handedness-dependent LDOS [197], it has been recently shown that chiral plasmonic structures can foster sources located on their surface to radiate according to a specific circular polarization handedness [198]. These strategies provide an unprecedented degree of control on the polarization state of the emitted light. The use of BSWs as a mean for coupling and transferring energy from sources to free-space, mediated by chiral diffractive gratings, can contribute to enhance the performance of purely plasmonic nanostructures, which are often limited by the strong absorption occurring at visible frequencies.

Summary and perspectives

The focus of the current thesis regards multilayered photonic structures sustaining electromagnetic surface waves. In this work, I demonstrated that the implementation of structured multilayers can be advantageous in manipulating the light at the nanoscale, promoting rich physics and possible device applications. Electromagnetic surface waves sustained by the multilayers are the main actors of this work.

The first part of this thesis dealt with the beaming of the fluorescence from emitters coupled to Tamm plasmon polaritons. In particular, a novel approach has been presented based on a nanohole in the metallic film, ranging from 200 nm to 1 μm in diameter, through which emitters can couple to TPP. The nanoaperture avoids the embedding of the emitters beneath the metallic film, which is not favorable for applications in fluorescence sensing or imaging. The increased directionality and beaming of the emission coupled to TPP is demonstrated experimentally through back focal plane images of the fluorescence intensity. The observations confirm that for λ such that $\mathbf{k}_{TPP}(\lambda) = 0$ the coupled emission appears in the direction normal to the glass, following the dispersion of TPP. Experimental observations are well supported by rigorous calculations, performed by means of a FDTD model. Further investigations confirmed that other nanoaperture shapes can be employed without losing the beneficial coupling to TPP.

The second part of the thesis is focused on Bloch surface waves manipulation on one-dimensional photonic crystal. In Chapter 3, the realization of circular cavities based on Bloch surface wave for the enhancement of the spontaneous emission decay rate has been described. The cavity is realized on top of the 1DPC by means of a circular grating, acting as a distributed Bragg reflector for the BSW-coupled emission from emitters embedded in the center of the cavity. Rigorous 2D and 3D FDTD simulations have been implemented to design the cavity and to fully characterize the cavity mode for the wavelength range of interest, calculating the mode profile, the mode dispersion and the quality factor. The fabricated devices have then been analyzed using a streak-camera based spectroscopic setup, in order to collect the spectral and temporal signature of the emission coupled to the BSW cavity mode. The spectrum of the coupled emission from the all dielectric cavity presents narrow peaks according to the calculated $Q \sim 1400$. Regarding the

temporal signature, the decay curves highlight an enhancement of the decay rate, giving an estimation of the Purcell factor of $P_f \sim 31$. An accurate fitting procedure (stretched exponential) has been implemented in order to grasp all the aspects of the complicated coupling mechanism inside the center of the cavity. In a further step, an outcoupling mechanism is introduced based on circular diffraction gratings surrounding the cavity, in order to control the extraction from the multilayer. The outcoupler efficiently redirects the emission at normal direction with respect to the multilayer surface, as demonstrated by BFP measurements. Thus, the ability of this device to provide enhanced directional light emission is envisioned to be exploited for single photon source manipulation.

In Chapter 4, a mechanism for producing a vortex beam by exploiting BSW have been discussed. The vortex beam is generated in a two-step process, involving a SAM-to-OAM conversion from a focused circularly polarized beam into radially propagating BSWs and a BSW diffraction in free-space, with the additional phase distribution imparted by a spiral diffraction grating. Experimentally, BFP imaging plus Stoke's polarimetry techniques have been implemented in order to retrieve the angular distribution and polarization state of the diffracted light. Circular and spiral outcouplers with one and two arms have been characterized, by illuminating them with a circular polarized beam, testing both handednesses. The BFP diffraction patterns together with the calculated phase profiles of the diffracted beams have demonstrated that several combinations of polarization states and OAM can be obtained, depending on the handedness of the incoming polarization and the number of arms in the spiral outcoupler. The mechanism effectively generates a vortex beam carrying OAM at low NA. All the experimental observations are supported by numerical simulations of the system, performed in a rigorous 3D FDTD environment. In the perspective of advanced engineered light sources for free-space applications, chiral diffractive structures can be used as outcouplers surrounding single point-like sources.

The photonic structures discussed in this work can be an interesting substrate for manipulating and engineering single-photon emitters, that nowadays play an important role in many leading quantum technologies. There is still no "ideal" on-demand single-photon emitter, but a plethora of promising material systems have been developed. Recently, several works focused on single-photon emission from hexagonal boron nitride, a wide bandgap semiconductors with very high thermal and chemical stability. We envision the possibility to integrate this emerging two-dimensional material with the photonic structures presented in this work, in order to exploit the high influence of the electromagnetic surface waves on the photonic behaviour of the emitters near the surface.

Author's contribution

In the work presented in Chapter 2 and published in [85], the author was responsible for the FDTD simulations to support the experimental observation. Regarding the work discussed in Chapter 3 and published in [97], the author conducted the fabrication of the cavity+outcoupler system and was responsible for the construction of the experimental setup, the numerical simulations and the experimental characterization of the device. Regarding the work discussed in Chapter 4, the author conducted the design and the fabrication of the spiral diffraction grating and was responsible for the construction of the experimental setup, the numerical simulations and the experimental characterization of the device.

Appendix A

Stokes parameters of diffracted light from annular gratings

In the following, the Stokes parameters used for the evaluation of $\epsilon(k_x, k_y)$ and $\alpha(k_x, k_y)$ in the experiment described in Section 4.5 are presented. For each annular outcoupler considered in Section 4.5, a set of 6 intensity measurements with 6 different outgoing beam polarizations (H, V, 45, 135, RHC and LHC) have been carried out, by filtering the diffracted light with a quarter wave plate and a linear polarizer, as described in Section 4.3.2. Next, the Stokes parameters are retrieved through the 6 measurements (more details can be found in [153, 154]). Here the Stokes parameters S_i , $i = 1, 2, 3$ are normalized by S_0 and therefore range from -1 to $+1$. It should be noted that the intensity measurements are not background corrected, since this would invalidate the calculation of the Stokes parameters. That is why even away from the central region of the Back Focal Plane, the intensity is not exactly zero in some cases. The calculated Stokes parameters with FDTD Lumerical are presented, as well, showing perfect matching with the experimental evaluation.

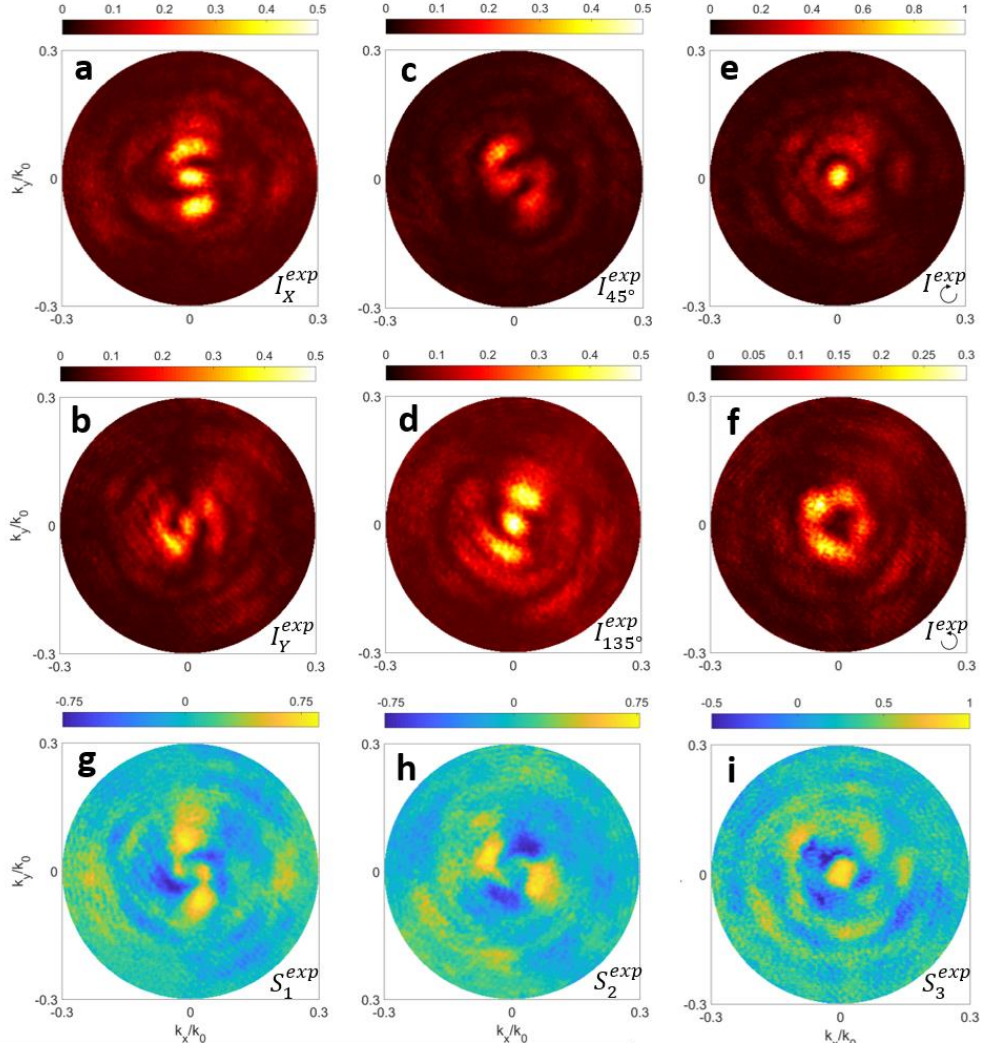


Figure A.1: Circular grating ($m = 0$): RHC polarized illumination. (a-f) Polarization-filtered intensities and (g-i) Stokes parameters (experimental).

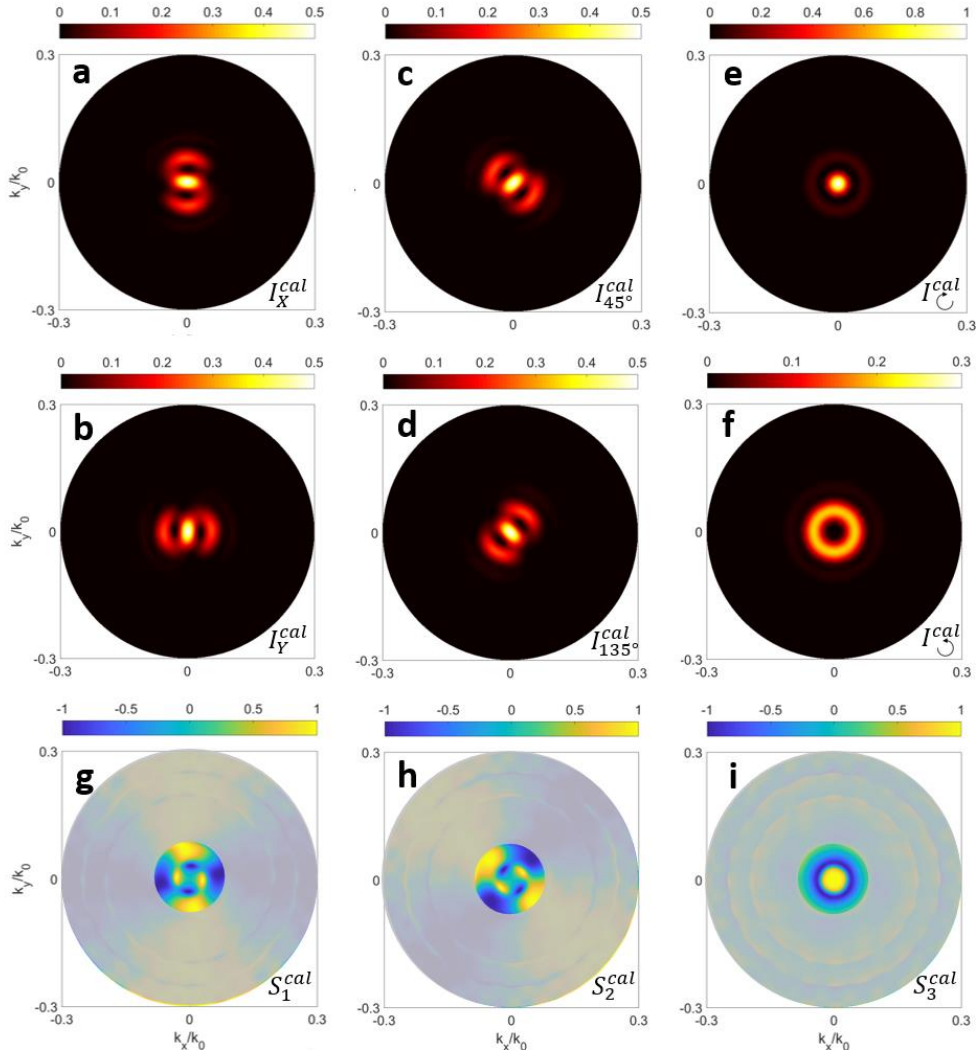


Figure A.2: Circular grating ($m = 0$): RHC polarized illumination. (a-f) Polarization-filtered intensities and (g-i) Stokes parameters (calculations).

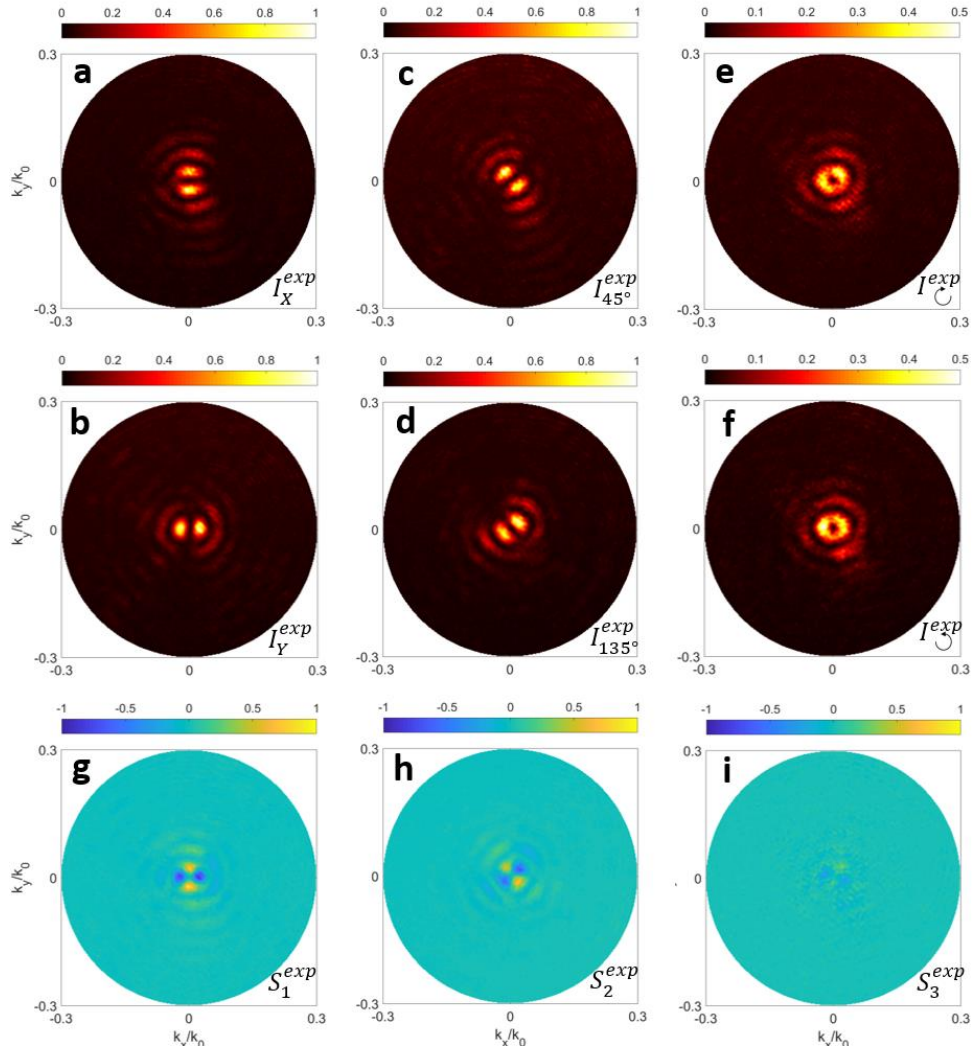


Figure A.3: Spiral grating ($m = -1$): RHC polarized illumination. (a-f) Polarization-filtered intensities and (g-i) Stokes parameters (experimental).

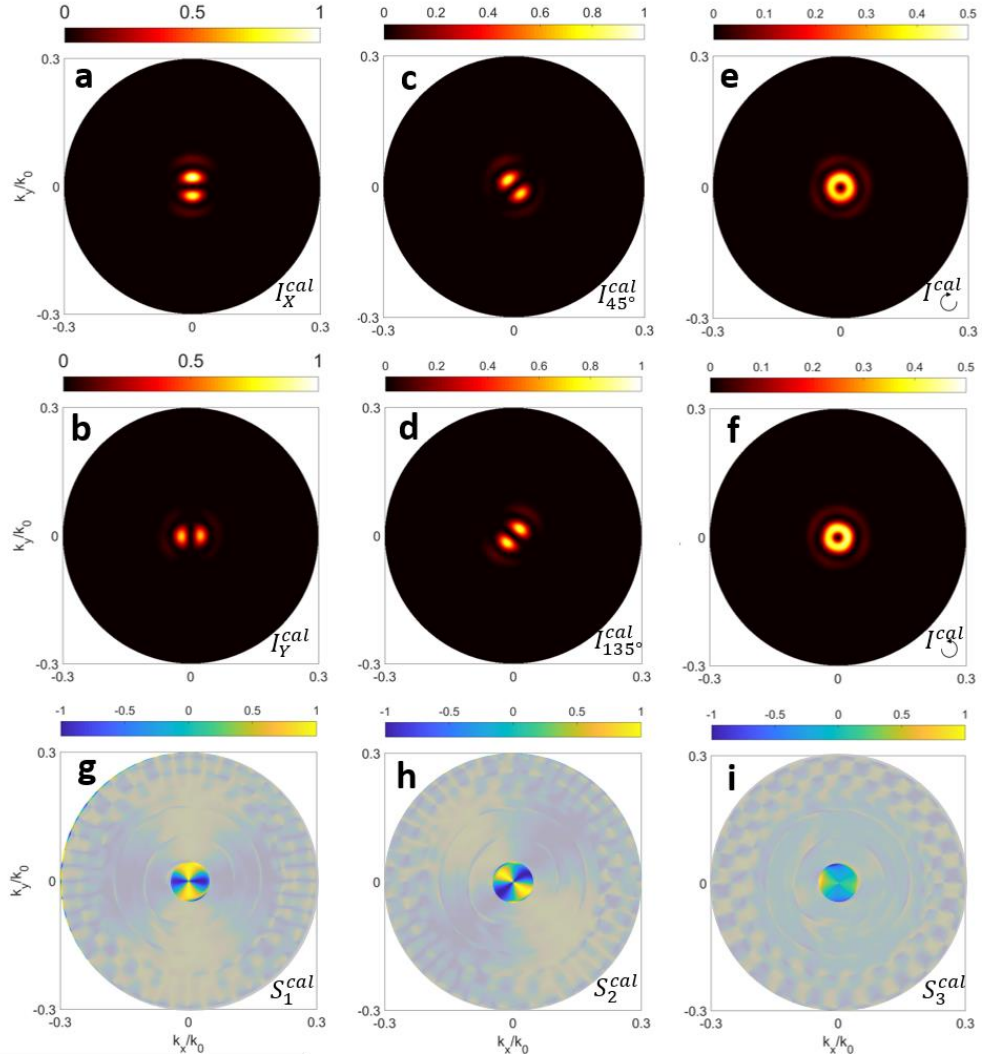


Figure A.4: Spiral grating ($m = -1$): RHC polarized illumination. (a-f) Polarization-filtered intensities and (g-i) Stokes parameters (calculations).

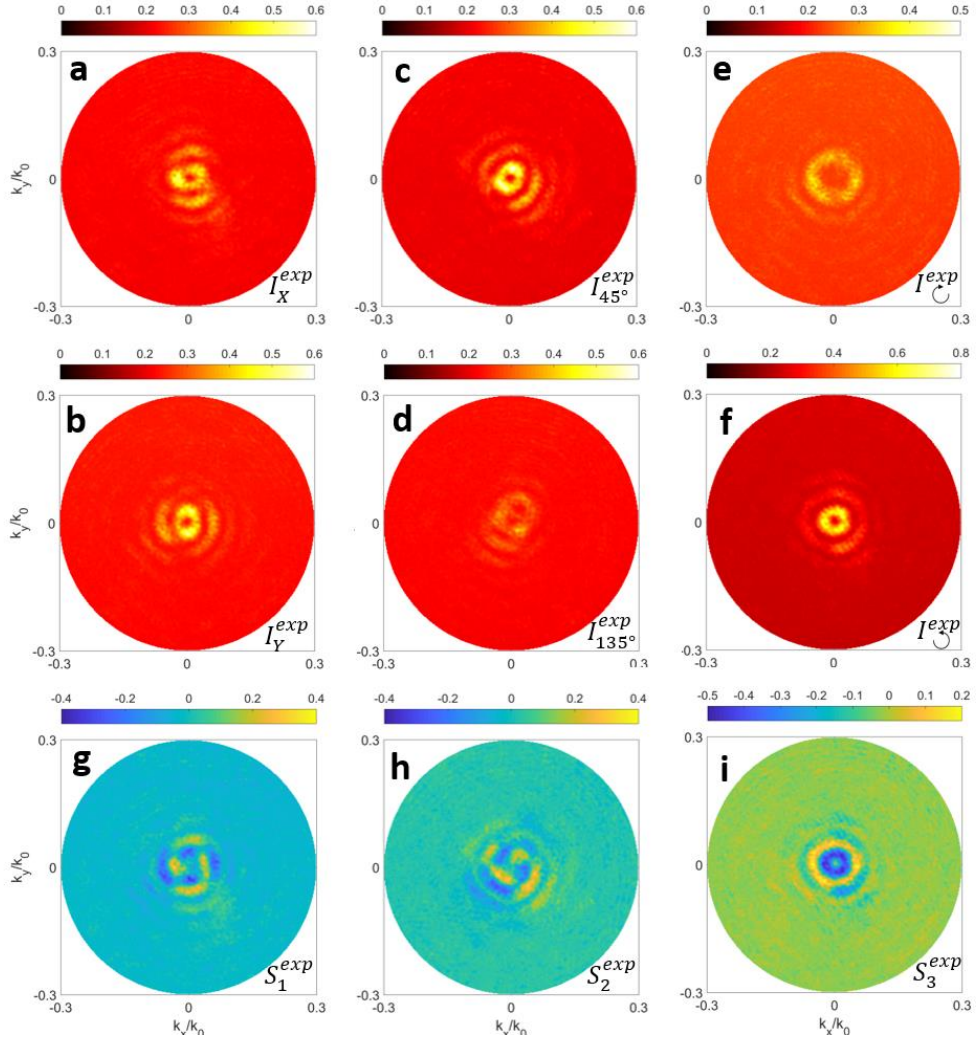


Figure A.5: Spiral grating ($m = -1$): LHC polarized illumination. (a-f) Polarization-filtered intensities and (g-i) Stokes parameters (experimental).

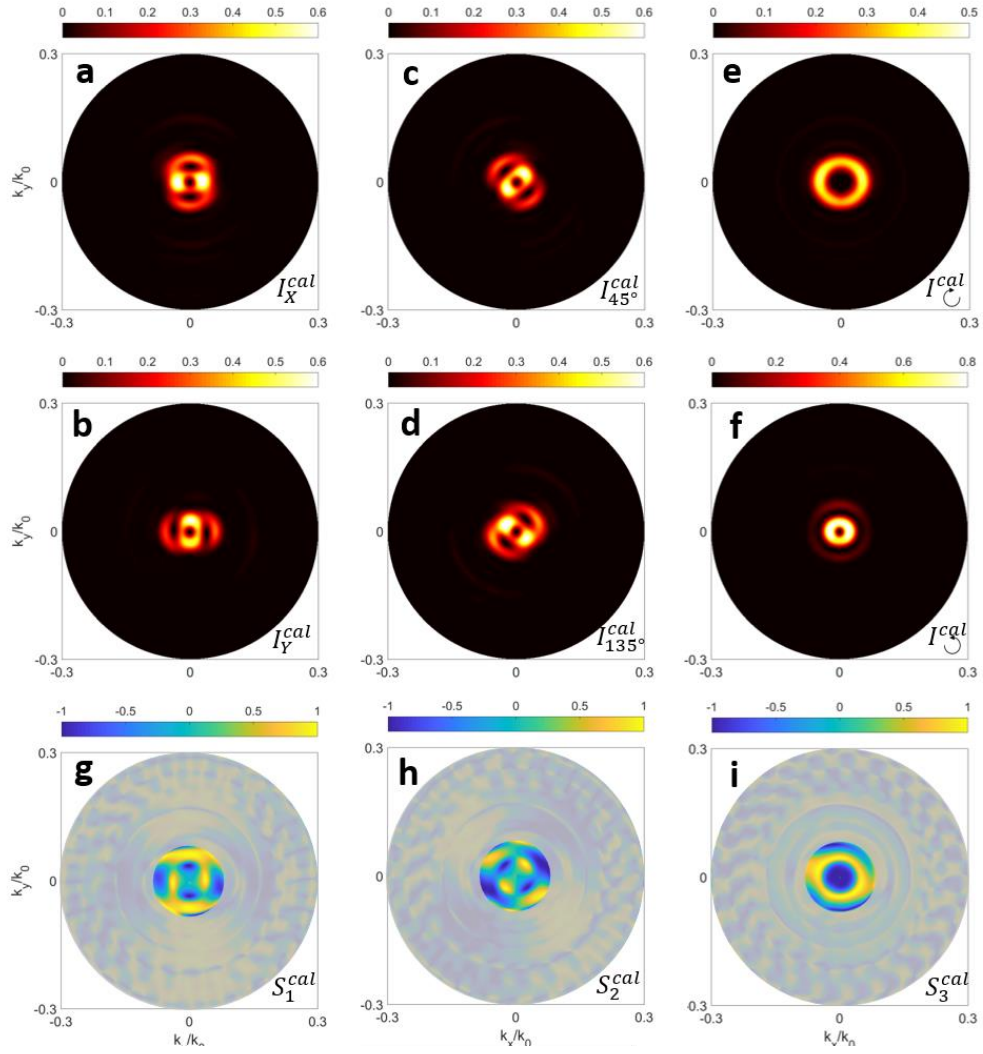


Figure A.6: Spiral grating ($m = -1$): LHC polarized illumination. (a-f) Polarization-filtered intensities and (g-i) Stokes parameters (calculations).

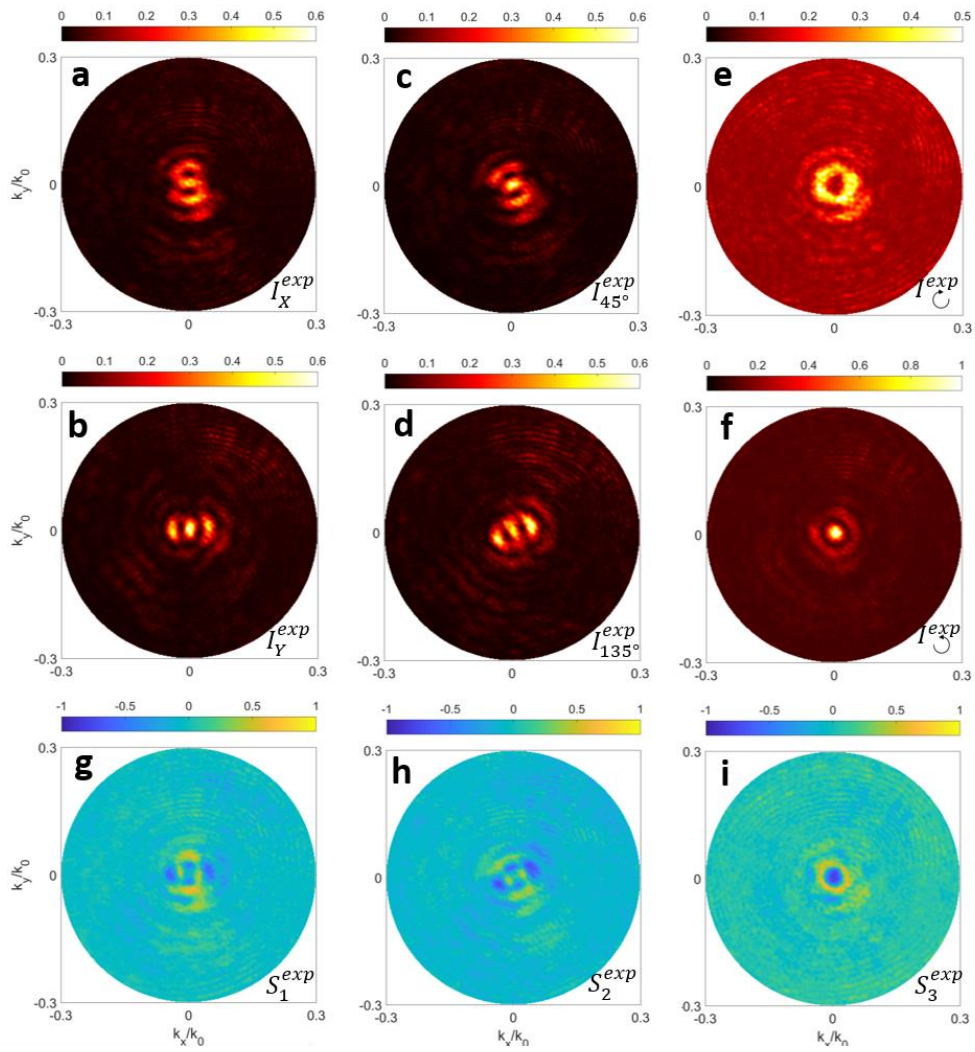


Figure A.7: Spiral grating ($m = -2$): RHC polarized illumination. (a-f) Polarization-filtered intensities and (g-i) Stokes parameters (experimental).

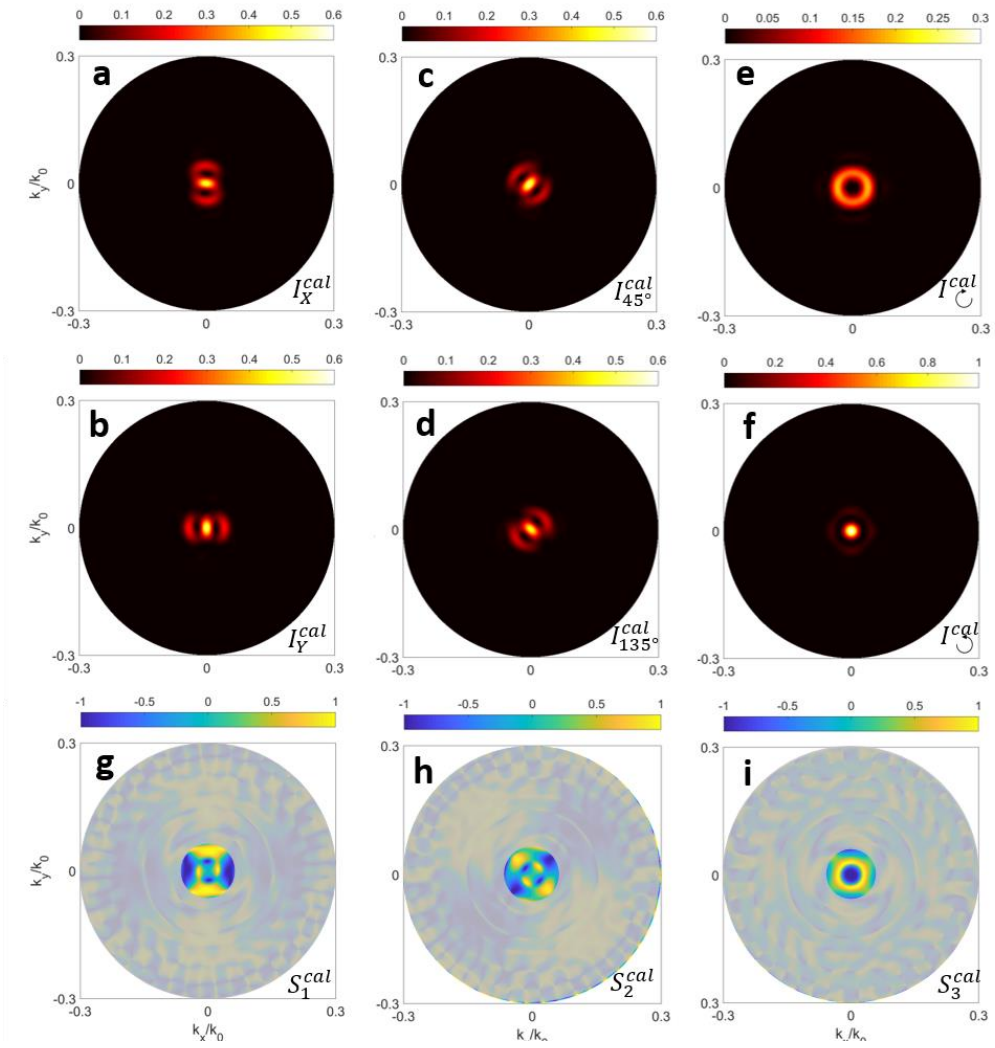


Figure A.8: Spiral grating ($m = -2$): RHC polarized illumination. (a-f) Polarization-filtered intensities and (g-i) Stokes parameters (calculations).

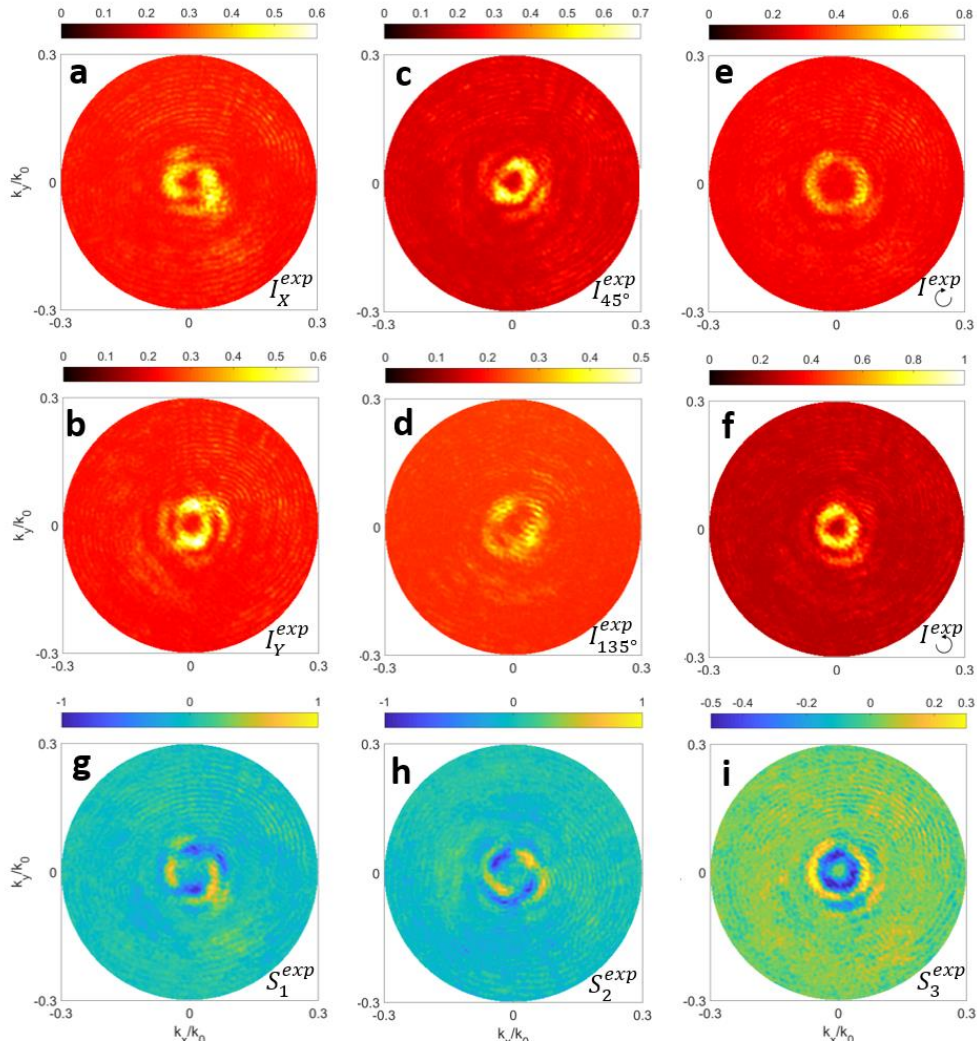


Figure A.9: Spiral grating ($m = -2$): LHC polarized illumination. (a-f) Polarization-filtered intensities and (g-i) Stokes parameters (experimental).

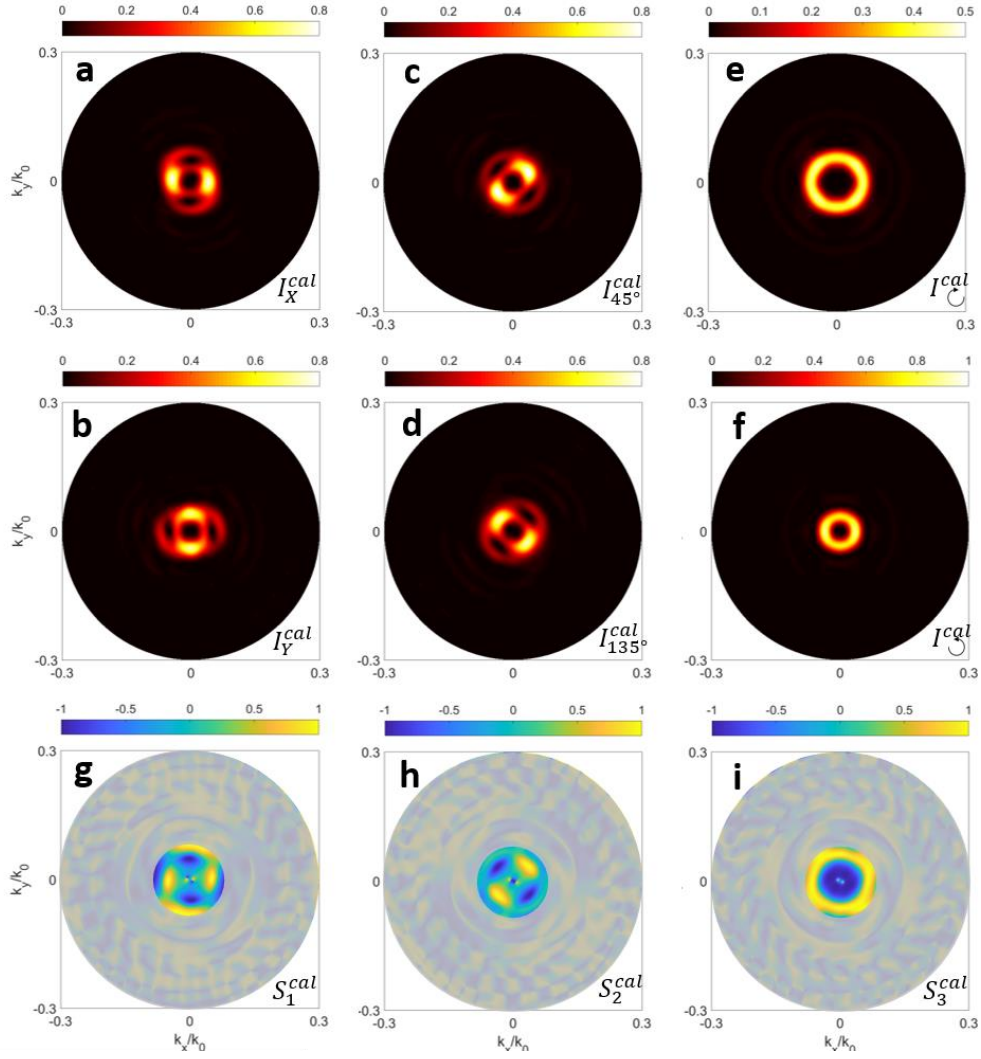


Figure A.10: Spiral grating ($m = -2$): LHC polarized illumination. (a-f) Polarization-filtered intensities and (g-i) Stokes parameters (calculations).

Bibliography

- [1] E. Yablonovitch. “Inhibited Spontaneous Emission in Solid-State Physics and Electronics”. In: *Phys. Rev. Lett.* 58 (1987), p. 2059.
- [2] E. Yablonovitch and T. J. Gmitter. “Photonic Band Structure: The Face-Centered-Cubic Case”. In: *Phys. Rev. Lett.* 63 (1989), p. 1950.
- [3] O. Painter et al. “Two-Dimensional Photonic Band-Gap Defect Mode Laser”. In: *Science* 284 (1999), pp. 1819–1821.
- [4] A. Erchak et al. “Enhanced coupling to vertical radiation using a two-dimensional photonic crystal in a semiconductor light-emitting diode”. In: *Appl. Phys. Lett.* 78 (2001), p. 563.
- [5] P. Russell. “Photonic Crystal Fibers”. In: *Science* 299 (2003), pp. 358–362.
- [6] L. Zeng et al. “Efficiency enhancement in Si solar cells by textured photonic crystal back reflector”. In: *Appl. Phys. Lett.* 89 (2006), p. 111111.
- [7] H. Inan et al. “Photonic crystals: emerging biosensors and their promise for point-of-care applications”. In: *Chem. Soc. Rev.* 46 (2017), pp. 366–388.
- [8] A. Kress et al. “Manipulation of the spontaneous emission dynamics of quantum dots in 2D photonic crystals”. In: *Phys. Rev. B* 71 (2005), p. 241304.
- [9] W. L. Barnes. “Fluorescence near interfaces, the role of photonic mode density”. In: *J. Mod. Opt.* 45 (1988), pp. 661–699.
- [10] S. Noda, M. Fujita, and T. Asano. “Spontaneous- emission control by photonic crystals and nanocavities”. In: *Nat. Photonics* 1 (2007), pp. 449–458.
- [11] W. Knoll. “Interfaces and thin films as seen by bound electromagnetic waves”. In: *Annu. Rev. Phys. Chem.* 49 (1998), pp. 569–638.
- [12] A. V. Zayats and I. I. Smolyaninov. “Near-field photonics: surface plasmon polaritons and localized surface plasmons”. In: *J. Opt. A Pure Appl. Opt.* 5 (2003), S16–S50.
- [13] P. Yeh. *Optical Waves in Layered Media*. John Wiley & Sons, 2005.
- [14] L. Novotny and B. Hecht. *Principles of nano-optics*. Cambridge Press, 2012.

- [15] J. W. Goodman. *Introduction to Fourier optics*. The McGraw-Hill companies, Inc., 1996.
- [16] P. Yeh, A. Yariv, and A. Y. Cho. “Optical surface-waves in periodic layered media”. In: *Applied Physics Letters* 32 (1978), p. 104.
- [17] P. Yeh, A. Yariv, and C. S. Hong. “Electromagnetic propagation in periodic stratified media I General theory”. In: *Journal of the Optical Society of America* 67 (1977), p. 423.
- [18] M. Liscidini and J. E. Sipe. “Analysis of Bloch-surface-wave assisted diffraction-based biosensors”. In: *J. Opt. Soc. Am. B* 26 (2009), pp. 279–289.
- [19] A. V. Kavokin. *Microcavities*. Oxford University Press, 2007.
- [20] A. Yariv. *Quantum Electronics*. John Wiley & Sons, 1989.
- [21] D. Aurelio and M. Liscidini. “Electromagnetic field enhancement in Bloch surface waves”. In: *Phys. Rev. B* 96 (2017), p. 045308.
- [22] F. Michelotti et al. “Fast optical vapour sensing by Bloch surface waves on porous silicon membranes”. In: *Phys. Chem. Chem. Phys* 12 (2010), pp. 502–506.
- [23] W. M. Robertson and M. S. May. “Surface electromagnetic wave excitation on one-dimensional photonic band-gap arrays”. In: *Applied Physics Letters* 74 (1999), p. 1800.
- [24] M. Liscidini. “Surface guided modes in photonic crystal ridges, the good, the bad, and the ugly”. In: *J. Opt. Soc. Am. B* 29 (2012), pp. 2103–2109.
- [25] M. Wang et al. “Magnetic spin-orbit interaction of light”. In: *Light: Sci. Appl* 7 (2018), p. 24.
- [26] M. S. Kim et al. “Multiple self-healing Bloch surface wave beams generated by a two-dimensional fraxicon”. In: *Commun. Phys.* 1 (2018), p. 63.
- [27] B. Vosoughi Lahijani et al. “Experimental demonstration of critical coupling of whispering gallery mode cavities on a Bloch surface wave platform”. In: *Opt. Lett.* 42 (2017), pp. 5137–5140.
- [28] M. Menotti and M. Liscidini. “Optical resonators based on Bloch surface waves”. In: *J. Opt. Soc. Am. B* 32 (2015), pp. 431–438.
- [29] R. Dubey et al. “Near-field characterization of a Bloch-surface-wave-based 2D disk resonator”. In: *Opt. Lett.* 41 (2016), pp. 4867–4870.
- [30] R. Wang et al. “Diffraction-Free Bloch Surface Waves”. In: *ACS Nano* 11 (2017), pp. 5383–5390.
- [31] R. Wang et al. “Bloch surface waves confined in one dimension with a single polymeric nanofiber”. In: *Nat. Commun.* 8 (2017), p. 14330.

- [32] H. K. Baghbadorani et al. “Guided modes in photonic crystal slabs supporting Bloch surface waves”. In: *J. Opt. Soc. Am. B* 35 (2018), pp. 805–810.
- [33] T. Sfez et al. “Bloch surface waves in ultrathin waveguides, near-field investigation of mode polarization and propagation”. In: *Appl. Phys. Lett.* 96 (2010), p. 151101.
- [34] T. Kovalevich et al. “Experimental evidence of Bloch surface waves on photonic crystals with thin-film LiNbO₃ as a top layer”. In: *Photonic Res.* 5 (2017), pp. 649–653.
- [35] M. Ballarini et al. “Bloch surface waves-controlled emission of organic dyes grafted on a onedimensional photonic crystal”. In: *Appl. Phys. Lett.* 99 (2011), p. 043302.
- [36] E. Descrovi et al. “Guided Bloch surface waves on ultrathin polymeric ridges”. In: *Nano Lett.* 10 (2010), pp. 2087–2091.
- [37] H. Raether. *Surface Plasmons*. Springer-Verlag, Berlin, 1988.
- [38] R. D. Maede et al. “Electromagnetic Bloch Waves at the surface of a photonic crystal”. In: *Phys. Rev. B* 44 (1995), p. 109601.
- [39] M. Liscidini et al. “Strong modification of light emission from a dye monolayer via Bloch surface waves”. In: *Opt. Lett.* 34 (2009), pp. 2318–2320.
- [40] R. Badugu et al. “Radiative decay engineering 6, fluorescence on one-dimensional photonic crystals”. In: *An. Biochem.* 442 (2013), pp. 83–96.
- [41] S. Pirotta et al. “Strong coupling between excitons in organic semiconductors and Bloch surface waves”. In: *Appl. Phys. Lett.* 104 (2014), p. 51111.
- [42] K. Ray, R. Badugu, and J. R. Lakowicz. “Bloch Surface Wave-Coupled Emission from Quantum Dots by Ensemble and Single Molecule Spectroscopy”. In: *RSC Adv.* 5 (2015), pp. 54403–54411.
- [43] M. N. Romodina et al. “Magneto-optical switching of Bloch surface waves in magnetophotonic crystals”. In: *J. Magn. Magn. Mater.* 415 (2016), pp. 82–86.
- [44] G. Lerario et al. “High-speed flow of interacting organic polaritons”. In: *Light: Sci. Appl.* 6 (2017), e16212.
- [45] R. Wang et al. “Two-Dimensional Photonic Devices based on Bloch Surface Waves with One-Dimensional Grooves”. In: *Phys. Rev. Appl.* 10 (2018), p. 024032.
- [46] M. Kaliteevski et al. “Tamm plasmon-polaritons: Possible Electromagnetic States at the Interface of a Metal and a Dielectric Bragg mirror”. In: *Phys. Rev. B* 76 (2007), p. 165415.

- [47] A. V. Kavokin et al. “Lossless interface modes at the boundary between two periodic dielectric structures”. In: *Phys. Rev. B* 72 (2005), p. 233102.
- [48] M. E. Sasin et al. “Tamm plasmon polaritons: slow and spatially compact light”. In: *Appl. Phys. Lett.* 92 (2008), p. 251112.
- [49] M- Lopez-Garcia et al. “Efficient out-coupling and beaming of Tamm optical states via surface plasmon polariton excitation”. In: *Appl. Phys. Lett.* 104 (2014), p. 231116.
- [50] A. V. Kavokin et al. “Room-temperature Tamm-plasmon exciton-polaritons with a WSe₂ monolayer”. In: *Nat. Comm.* 7 (2016), p. 13328.
- [51] A. R. Gubaydullin et al. “Enhancement of spontaneous emission in Tamm plasmon structures”. In: *Sci. Rep.* 7 (2017), p. 9014.
- [52] P. Mandracci and C. Ricciardi. “Silicon–carbon–oxynitrides grown by plasma-enhanced chemical vapor deposition technique”. In: *Thin Solid Films* 515 (2007), pp. 7639–7642.
- [53] F. Giorgis et al. “Luminescence processes in amorphous hydrogenated silicon-nitride nanometric multilayers”. In: *Phys. Rev. B* 60 (1999), pp. 11572–11576.
- [54] T. Suntola and J. Hyv[’]arinen. “Atomic layer epitaxy”. In: *Ann. Rev. Mater. Sci.* 15 (1985), pp. 95–177.
- [55] R. W. Johnson et al. “A brief review of atomic layer deposition: from fundamentals to applications”. In: *Materials Today* 17 (2014), pp. 236–246.
- [56] L. Ahmadi. “Advanced photonics with polymer waveguides”. PhD thesis. University of Eastern Finland, 2019.
- [57] R. S. Meltzer et al. “Dependence of fluorescence lifetimes of Y₂O₃ : Eu+3 nanoparticles on the surrounding medium”. In: *Phys. Rev. B* 60 (1999), pp. 14012–14015.
- [58] M. Megens et al. “Fluorescence lifetimes and linewidths of dye in photonic crystals”. In: *Phys. Rev. A* 59 (1999), p. 4727.
- [59] N. Ganesh et al. “Enhanced fluorescence emission from quantum dots on a photonic crystal surface”. In: *Nat. Nanotech.* 2 (2007), pp. 515–520.
- [60] P. Lohdal et al. “Controlling the dynamics of spontaneous emission from quantum dots by photonic crystals”. In: *Nature* 430 (2004), pp. 654–657.
- [61] I. D. Block, L. L. Chan, and B. T. Cunningham. “Photonic crystal optical biosensor incorporating structured low-index porous dielectric”. In: *Sens. and Act. B* 120 (2006), pp. 187–193.
- [62] W. H. Chang et al. “Efficient Single-Photon Sources Based on Low-Density Quantum Dots in Photonic-Crystal Nanocavities”. In: *Phys. Rev. Lett.* 96 (2006), p. 117401.

- [63] K. G. Lee et al. “A planar dielectric antenna for directional single-photon emission and near-unity collection efficiency.” In: *Nat. Photon.* 5 (2011), pp. 166–169.
- [64] L. Novotny and N. F. Van Hulst. “Antennas for light”. In: *Nat. Photon.* 5 (2011), pp. 83–90.
- [65] J. R. Lakowicz. “Radiative decay engineering 3. Surface plasmon coupled directional emission”. In: *An. Biochem.* 324 (2) (2004), pp. 153–169.
- [66] J. E. Donehue et al. “Plasmon-Enhanced Brightness and Photostability from Single Fluorescent Proteins Coupled to Gold Nanorods”. In: *Phys. Chem. C* 118 (2014), pp. 15027–15035.
- [67] C. Y. Wu et al. “Surface-Plasmon-Mediated Photoluminescence Enhancement from Red-Emitting InGaN Coupled with Colloidal Gold Nanocrystals”. In: *Phys. Chem. C* 114 (2010), pp. 12987–12993.
- [68] P. Mühlshlegel et al. “Resonant optical antennas”. In: *Science* 308 (2005), pp. 1607–1609.
- [69] P. Bharadwaj, B. Deutsch, and L. Novotny. “Optical antennas”. In: *Adv. Opt. Photonics* 1 (2009), pp. 438–483.
- [70] V. Giannini, A. I. Fernández-Dominguez, S. C. Heck, et al. “Nanoantennas: Fundamentals and Their Use in Controlling the Radiative Properties of Nanoemitters”. In: *Chem. Rev.* 111 (2011), pp. 3888–3912.
- [71] A. Kinkhabwala et al. “Large Single-Molecule Fluorescence Enhancements Produced by a Bowtie Nanoantenna”. In: *Nat. Photonics* 3 (2009), pp. 654–657.
- [72] T. Kosako, Y. Kadoya, and H. F. Hofmann. “Directional Control of Light by a Nano-optical Yagi-Uda Antenna”. In: *Nat. Photonics* 4 (2010), pp. 312–315.
- [73] F. Hao et al. “Design and Experimental Demonstration of a Plasmonic Directional Beaming Device”. In: *J. Opt. Soc. Am. B* 29 (2012), pp. 2255–2259.
- [74] H. Aouani et al. “Plasmonic Antennas for Directional Sorting of Fluorescence Emission”. In: *Nano Lett.* 11 (2011), pp. 2400–2406.
- [75] H. Aouani et al. “Unidirectional Fluorescence Emission of Molecules in a Nanoaperture with Plasmonic Corrugations”. In: *Nano Lett.* 11 (2011), pp. 637–644.
- [76] M. G. Harats et al. “Full Spectral and Angular Characterization of Highly Directional Emission from Nanocrystal Quantum Dots Positioned on Circular Plasmonic Lenses”. In: *Nano Lett.* 14 (2014), pp. 5766–5771.

- [77] J. T. Choy et al. “Spontaneous Emission and Collection Efficiency Enhancement of Single Emitters in Diamond Via Plasmonic Cavities and Gratings”. In: *Appl. Phys. Lett.* 103 (2013), p. 161101.
- [78] L. Langguth et al. “Plasmonic Band Structure Controls Single-Molecule Fluorescence”. In: *ACS Nano* 7 (2013), pp. 8840–8848.
- [79] J. R. Lakowicz. “Radiative Decay Engineering: Biophysical and Biomedical Applications”. In: *An. Biochem.* 298 (2001), pp. 1–24.
- [80] J. R. Lakowicz. “Radiative Decay Engineering 5: Metal-Enhanced Fluorescence and Plasmon Emission”. In: *An. Biochem.* 337 (2005), pp. 171–194.
- [81] Y. C. Jun, K. C. Y. Huang, and M. L. Brongersma. “Plasmonic Beaming and Active Control over Fluorescent Emission”. In: *Nat. Commun.* 2 (2011).
- [82] O. Gazzano et al. “Evidence for Confined Tamm Plasmon Modes under Metallic Microdisks and Application to the Control of Spontaneous Optical Emission”. In: *Phys. Rev. Lett.* 107 (2011), p. 247402.
- [83] R. Badugu et al. “Radiative Decay Engineering 7: Tamm State-Coupled Emission Using a Hybrid Plasmonic-Photonic Structure”. In: *An. Biochem.* 445 (2014), pp. 1–13.
- [84] Y. K. Chen et al. “Back Focal Plane Imaging of Tamm Plasmons and Their Coupled Emission”. In: *Laser Photonics Rev.* 8 (2014), pp. 933–940.
- [85] D. Zhang et al. “Coupling of Fluorophores in Single Nanoapertures with Tamm Plasmon Structures”. In: *J. Phys. Chem. C* 123 (2019), pp. 1413–1420.
- [86] M. Ballarini et al. “A polymer-based functional pattern on one-dimensional photonic crystals for photon sorting of fluorescence radiation”. In: *Opt. Express* 20 (2012), p. 6703.
- [87] G. D. Zhang, X. C. Yuan, and A. Bouhelier. “Direct Image of Surface-Plasmon-Coupled Emission by Leakage Radiation Microscopy”. In: *Appl. Opt.* 49 (2010), pp. 875–878.
- [88] N. Hartmann et al. “Launching Propagating Surface Plasmon Polaritons by a Single Carbon Nanotube Dipolar Emitter”. In: *Nano Lett.* 12 (2012), pp. 177–181.
- [89] Y. K. Chen et al. “Tamm Plasmon- and Surface Plasmon Coupled-Emission from Hybrid Plasmonic-Photonic Structures”. In: *Optica* 1 (2014), pp. 407–413.
- [90] I. Yu. Chestnov et al. “One-dimensional Tamm plasmons: spatial confinement, propagation, and polarization properties”. In: *Phys. Rev. B* 96 (2017), p. 245309.

- [91] G. Lheureux et al. “Polarization-Controlled Confined Tamm Plasmon Lasers”. In: *ACS Photonics* 2 (2015), pp. 842–848.
- [92] C. Symonds et al. “Confined Tamm Plasmon Lasers”. In: *Nano Lett.* 13 (2013), pp. 3179–3184.
- [93] O. Gazzano et al. “Single Photon Source Using Confined Tamm Plasmon Modes”. In: *Appl. Phys. Lett.* 100 (2012), p. 232111.
- [94] E. M. Purcell. “Spontaneous Emission Probabilities at Radio Frequencies”. In: *Phys. Rev.* 69 (1946), p. 681.
- [95] T. Benson et al. *Frontiers in planar lightwave circuit technology*. Springer (Berlin), 2006.
- [96] S. Bär et al. “Microcavities: tailoring the optical properties of single quantum emitters”. In: *An. Biochem.* 396 (2010), pp. 3–14.
- [97] U. Stella et al. “Enhanced directional light emission assisted by resonant Bloch surface waves in circular cavities”. In: *ACS Photonics* 6 (2019), pp. 2073–2082.
- [98] K. J. Vahala et al. “Optical Microcavities”. In: *Nature* 424 (2003), pp. 839–846.
- [99] J. M. Gerard and B. Gayral. “Strong Purcell Effect for InAs Quantum Boxes in Three-Dimensional Solid-State Microcavities”. In: *Journal of Lightwave Technology* 17 (1999), pp. 2089–2095.
- [100] J. M. Gerard et al. “Quantum boxes as active probes for photonic microstructures: The pillar microcavity case”. In: *Appl. Phys. Lett.* 69 (1996), p. 449.
- [101] J. M. Gerard et al. “Enhanced Spontaneous Emission by Quantum Boxes in a Monolithic Optical Microcavity”. In: *Phys. Rev. Lett.* 81 (1998), pp. 1110–1113.
- [102] B. Gayral et al. “High-Q wet-etched GaAs microdisks containing InAs quantum boxes”. In: *Appl. Phys. Lett.* 75 (1999), p. 1908.
- [103] K. Djordjev and R. D. Dapkus. “Microdisk tunable resonant filters and switches”. In: *IEEE Photonics Technology Letters* 14 (2002), pp. 828–830.
- [104] P. Rabiei, W. H. Steier, and L. R. Dalton. “Polymer micro-ring filters and modulators”. In: *Journal of Lightwave Technology* 20 (2002), pp. 1968–1975.
- [105] K. Srinivasan et al. “Experimental demonstration of a high quality factor photonic crystal microcavity”. In: *Appl. Phys. Lett.* 83 (2003), p. 1915.
- [106] C. J. Hood et al. “The Atom-Cavity Microscope: Single Atoms Bound in Orbit by Single Photons”. In: *Appl. Phys. Lett.* 287 (2000), pp. 1447–1453.
- [107] J. Buck and H. Kimble. “Optimal sizes of dielectric microspheres for cavity QED with strong coupling”. In: *Phys. Rev. A* 67 (2003), p. 033806.

- [108] D. W. Vernooy et al. “High-Q measurements of fused-silica microspheres in the near infrared”. In: *Optics Letters* 23 (1998), p. 247.
- [109] D. K. Armani et al. “Ultrahigh-Q toroid microcavity on a chip”. In: *Nature* 421 (2003), pp. 925–928.
- [110] P. Lodahl et al. “Controlling the dynamics of spontaneous emission from quantum dots by photonic crystals”. In: *Nature* 430 (2004), pp. 654–657.
- [111] D. Englund et al. “Controlling the spontaneous emission rate of single quantum dots in a twodimensional photonic crystal”. In: *Phys. Rev. Lett.* 95 (2005), p. 013904.
- [112] J. S. Foresi et al. “Photonic-bandgap microcavities in optical waveguides”. In: *Nature* 390 (1997), pp. 143–145.
- [113] Z. Yang et al. “Spontaneous emission enhancement of colloidal perovskite nanocrystals by a photonic crystal cavity”. In: *Appl. Phys. Lett.* 111 (2017), p. 221104.
- [114] J. Claudon et al. “A highly efficient single-photon source based on a quantum dot in a photonic nanowire”. In: *Nat. Photonics* 4 (2010), pp. 174–177.
- [115] J. Bleuse et al. “Inhibition, enhancement, and control of spontaneous emission in photonic nanowires”. In: *Phys. Rev. Lett.* 106 (2011), p. 103601.
- [116] P. Kolchin et al. “High purcell factor due to coupling of a single emitter to a dielectric slot waveguide”. In: *Nano Lett.* 15 (2015), pp. 464–468.
- [117] T. Liu et al. “Two-dimensional hybrid photonic/plasmonic crystal cavities”. In: *Optics Express* 22 (2014), pp. 8219–8225.
- [118] S. Derom et al. “Single molecule controlled emission in planar plasmonic cavities”. In: *Phys. Rev. B* 89 (2014), p. 035401.
- [119] G. M. Akselrod et al. “Probing the mechanism of large Purcell enhancement in plasmonic nanoantennas”. In: *Nat. Photonics* 8 (2014), pp. 835–840.
- [120] J. H. Huang et al. “Atomically flat single-crystalline gold nanostructures for plasmonic nanocircuitry”. In: *Nat. Comm.* 1 (2010).
- [121] S. Zenga et al. “Size dependence of Au NP-enhanced surface plasmon resonance based on differential phase measurement”. In: *Sensors and Actuators B* 176 (2013), pp. 1128–1133.
- [122] K. J. Russell and E. L. Hu. “Two-dimensional hybrid photonic/plasmonic crystal cavities”. In: *Appl. Phys. Lett.* 97 (2010), p. 163115.
- [123] E. Jan et al. “Modal Decomposition of Surface-Plasmon Whispering Gallery Resonators”. In: *Nano Lett.* 9 (2009), pp. 3147–3150.
- [124] M. Witzany et al. “Lasing properties of InP/(Ga_{0.51}In_{0.49})P quantum dots in microdisk cavities”. In: *Phys. Rev. B* 83 (2011), p. 205305.

- [125] M. Witzany et al. “Strong mode coupling in InP quantum dot-based GaInP microdisk cavity dimers”. In: *New Journal of Physics* 15 (2013), p. 013060.
- [126] B. Min et al. “High-Q surface-plasmon-polariton whispering-gallery microcavity”. In: *Nature* 457 (2009), pp. 455–458.
- [127] J. C. Weeber et al. “Submicrometer In-Plane Integrated Surface Plasmon Cavities”. In: *Nano Lett.* 7 (2007), pp. 1352–1359.
- [128] K. J. Russell and E. L. Hu. “Large spontaneous emission enhancement in plasmonic nanocavities”. In: *Nat. Photonics* 6 (2012), pp. 459–462.
- [129] C. Belacel et al. “Controlling spontaneous emission with plasmonic optical patch antennas”. In: *Nano Lett.* 13 (2013), pp. 1516–1521.
- [130] A. G. Curto et al. “Unidirectional emission of a quantum dot coupled to a nanoantenna”. In: *Science* 329 (2010), pp. 930–933.
- [131] Y. Chu, M. G. Banaee, and K. B. Crozier. “Double-Resonance Plasmon Substrates for Surface-Enhanced Raman Scattering with Enhancement at Excitation and Stokes Frequencies”. In: *ACS Nano* 4 (2010), p. 2804.
- [132] A. Poddubny et al. “Hyperbolic metamaterials”. In: *Nat. Photonics* 7 (2013), pp. 948–957.
- [133] K. V. Sreekanth et al. “Large spontaneous emission rate enhancement in grating coupled hyperbolic metamaterials”. In: *Sci. Rep.* 4 (2015), p. 6340.
- [134] D. Lu et al. “Enhancing spontaneous emission rates of molecules using nanopatterned multilayer hyperbolic metamaterials”. In: *Nat. Nanotech.* 9 (2014), pp. 48–53.
- [135] P. Ginzburg et al. “Spontaneous emission in non-local materials”. In: *Light: Sci. Appl.* 6 (2017), e16273.
- [136] P. Anger, P. Bharadwaj, and L. Novotny. “Enhancement and Quenching of Single-Molecule fluorescence”. In: *Phys. Rev. Lett.* 96 (2006), p. 113002.
- [137] Y. Ma et al. “Highly directional emission from a quantum emitter embedded in a hemispherical cavity”. In: *Opt. Lett.* 40 (2015), 23732376.
- [138] S. Checcucci et al. “Beaming light from a quantum emitter with a planar optical antenna”. In: *Light: Sci. Appl.* 6 (2017), e16245.
- [139] D. Aurelio and M. Liscidini. “Electromagnetic field enhancement in Bloch surface waves”. In: *Phys. Rev. B* 96 (2017), p. 045308.
- [140] K. Toma et al. “Bloch surface wave-enhanced fluorescence biosensor”. In: *Biosens. Bioelectron.* 43 (2013), pp. 108–114.
- [141] F. Frascella et al. “Enhanced fluorescence detection of miRNA-16 on a photonic crystal”. In: *Analyst* 140 (2015), pp. 5459–5463.

- [142] A. Angelini et al. “Focusing and extraction of light mediated by Bloch surface waves”. In: *Sci. Rep.* 4 (2015), p. 5428.
- [143] L. Yu et al. “Manipulating Bloch surface waves in 2D, a platform concept-based flat lens”. In: *Light: Sci. Appl.* 3 (2014), e124.
- [144] B. V. Lahijani et al. “Bloch surface waves Fabry-Pérot Nanocavity”. In: *J. Phys.* 1093 (2018), p. 012163.
- [145] A. Pitanti et al. “Probing the spontaneous emission dynamics in Sinanocrystals-based microdisk resonators”. In: *Phys. Rev. Lett.* 104 (2010), p. 103901.
- [146] M. N. Berberan-Santos et al. “Mathematical functions for the analysis of luminescence decays with underlying distributions 1. Kohlrausch decay function (stretched exponential)”. In: *Chem. Phys.* 315 (2005), pp. 171–182.
- [147] S. L. Brown et al. “Origin of stretched-exponential photoluminescence relaxation in size-separated silicon nanocrystals”. In: *AIP Adv.* 7 (2017), p. 055314.
- [148] A. Angelini et al. “Surface-Wave-Assisted Beaming of Light Radiation from Localized Sources”. In: *ACS Photonics* 1 (2014), pp. 612–617.
- [149] D. Zhang et al. “Coupling of Fluorophores in Single Nanoapertures with Tamm Plasmon Structures”. In: *J. Phys. Chem. C* 123 (2019), pp. 1413–1420.
- [150] T. T. Tran et al. “Nanodiamonds with photostable, sub-gigahertz linewidth quantum emitters”. In: *APL Photonics* 2 (2017), p. 116103.
- [151] G. Grosso et al. “Tunable and high-purity room temperature singlephoton emission from atomic defects in hexagonal boron nitride”. In: *Nat. Commun.* 8 (2017), p. 705.
- [152] J. H. Poynting. “The wave motion of a revolving shaft, and a suggestion as to the angular momentum in a beam of circularly polarised light”. In: *Proc. R. Soc. Lond. A* 82 (1909), pp. 560–567.
- [153] D. H. Goldstein. *Polarized light*. CRC Press, Taylor & Francis Group, 2001.
- [154] R. Röhrich et al. “Quantifying single plasmonic nanostructure far-fields with interferometric and polarimetric k-space microscopy”. In: *Light-Science & Applications* 7 (2018), p. 65.
- [155] C. G. Darwin. “Notes on the theory of radiation”. In: *Proc. R. Soc. Lond. A* 136 (1932), pp. 34–52.
- [156] L. Allen et al. “Orbital angular-momentum of light and the transformation of Laguerre–Gaussian laser modes”. In: *Phys. Rev. A* 45 (1992), pp. 8185–8189.
- [157] M. Padgett. “Light’s twist”. In: *Proc. R. Soc. A* 470 (2014), p. 2172.

- [158] M. Wang. “Spin-orbit interactions for steering Bloch surface waves with the optical magnetic field and for locally controlling light polarization by swirling surface plasmons”. PhD thesis. Université de Franche-Comté, 2019.
- [159] A. M. Yao and M. J. Padgett. “Orbital angular momentum: origins, behavior and applications”. In: *Adv. Opt. Photon.* 3 (2011), pp. 161–204.
- [160] Y. Shen et al. “Optical vortices 30 years on: OAM manipulation from topological charge to multiple singularities”. In: *Light: Science & Applications* 8 (2019), p. 90.
- [161] M. Padgett, J. Courtial, and L. Allen. “Light’s orbital angular momentum”. In: *Phys. Today* 57 (2004), p. 35.
- [162] X. Yi et al. “Hybrid-order Poincare sphere”. In: *Physical Review A* 91 (2015), p. 023801.
- [163] J. Ng et al. “Hybrid-order Poincare sphere”. In: *Physical Review Letters* 104 (2010), p. 103601.
- [164] D. Cojoc et al. “Hybrid-order Poincare sphere”. In: *Microelectronic Engineering* 78 (2005), pp. 125–131.
- [165] Y. MA et al. “Trapping and manipulation of nanoparticles using multifocal optical vortex metalens”. In: *Scientific Reports* 7 (2017), p. 14611.
- [166] X. Cai et al. “Integrated compact optical vortex beam emitters”. In: *Science* 6 (2012), pp. 338–363.
- [167] Z. Xie et al. “Ultra-broadband on-chip twisted light emitter for optical communications”. In: *Light: Science & Applications* 7 (2018), p. 18001.
- [168] S. Wei et al. “Sub-100 nm resolution PSIM by utilizing modified optical vortices with fractional topological charges for precise phase shifting”. In: *Optics Express* 23 (2015), p. 18001.
- [169] L. X. Chen, J. J. Lei, and J. Romero. “Quantum digital spiral imaging”. In: *Light: Science & Applications* 3 (2014), e153.
- [170] J. Wang et al. “Terabit free-space data transmission employing orbital angular momentum multiplexing”. In: *Nature Photonics* 6 (2012), pp. 488–496.
- [171] G. Ruffato, M. Massari, and F. Romanato. “Diffractive optics for combined spatial-and mode-division demultiplexing of optical vortices: design, fabrication and optical characterization”. In: *Scientific reports* 6 (2016), p. 24760.
- [172] X. Wang et al. “Recent advances on optical vortex generation”. In: *Nanophotonics* 7 (2018), pp. 1533–1556.
- [173] L. Marucci, C. Manzo, and D. Paparo. “Optical Spin-to-Orbital Angular Momentum Conversion in Inhomogeneous Anisotropic Media”. In: *Physical Review Letters* 96 (2006), p. 163905.

- [174] I. Moreno et al. “Decomposition of radially and azimuthally polarized beams using a circular-polarization and vortex-sensing diffraction grating”. In: *Optics Express* 18 (2010), pp. 7173–7183.
- [175] F. Cardano et al. “Polarization pattern of vector vortex beams generated by q-plates with different topological charges”. In: *Applied Optics* 51 (2012), pp. C1–C6.
- [176] P. Genevet et al. “Holographic detection of the orbital angular momentum of light with plasmonic photodiodes”. In: *Nature Communications* 3 (2012), p. 1278.
- [177] J. Lin et al. “Nanostructured holograms for broadband manipulation of vector beams”. In: *Nano Letters* 13 (2016), pp. 4269–4274.
- [178] A. Zhan et al. “Low-Contrast Dielectric Metasurface Optics”. In: *ACS Photonics* 3 (2016), pp. 209–214.
- [179] Y. Zhou et al. “Orbital angular momentum generation via a spiral phase microsphere”. In: *Optics Letters* 43 (2018), pp. 34–37.
- [180] F. Yue et al. “Vector Vortex Beam Generation with a Single Plasmonic Metasurface”. In: *ACS Photonics* 3 (2016), pp. 1558–1563.
- [181] Y. W. Huang et al. “Versatile total angular momentum generation using cascaded J-plates”. In: *Optics Express* 27 (2019), pp. 7469–7484.
- [182] F. Bouchard et al. “Optical spin-to-orbital angular momentum conversion in ultra-thin metasurfaces with arbitrary topological charges”. In: *Applied Physics Letters* 105 (2014), p. 101905.
- [183] E. Maguid et al. “Topologically Controlled Intracavity Laser Modes Based on Pancharatnam-Berry Phase”. In: *ACS Photonics* 5 (2018), pp. 1817–1821.
- [184] Z. Wang et al. “Induced Optical Chirality and Circularly Polarized Emission from Achiral CdSe/ZnS Quantum Dots via Resonantly Coupling with Plasmonic Chiral Metasurfaces”. In: *Laser & Photonics Reviews* 13 (2019), p. 1800276.
- [185] H. Kim et al. “Synthesis and Dynamic Switching of Surface Plasmon Vortices with Plasmonic Vortex Lens”. In: *Nano Letters* 10 (2010), pp. 529–536.
- [186] G. Rui, R. L. Nelson, and Q. Zhan. “Beaming photons with spin and orbital angular momentum via a dipole-coupled plasmonic spiral antenna”. In: *Optics Express* 18 (2012), pp. 819–826.
- [187] H. Yu et al. “Optical orbital angular momentum conservation during the transfer process from plasmonic vortex lens to light”. In: *Scientific Reports* 3 (2013), p. 3191.

- [188] Q. Jiang et al. “Directional and Singular Surface Plasmon Generation in Chiral and Achiral Nanostructures Demonstrated by Leakage Radiation Microscopy”. In: *ACS Photonics* 3 (2016), pp. 1116–1124.
- [189] Y. Gorodetski et al. “Observation of Optical Spin Symmetry Breaking in Nanoapertures”. In: *Nano Letters* 9 (2009), pp. 3016–3019.
- [190] B. Zhang et al. “Chiral plasmonic lens with Archimedes-spiral distributed nanoslits”. In: *Journal of Nanophotonics* 13 (2019), p. 026008.
- [191] Y. Gorodetski et al. “Generating Far-Field Orbital Angular Momenta from Near-Field Optical Chirality”. In: *Phys. Rev. Lett.* 110 (2013), p. 203906.
- [192] A. Sinibaldi et al. “Combining label-free and fluorescence operation of Bloch surface wave optical sensors”. In: *Optics Letters* 39 (2014), pp. 2947–2950.
- [193] A. Angelini et al. “Fluorescence diffraction assisted by Bloch surface waves on a one-dimensional photonic crystal”. In: *New Journal of Physics* 15 (2013), p. 073002.
- [194] G. Rui, D.C. Abeysinghe R. L. Nelson, and Q. Zhan. “Demonstration of beam steering via dipole-coupled plasmonic spiral antenna”. In: *Sci. Rep.* 3 (2013), p. 2237.
- [195] G. Pellegrini et al. “Chiral surface waves for enhanced circular dichroism”. In: *Phys. Rev. B* 95 (2017), p. 241402.
- [196] R. Badugu et al. “Bloch Surface Wave-Coupled Emission at Ultra-Violet Wavelengths”. In: *J. Phys. Chem. C* 120 (2016), pp. 28727–28734.
- [197] A. Pham. “Chiral optical local density of states in a spiral plasmonic cavity”. In: *Phys. Rev. A* 94 (2016), p. 053850.
- [198] P. Pachidis, B. M. Cote, and V. E. Ferry. “Tuning the polarization and directionality of photoluminescence of achiral quantum dot films with chiral nanorod dimer arrays: implications for luminescent applications”. In: *ACS Applied Nano Materials* 2 (2019), pp. 5681–5687.

Acknowledgements

First, I thank Prof. Emiliano Descrovi for the opportunity to work on this exciting and challenging topic and for the supervision. His impressive ways of creating ideas, giving advices, proof-reading and discussing manuscripts, abstracts, and even this work, and especially sharing his knowledge, guided me in all the time of research.

The enthusiasm and scientific spirit of Dr. Angelo Angelini have accompanied me in the lab, in the clean room and most of all in the coffee time. I thank him for the valuable ideas, thousands of explanations and for always being there.

I like to thank Prof. Matthieu Roussey for inviting me to the University of Eastern Finland and giving me the opportunity to work in his team. His guidance was really motivating and enjoyable.

I sincerely thank Prof. Paolo Biagioni for his willingness to review this thesis.

Further, I want to thank:

Prof. Ubirajara Agero Batista for the stimulating discussions about interferometric and polarimetric k -space microscopy and for all the moments of mountain climbing spent together. His presence made the laboratory a better place.

Dr. Ségolène Pélisset for her precious guidance in understanding and running ALD processes and her help with the ellipsometer.

Dr. Luca Boarino and Dr. Natascia De Leo for giving me the opportunity to work in the QR laboratory and Nanofacility Piemonte in INRIM. Dr. Federico Ferrarese Lupi and Dr. Emanuele Enrico for their constant support in clean room and with the EBL.

Prof. Hans Peter Herzig for inviting me to EPFL in the wonderful city of Neuchâtel and the former members of his OPT Lab, Dr. Myunsik Kim, Dr. Babak Vosoughi Lahijani, Dr. Nicolas Descharmes, Dr. Gaël Osowiecki, Dr. Grégoire Smolik and Dr. Sara Santi for making the stay there unforgettable.

My former teammates Dr. Francesca Frascella, Dr. Serena Ricciardi, Federica Pirani, Susanna Licheri and Chiara Summa for constant support.

Dr. Gianluca Palmara and Dr. Roberta Calmo for the really pleasant company in the pink office and the support in the laboratory.

Most of all, I thank my family and my love, Alessandra, for having always believed in me.

This Ph.D. thesis has been typeset by means of the T_EX-system facilities. The typesetting engine was pdfL^AT_EX. The document class was `toptesi`, by Claudio Beccari, with option `tipotesi=scudo`. This class is available in every up-to-date and complete T_EX-system installation.